REPORT DOCUMENTATION PAGE

Public reporting burden for this collection of information is estimated to average 1 hour per response, including the time for reviewing instructio data needed, and completing and reviewing this collection of information. Send comments regarding this burden estimate or any other aspect this burden to Department of Defense, Washington Headquarters Services, Directorate for Information Operations and Reports (0704-0188), 12 4302. Respondents should be aware that notwithstanding any other provision of law, no person shall be subject to any penalty for failing to com, valid OMB control number. PLEASE DO NOT RETURN YOUR FORM TO THE ABOVE ADDRESS.

0238

1. REPORT DATE *(DD-MM-YYYY)* 02-06-2005	**2. REPORT TYPE** Final Technical Report	**3. DATES COVERED** *(From - To)* 01 SEP 2004 - 31 MAY 2005
4. TITLE AND SUBTITLE "Quench-Protection Strategies for HTS Superconductors"		**5a. CONTRACT NUMBER** FA9550-04-C-0073
		5b. GRANT NUMBER
		5c. PROGRAM ELEMENT NUMBER
6. AUTHOR(S) William N. Lawless		**5d. PROJECT NUMBER**
		5e. TASK NUMBER
		5f. WORK UNIT NUMBER
7. PERFORMING ORGANIZATION NAME(S) AND ADDRESS(ES) CeramPhysics, Inc. 921 Eastwind Dr., Suite 110 Westerville, OH 43081		**8. PERFORMING ORGANIZATION REPORT NUMBER**
9. SPONSORING / MONITORING AGENCY NAME(S) AND ADDRESS(ES) AFOSR/PKC 4015 Wilson Blvd, Room 731 Arlington, VA 22203-1954		**10. SPONSOR/MONITOR'S ACRONYM(S)**
		11. SPONSOR/MONITOR'S REPORT NUMBER(S)

12. DISTRIBUTION / AVAILABILITY STATEMENT

Approved for public release, distribution unlimited

13. SUPPLEMENTARY NOTES

14. ABSTRACT

Assessments are made of four distinct strategies for the quench protection of HTS coils near 77 K -- diamond-film insulation, cryovaristor current shunt, loaded Formvar insulation, and a sputtered ceramic insulation. An improved three-dimensional thermal modeling of quench protection is developed which provides guidelines for judging the strategies.

Boundary scattering depresses the thermal conductivity of diamond films and Kapitsa resistance depresses the thermal conductivity of loaded Formvar insulation, rendering these strategies non-viable.

The cryovaristor current shunt is modeled electrically and it is concluded that this strategy requires substantial development with a low probability of success. However, the cryovaristor ceramic has a large thermal conductivity due to the ZnO grains and is the insulation material of choice from the thermal modeling.

Thin films of a high-thermal-conductivity ZG ceramic sputtered on substrates were amorphous and could not be crystallized without exceeding the 400 C limitation of the HTS coil (e.g., 600 C).

These assessments, while discouraging, are valuable for advancing the technology. In a Phase II program, appropriate deposition methods for ZG and ZnO should be pursued and small HTS magnets wound and tested, together with continuing thermal modeling studies.

15. SUBJECT TERMS

Quench Protection Strategies, Insulation of HTS Coils, Cryovaristor

16. SECURITY CLASSIFICATION OF:			**17. LIMITATION OF ABSTRACT**	**18. NUMBER OF PAGES**	**19a. NAME OF RESPONSIBLE PERSON**
					C.F. Clark, Jr.
a. REPORT	**b. ABSTRACT**	**c. THIS PAGE**	UU	86	**19b. TELEPHONE NUMBER** *(include area code)*
U	U	U			614-882-2231

June 22 05

CeramPhysics, Inc.
921 Eastwind Drive, Suite #110, Westerville, Ohio 43081
Telephone (614) 882-2231 FAX (614) 882-1437

FINAL REPORT

"Quench-Protection Strategies for HTS Conductors"
Contract No. FA9550-04-C-0073

W. N. Lawless

June 2, 2005

TABLE OF CONTENTS

Page

I. SUMMARY 1

II. INTRODUCTION AND BACKGROUND 2

III. REVIEW OF DIELECTRIC INSULATIONS FOR QUENCH PROTECTION 5

- A. Introduction 5
- B. Dielectric Insulations for Powder-in-Tube Ceramic Superconductors 5
- C. Dielectric Insulations for Epitaxially Grown YBCO on a Ni Substrate 7
- D. Conclusions, Discussion, Recommendations 9

IV. ASSESSMENT OF DIAMOND FILMS 24

- A. Introduction 24
- B. Review of Thermal Conduction in Solids 24
- C. Thermal Conductivity of Diamond Films 27
- D. Discussion and Conclusions 28

V. ASSESSMENT OF CRYOVARISTOR FOR QUENCH PROTECTION 36

- A. Introduction and Background 36
- B. Review of Measured Properties of the Cryovaristor 38
- C. Cryovaristor Electrical and Thermal Models 39
- D. Discussion and Conclusions 43

VI. FORMVAR VARNISH LOADED WITH CERAMIC POWDERS 50

- A. Sample Preparation and Measurement Methods 50
- B. Measurement Results 52
- C. Discussion and Conclusion 53

VII. ASSESSMENT OF SPUTTERED INSULATING FILM 63

VIII. THREE-DIMENSIONAL THERMAL MODELING 69

- A. Summary 69
- B. Introduction 69
- C. Governing Equations 70
- D. Novel Current Sharing Model 71
- E. Numerical Procedures 72
- F. Results and Discussions 72

IX. CONCLUSIONS OF THE PHASE I STTR PROGRAM 84

I. SUMMARY

A broad-based program has been successfully pursued to make assessments of four distinct strategies for the quench protection of HTS coils near 77 K -- diamond-film insulation, cryovaristor current shunt, loaded Formvar insulation, and a sputtered ceramic insulation. Three-dimensional thermal modeling of quench protection has provided important guidelines for judging the strategies, and a greatly improved modeling code has been developed in the program for doing so.

Boundary scattering substantially depresses the thermal conductivity of diamond films. An analysis indicates that a 10-micron thick diamond film would have a thermal conductivity of only 130 mW/cm-K at 77 K which is too small to be of interest from the thermal modeling of quench protection.

The cryovaristor current shunt is modeled electrically. For this strategy to work, both sides of the HTS coil would have to have a Cu overlayer, and current would have to travel a considerable distance in one of the Cu overlayers to build the 1 kV/cm field needed to switch the cryovaristor. Also, one full turn of the coil would have to be sacrificed. The major drawback to this strategy is the cryovaristor characteristic requires a substantial amount of impurities in the grain boundaries which may not be achievable with deposition methods limited to 400 °C.

The cryovaristor ceramic is very significant but for a *different* reason. Namely, this ceramic has a very large thermal conductivity at 77 K, 620 mW/cm-K, and is in fact the insulation material of choice from the thermal modeling. This conductivity is due to the ZnO grains and is not boundary-scattering limited for films thicker than 5 micron.

Measurements of Formvar loaded with 1.5 micron powders of a high-thermal-conductivity NN ceramic show that Kapitsa resistance at the Formvar/ceramic interface depresses the thermal conductivity of the composites, 15 - 17 mW/cm-K at 77 K. Thermal modeling indicates these values are too small to provide any quench protection.

Thin films of a high-thermal-conductivity ZG ceramic sputtered on substrates were amorphous and could not be crystallized without exceeding the 400 °C limitation of the HTS coil (e.g., 600 °C). Therefore, this strategy remains viable but alternate or modified deposition methods should be explored consistent with the 400 °C constraint because ZG has a large thermal conductivity at 77 K, 224 mW/cm-K, which is not boundary-scattering limited for films thicker than 5 micron.

The assessments of these four quench-protection strategies are not encouraging but they are valuable for advancing the technology. In a Phase II program, appropriate deposition methods for ZG and ZnO should be pursued and small HTS magnets wound and tested, together with continuing thermal modeling studies.

II. INTRODUCTION AND BACKGROUND

Magnets wound with HTS are of interest to the Air Force for power components such as generators and gyrotron tubes and are also of interest for commercial utility power applications. Early HTS magnets were operated in the 20-30 K range but required refrigeration systems that were large and heavy. Magnet operation near 77 K would relieve most of these refrigeration penalties, but quench protection becomes a serious consideration at these higher temperatures. As the temperature of the HTS increases, the thermal diffusivity of the superconductor decreases and the quench propagation velocity slows to a few cm/sec, causing the magnet energy to be discharged rapidly into a small volume, possibly destroying the magnet. New methods of quench protection will be required as the operating temperature is raised in order to minimize refrigeration size and weight.

The current structure for a 1-cm-wide HTS tape consists of the following materials and dimensions (in microns): YBCO (1-2) coated with CeO_2 (0.3-1.0) deposited on a Ni substrate (50-100), and a Ag overlayer (3-4) and a Cu overlayer (20-80) are atop the YBCO. The overall thickness of the tape is 75 to 188 microns (i.e., 3 to 7.4 mil), and since there are compelling reasons to conserve space, practical quench-protection methods applied to the tape have to be commensurably thin. Also, the processing of any such means is limited to 400 °C to preserve the oxygen stochiometry of the YBCO.

One possible strategy for quench protection is to provide a dielectric insulation with large thermal conductivity in the 60 - 90 K range, and this insulation can be very thin and still be compatible with the standoff voltage for the HTS tape (~ 5 V). Another possible strategy is to provide a film of a so-called "cryovaristor" ceramic which switches from an insulator to a conductor for an applied electric field of about 1 kV/cm at cryogenic temperatures -- such a film could, in principle, shunt the current out of a normal region of YBCO to prevent a quench.

The purpose of this Phase I STTR program is to make assessments of *three* dielectric-insulation strategies *and* an assessment of the cryovaristor strategy for quench protection. Thermal modeling studies of the dielectric insulations at the Univ. of Pittsburgh in this program play a key role in the assessments.

The three dielectric insulations considered are: (1) Formvar insulation loaded with ceramic powders having a large thermal conductivity; (2) Sputtered film of a ceramic insulation having a large thermal conductivity; and (3) Vapor-deposited diamond film insulation. The first type of insulation is inexpensive and immediately lends itself to a commercial, room-temperature, draw-tower application. The second type is more expensive to deposit but the technology exists for doing so. The third type is currently in the development stage at Wright Patterson AFB and is expected to be the most expensive.

The cryovaristor ceramic retains the varistor I-V characteristic down to helium temperatures, hence the name cryovaristor. In contrast, conventional varistors lose this characteristic when cooled below room temperature, and in Fig. II-1 are shown comparative data for these ceramics.

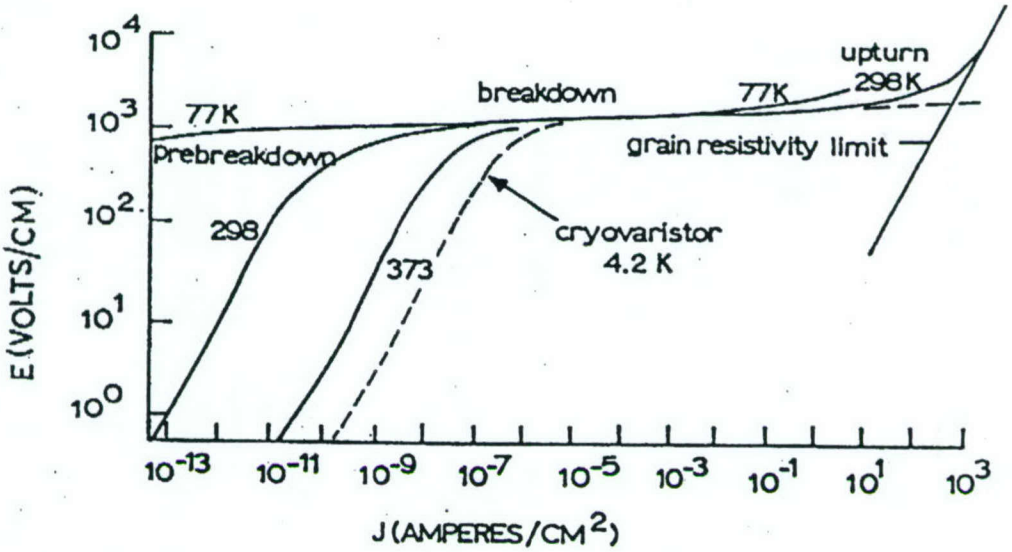

FIGURE II-1. *The electric field - current density effect in a cryovaristor ceramic at 4.2 K compared to conventional varistor ceramics.*

The quench-protection concept for the cryovaristor is to place a film of this ceramic in parallel electrically with the superconducting winding, and when a portion of the winding becomes resistive the resulting voltage causes the current to shunt through the cryovaristor film.

There have been previous programs at CeramPhysics in the first two types of dielectric insulations and in the cryovaristor technology, and these program results provide the databases for assessing these strategies. For the first type of insulation, the goal of an SBIR program (Phase I only, BMDO #F33615-99-C-2929) was to provide an insulation for YBCO epitaxially grown on a Ni substrate with the constraint that the insulation could not be applied above 500 °C. The approach taken was to load powders of the large thermal conductivity ceramics into a Formvar varnish (GE 7031 varnish).

For the second type of insulation, the goal of Phase I and Phase II SBIR programs (AF Contracts F33615-91-C-2122 and F33615-92-C-2286) was to provide a dielectric insulation with a large thermal conductivity 60 - 90 K for powder-in-tube YBCO that could be co-fired on a Ni tube at elevated temperatures.

Finally, the physics of the cryovaristor ceramic was the subject of three Air Force programs (#F33615-81-C-2013, -2637, and -2721), and the feasibility of using this approach for the quench protection of A15 superconducting magnets was the subject of a Phase I, SBIR program with DOE (#DE-ACO2-85ER-80267). It was shown in these programs that the cryovaristor characteristic is independent of magnetic fields up to 10 T at cryogenic temperatures.

This Final Report is organized as follows: Each section is written as a stand-alone section with figures, references, and conclusions. Section III is a review of the results

from previous programs on dielectric insulations for ceramic superconductors. An assessment of the diamond-film insulation strategy for quench protection is given in Section IV, and an assessment of the cryovaristor strategy is given in Section V. Additional measurements of a Formvar varnish loaded with very fine ceramic powders are given in Section VI, and the results of sputtering thin films of a ceramic with a large thermal conductivity at 77 K are given in Section VII. The results of three-dimensional thermal modeling of quench protection are given in Section VIII, and the Discussion and Conclusions for the entire Phase I program are given in Section IX.

The ceramic powders used in Section VI were prepared by NexTech Materials, Ltd. where SEM's of the cast Formvar bars were also made. The work on sputtering thin films in Section VII was performed at Sputtering Target Manufacturing Co. LLC, and the three-dimensional thermal modeling in Section VIII was performed by Prof. Minking Chyu at the University of Pittsburgh.

III. REVIEW OF DIELECTRIC INSULATIONS FOR QUENCH PROTECTION OF SUPERCONDUCTING CERAMICS

A. INTRODUCTION

There have been three Air-Force-sponsored programs at CeramPhysics, Inc. on the quench protection of magnets made with superconducting ceramics. The goal of these programs was to provide dielectric insulations with large thermal conductivities as a means for thermal management to avoid magnet quenches.

The first two programs were Phase I and Phase II SBIR programs (F33615-91-C-2122 and F33615-92-C-2286) focused on the "powder in tube" process for fabricating ceramic superconductors. The third program was a Phase I SBIR program (F33615-99-C-2969) focused on the epitaxial growth of YBCO on a Ni substrate using pulsed-laser-deposition methods.

The insulation applications were different for these two fabrication methods, and consequently the approaches taken to develop insulations were also very different. The programs for these two methods will be reviewed separately.

Two candidate insulations will be recommended for the present STTR program based on this review of previous programs.

B. DIELECTRIC INSLUATIONS FOR "POWDER-IN-TUBE" CERAMICS SUPERCONDUCTORS

a. Phase I Program

The goal of these Phase I and Phase II programs was to provide a dielectric insulation with a large thermal conductivity in the 20 - 40 K temperature range, and the insulation should be co-firable with the YBCO + Ni tube at 1150 °C for 10 - 15 min. A small specific heat of the insulation is desirable to ensure a large thermal diffusivity, and a good thermal expansion match to Ni, 20 K to 1150 °C, is also very desirable.

A review was given in Phase I of the physics of thermal conductivity in insulators at low temperatures, and this review provided useful guidelines for selecting candidate materials. A particularly useful reference is amorphous materials which all have approximately the same thermal conductivity at low temperatures due, it is believed, to a two-level tunneling system. All the crystalline materials in this study were compared to amorphous materials.

A comprehensive review of measured thermal conductivity data was made in Phase I using published data sources and CeramPhysics' unpublished database. The review covered ferroelectrics (including antiferroelectrics and relaxors), fast-ion conductors, cesium and thallous halides, glass ceramics, and miscellaneous oxides (alumina, magnesia, spinels, columbites, pyrochlores, etc.), and composites of oxides and glasses. A so-called "cryovaristor" ceramic was also included in the review.

A down selection was made based on compatibility with the 1150 °C co-firing condition. Four categories of materials were selected for study, and fifteen materials

were prepared for measurements of thermal conductivity and specific heat in the 20 - 90 K range in Phase I. A final down selection to eight materials was made based on the thermal data, and in Figs. III-1 and III-2 are the summary plots of thermal conductivity and thermal diffusivity for these materials. The data in Figs. III-1 and III-2 are compared to amorphous materials ("glasses, resins, epoxies, etc.") as mentioned above.

It was not possible to measure thermal expansion data over the 20 K to 1150 °C range, but thermal expansion data at room temperature were compared to that of Ni for several materials. Poorly matched materials were not pursued further and are not included in Figs. III-1 and III-2.

The cryovaristor shown in Figs. III-1 and III-2 will be the subject of a section.

The Phase I program was very successful in demonstrating candidate ceramic insulations with thermal conductivities and thermal diffusivities up to an order of magnitude larger than those of amorphous materials at low temperatures. Based on these findings, new materials' directions were recommended for the Phase II program.

b. Phase II Program

From the Phase I program, ceramics containing Zn, Bi, and Ni appeared most promising, and a glass-ceramic approach was also recommended. The exploratory materials research in the Phase II program progressed in three stages, as follows:

In the first stage, the candidate materials recommended from Phase I were pursued. These were prepared as ceramic discs and their thermal conductivities and specific heats were measured 10 - 90 K (throughout Phase II ceramic-preparation results were used to eliminate some materials). Three glass-ceramics were also examined -- two new glass ceramics were prepared and the third glass ceramic was donated by Corning Glass Works.

In the second stage, the results obtained on the first stage materials eliminated some materials and suggested new materials for the second round of preparations and measurements. Two-phase ceramics were explored, and minor phases were added in some cases to improve sintering conditions. The specific heats and thermal conductivities of the materials were measured 10-90 K.

A total of twenty-three candidate insulation materials were evaluated in Phase II.

In the third stage, seven final dielectric insulation materials were selected from the results of the first two stages. Two selection criteria were used: (1) Magnitude of the thermal diffusivity at 20 K; and (2) Sinterability to a dense body at 1150 °C for 10 min. Thermal diffusivity data for these selected materials are shown in Fig. III-3 compared to glass, and it is seen that the thermal diffusivity of the selected materials range up to 100 times larger than that of amorphous materials at low temperatures. Four of the materials in Fig. III-3 are two-phase materials (e.g., 90/10 NN/BN) because the two-phase approach facilitated satisfying the 1150 °C sintering condition.

The final materials were characterized with regard to thermal expansion coefficient (20 K to 1100 °C), dielectric properties, adherence to Ni, and oxygen

diffusion. These properties will not be reviewed here because they do not apply to the topic of this STTR program.

We mention for completeness sake that the thermal properties of YBCO and the Ni sheath were measured in Phase II, including measurements in intense magnetic fields, but these will not be reviewed here. The thermal boundary resistance between YBCO and the Ni sheath due to a NiO layer was also thoroughly characterized in the Phase II program.

Computer Modeling. We conclude this review of the Phase II program by describing the results of three-dimensional, transient heat flow modeling performed by Prof. Minking Chyu (then of Carnigie Mellon Univ.).

The model here assumed a flat tape geometry for the Ni/YBCO HTSC conductor, and the measured thermal property data above for the insulations and for the Ni and YBCO constituents in magnetic fields were included in the modeling. Of particular importance, an effective heat transfer coefficient between the HTSC tape and the ambient coolant of 10 mW/cm^2 was adopted.

The primary quantity computed from the model was the maximum recoverable current, defined as the greatest current permissible to maintain the conductor stable, following a transient disturbance.

The thermal diffusivities of the insulation materials appear to play a surprisingly minor role in the modeled stability of the HTSC tape conductor. The large thermal boundary resistance of the NiO layer is also found to play a minor role. The reason for these findings is that the dominant heat flow is *longitudinal* rather than transverse, and this is driven by the value assumed above for the heat transfer coefficient.

In the presence of magnetic fields the maximum recoverable current is severely reduced due to the suppressed thermal conductivity of the Ni sheath in the case that the dominant heat transfer is longitudinal.

These three-dimensional modeling studies clearly show that the advantages of a highly thermally conducting insulation cannot be utilized for increased stability of the HTSC tape conductor unless the transverse heat conduction can be improved, and this in turn depends on increasing the heat transfer coefficient between the conductor and the ambient coolant.

C. DIELECTRIC INSULATIONS FOR EPITAXIALLY GROWN YBCO ON A Ni SUBSTRATE

The goal of this Phase I program was to provide a dielectric insulation for YBCO grown epitaxially on a Ni substrate by pulsed-laser-deposition methods. The condition here differed substantially from that involved in the Phase I and Phase II programs reviewed above in that the insulation had to be applied in a post-operation below 500 °C to preserve the oxygen stochiometry of the YBCO. For this reason, a *room-temperature* application of the insulation was selected for this program wherein powders of a ceramic having a large thermal conductivity would be added to an organic vehicle, making the

insulation system compatible with a draw-tower coating method. Also, the temperature range for this program was 60 - 100 K.

Single-phase ceramics have larger thermal conductivities at low temperature than two-phase ceramics, and the single-phase ceramic choices for this Phase I program were selected from the Phase II program reviewed above, as follows: The two-phase ceramic approach shown in Fig. III-3 was selected primarily to adjust the sintering temperature to 1150 °C, and the thermal conductivities of the *individual* phases were measured in the process of developing the two-phase approach. It is from this database that five ceramics were selected here, and in Fig. III-4 are shown the thermal conductivity data for these ceramics. Thermal diffusivity data are shown in Fig. III-5. Again, the data are compared to that of "glass".

Turning next to the organic vehicle, discussions were held with the manufacturer of Formvar-type insulations (Insulating Materials, Inc., Schenectady) and with a commercial wire-coating company with experience using these insulations (California Fine Wire). The consensus was to use GE 7031 varnish, which is a type of Formvar, because: (1) The excellent properties of this varnish at low temperatures are well known; (2) Whatever is developed with this varnish will easily carry over to other Formvars; and (3) There is a toxicity issue in California with shipping Formvar but not GE 7031.

The approach then was to add powders of the ceramics in Fig. III-4 to GE 7031 varnish at the 40 and 60 vol% levels (i.e., cured %'s, see below). A ceramic particle size of 10 micron was selected for the powders to minimize Kapitza resistance, and NexTech Materials, Ltd. prepared these powders.

The first step was to develop the methodology for preparing composite powder/7031 samples for measurement, and this proved challenging. This methodology was critical for this program and is reviewed here in some detail. On the one hand, the varnish had to be dilute enough to allow air bubbles to escape, but on the other hand the varnish could not be so dilute that the ceramic particles would settle out. The competition between these two effects required measuring the viscosity of the varnish as a function of the dilutant (50/50 methanol/toluene), and Stokes law of settling provided useful guidelines for maintaining a uniform distribution of particles.

The optimum viscosity of the diluted varnish was determined, and the cured properties of the varnish were calibrated. Curing requires two steps: An air cure for about 3 hours followed by a bake out at 125 °C for 4 hours. Measuring the final density of the varnish (1.015 g/cc) and knowing the densities of the ceramics allowed the design of samples at 40 and 60 vol% cured powder densities. It turned out that the vol% of the powders in the starting mixture is surprisingly small because the undiluted varnish contains only 19% solids by weight after bake out (e.g., only 8.2 vol% of powder in the starting mixture will yield 40 vol% powder after bake out).

Samples were prepared by repeatedly dip-coating a thin aluminum mold in a well-mixed varnish/powder slurry with air-drying between dips. This was found necessary because the optimum varnish viscosity would only allow a thin coating per dip. When a

build of about 2½ mm was reached, the sample was removed from the mold and baked out.

Ten samples were prepared and first used for thermal conductivity measurements, 60 - 100 K. The samples were then cleaned and used for thermal expansion measurements, 60 - 300 K. Finally, the samples were ground plane-parallel and used for density measurements to determine the porosity (which was always found to be small).

The specific heats of the five ceramics were measured in the Phase II program above. The specific heat of GE 7031 varnish has been published, and the specific heats of the powder/7031 composites here were calculated according to a linear mixing rule (valid because the varnish and the ceramics do not interact chemically). The resulting specific heats combined with the thermal conductivity data were used to determine thermal diffusivity data.

The candidate insulations were down selected based on thermal conductivity/diffusivity, and in Figs. III-6 and III-7 are shown these data for the three most favorable composites, 60NN, 60ZT, and 60ZG, respectively (60NN here means 60 vol.% NN in the GE 7031 varnish, etc.). The thermal properties of cured GE 7031 are also shown for comparison. Not surprisingly, the 60 vol% composites had larger thermal conductivities and diffusivities than the 40 vol% composites, ranging up to 10 times larger than that of GE 7031.

Thermal expansion data below room temperature are shown in Fig. III-8 for the down selected composites compared to Ni and to GE 7031. There is a very large thermal-expansion mismatch between Ni and GE 7031, but ceramic powder additions to the varnish greatly suppresses this mismatch.

Finally, the insulation voltage standoff at 77 K was measured on twisted wires which had been coated with the powder/7031 composites. In thin coatings, ~ 25 - 50 micron, the composites had electric-field withstands of 1000 - 3000 volts per mil, equivalent to that of the GE 7031 varnish alone.

D. CONCLUSIONS, DISCUSSION, AND RECOMMENDATIONS

The three previous programs reviewed here were each successful in achieving their goals at the time, and these programs reflect the progress-induced changes made in the field of ceramic superconductors over this time period. The present STTR program is based on an HTS conductor design which has evolved from the designs on which the previous programs were based.

The current design is a 1-cm wide HTS ribbon consisting of the following materials and their dimensions (in microns): YBCO (1-2) coated with CeO_2 (0.3-1.0) deposited on a Ni substrate (50-100), and a Ag overlayer (3-4) and a Cu overlayer (20-80) are atop the YBCO. Therefore, the overall thickness of the ribbon is 75 to 188 microns. The turn-to-turn voltage withstand is < 10 volts, and consequently the dielectric insulation can be *very thin*, ~ 2 - 20 micron (e.g., for an insulation with a standoff field of 1000 volts per mil, a layer 0.25 micron which withstands 10 volts). In fact, there is a

premium on a thin dielectric insulation in order to conserve space and weight within the coil.

In the STTR program, two types of candidate insulation materials will be applied to HTS ribbons and evaluated: (1) A ceramic will be sputtered onto a ribbon sample; and (2) A powder/7031 composite will be dip-coated onto a ribbon sample. Since a premium is placed on a large thermal conductivity and diffusivity, the **Zn_2GeO_4** ceramic in Fig. III-3 is the clear choice for a sputtering target. For a composite with GE 7031 varnish, the **60NN** composite in Figs. III-6 and III-7 is the clear choice for the composite approach. Thermal conductivity and thermal diffusivity data for these two choices are plotted in Figs. III-9 and III-10, respectively. These data plus specific heat data for the two candidates are given in Table III-I.

The thermal conductivity and diffusivity for Zn_2GeO_4 in Figs. III-9 and III-10 are an order of magnitude larger than those for 60NN, but the former material is for a sputtered film which has not yet been demonstrated. On the other hand, the latter material can be used in a commercial, inexpensive draw-tower deposition method.

The Zn_2TiO_4 ceramic has a better thermal expansion match with Ni than the Zn_2GeO_4 ceramic but a much smaller thermal conductivity (Fig. III-4). Sputtered thin films are very tolerant of thermal-expansion mismatches, so this does not alter the choice of Zn_2GeO_4 for this program (although this may be re-visited in the future).

Data for glass are also included in Figs. III-6 and III-7 and given in Table III-I for possible use in modeling studies.

The cryovaristor ceramic shown in Fig. III-1 is of interest as a possible shunting material in its conducting state for current sharing in the early stages of a quench and will be the subject of another section. The thermal properties of the cryovaristor in its insulating state are given here in Table III-I for possible use in modeling studies.

Discussions have been held with California Fine Wire (CFW) regarding the 60NN composite insulation. CFW has had experience coating wires with very thin insulations, ~ 25 micron, plus experience in loading ceramic powders in insulations. For a 60 vol% cured loading in a 25 micron insulation, CFW recommends that the ceramic powder grain size be about 1 - 2 micron. This specification has been supplied to NexTech Materials for preparing the NN powders, and a new can of GE 7031 varnish has been ordered.

The sputtering target information ahs been supplied to Sputtering Target Manufacturing Co.

In conclusion, we return to what has been learned from the computer modeling in the Phase II program above where it was found that the longitudinal heat transfer through the Ni sheet was dominant. These results may not apply in the present case due to the *new geometries* involved. In the previous model, the thicknesses of the Ni sheet and the dielectric insulation were *both* taken to be 300 micron. In the present case, however, there is a great disparity between these two thicknesses – the Ni sheet is 50 - 100 micron thick whereas the insulation will be ~ 10 - 20 micron thick (or possibly even less in the sputtered case). Thus, other things being equal, the transverse thermal conductance across the insulation will be > 30 times larger than in the previously modeled case.

- Finally, the heat transfer coefficient between the HTS tape and the coolant may be worth re-examining as the assumed value here drove the modeling results in the Phase II program. In a program on storing energy in capacitors at 77 K, CeramPhysics measured the heat transfer between some ceramic surfaces and liquid nitrogen, and it was found that a few silvered spots on the ceramic surface dramatically *increased* the heat transfer. Presumably some Ag could be sputtered atop the dielectric insulation to achieve this same effect.

TABLE III-I

Thermal Conductivity, Specific Heat, and Thermal Diffusivity Data

Units: T, Temperature, K; K, Thermal Conducitivity, mW cm^{-1} K^{-1}; C_v, Volumetric Specific Heat, J cm^{-3} K^{-1}; k, Thermal Diffusivity, 10^{-3} cm^2 s^{-1}

GLASS			
T	K	Cv	k
60	1.807	0.370	4.884
65	1.945	0.410	4.744
70	2.083	0.450	4.629
75	2.221	0.484	4.589
80	2.360	0.519	4.547
85	2.498	0.561	4.453
90	2.636	0.603	4.371
95	2.774	0.641	4.328
100	2.912	0.680	4.282

60NN			
T	K	Cv	k
60	21.245	0.397	53.55
65	21.479	0.450	47.78
70	21.713	0.502	43.23
75	21.947	0.562	39.04
80	22.181	0.618	35.91
85	22.414	0.676	33.15
90	22.648	0.735	30.834
95	22.882	0.791	28.92
100	23.116	0.848	27.244

Zn_2GeO_4			
T	K	Cv	k
60	2.9536E+02	5.3793E-01	5.4907E+02
65	2.6780E+02	5.9583E-01	4.4946E+02
70	2.4024E+02	6.4816E-01	3.7065E+02
75	2.3079E+02	7.0298E-01	3.2830E+02
80	2.1661E+02	7.5780E-01	2.8585E+02
85	2.0244E+02	8.1261E-01	2.4912E+02
90	1.8827E+02	8.6743E-01	2.1704E+02

CRYOVARISTOR			
T	K	Cv	k
60	0.595×10^3	0.711	0.837×10^3
65	0.604×10^3	0.782	0.772×10^3
70	0.612×10^3	0.853	0.717×10^3
75	0.612×10^3	0.911	0.672×10^3
80	0.612×10^3	0.968	0.632×10^3
85	0.612×10^3	1.068	0.573×10^3
90	0.612×10^3	1.172	0.522×10^3
95	0.612×10^3	1.299	0.471×10^3

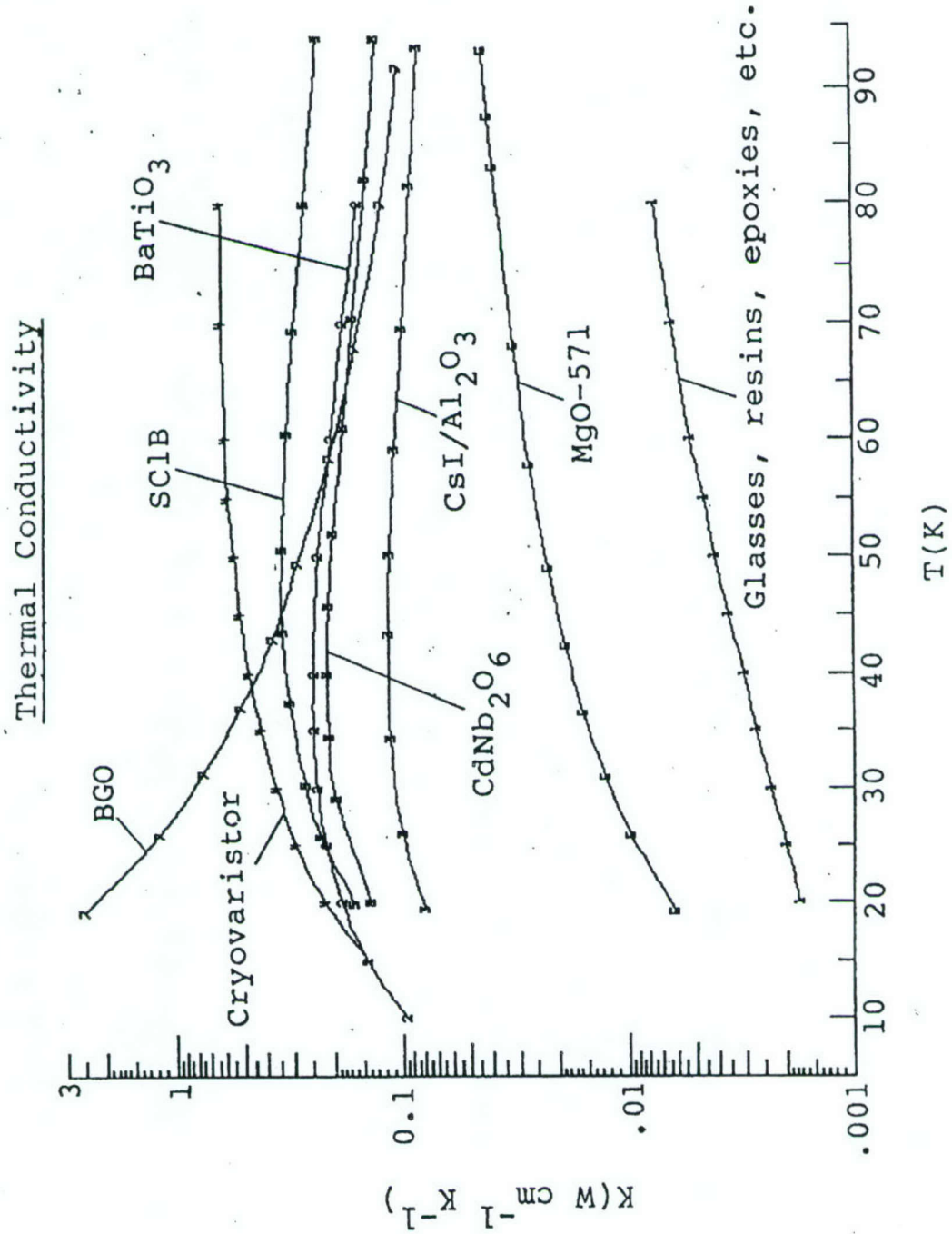
Thermal Conductivity
BGO
Cryovaristor
SC1B
BaTiO3
CdNb2O6
CsI/Al2O3
MgO-571
Glasses, resins, epoxies, etc.
K(W cm-1 K-1)
3
1
0.1
.01
.001
10
20
30
40
50
60
70
80
90
T(K)

FIGURE III-1

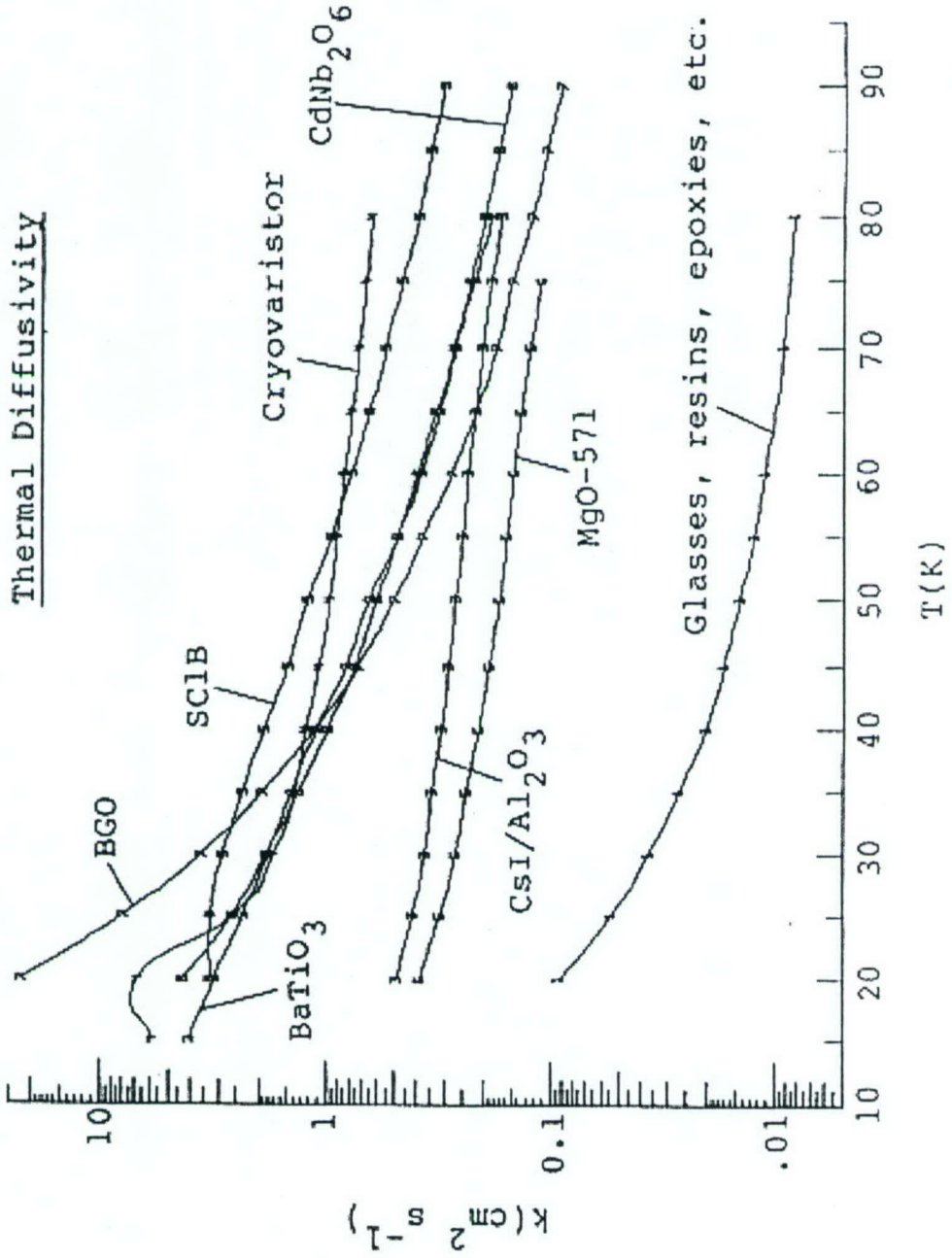
Thermal Diffusivity
BGO
SC1B
BaTiO3
Cryovaristor
CdNb2O6
CsI/Al2O3
MgO-571
Glasses, resins, epoxies, etc.
10
1
0.1
.01
κ(cm2 s-1)
10
20
30
40
50
60
70
80
90
T(K)

FIGURE III-2

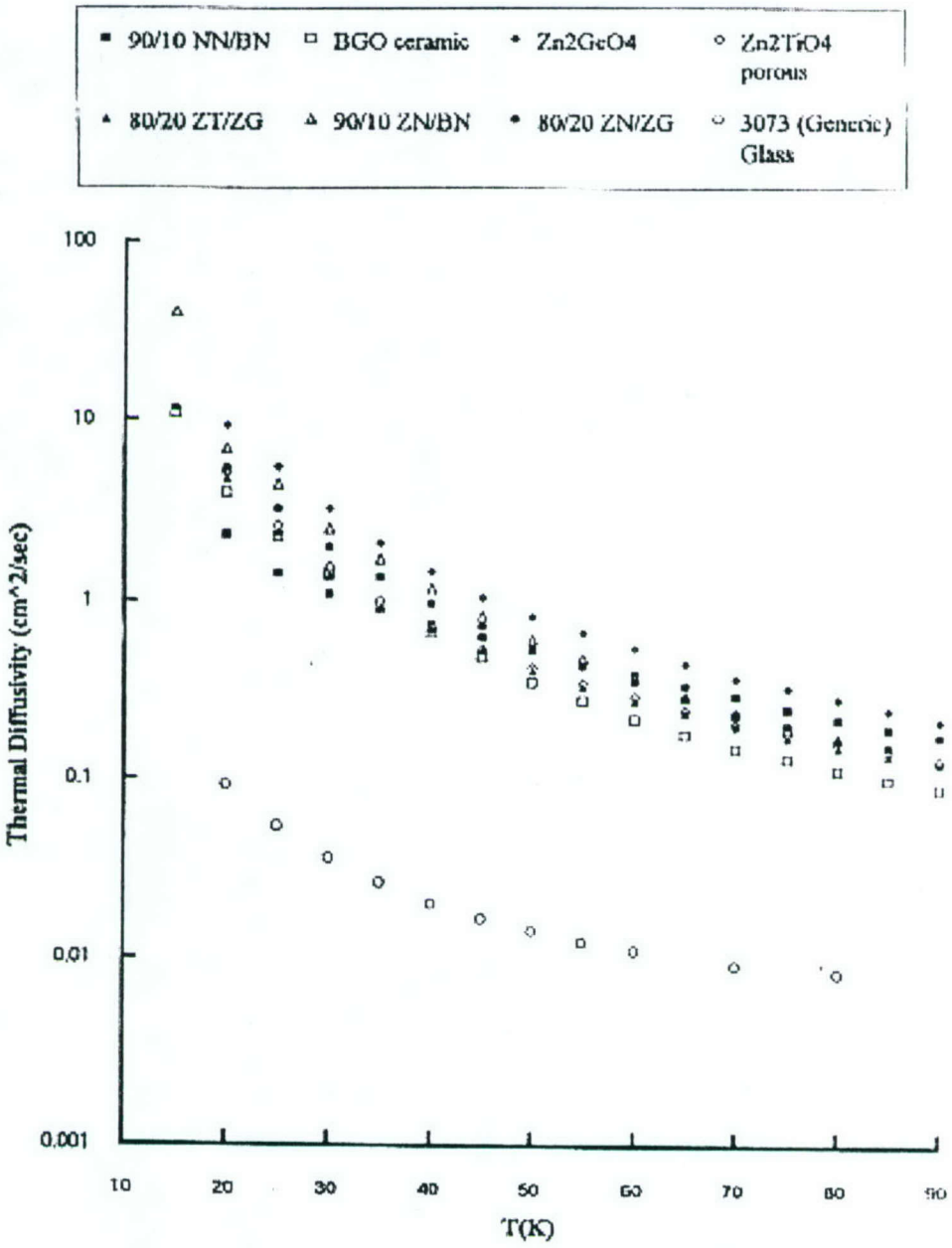
90/10 NN/BN
BGO ceramic
Zn2GeO4
Zn2TiO4 porous
80/20 ZT/ZG
90/10 ZN/BN
80/20 ZN/ZG
3073 (Generic) Glass
Thermal Diffusivity (cm^2/sec)
100
10
1
0.1
0.01
0.001
10
20
30
40
50
60
70
80
90
T(K)

FIGURE III-3

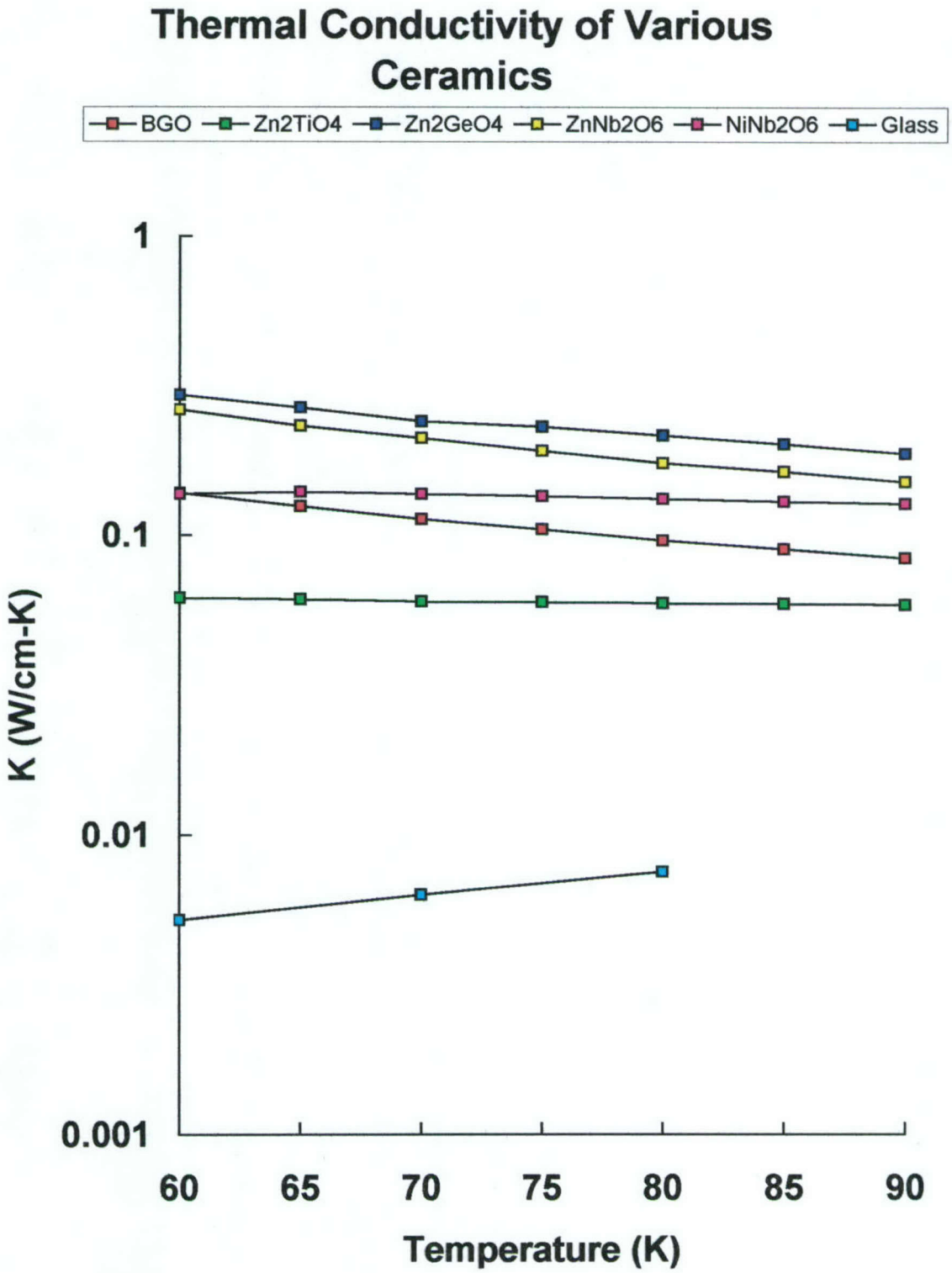
Thermal Conductivity of Various Ceramics
BGO
Zn2TiO4
Zn2GeO4
ZnNb2O6
NiNb2O6
Glass
1
0.1
0.01
0.001
K (W/cm-K)
60
65
70
75
80
85
90
Temperature (K)

FIGURE III-4

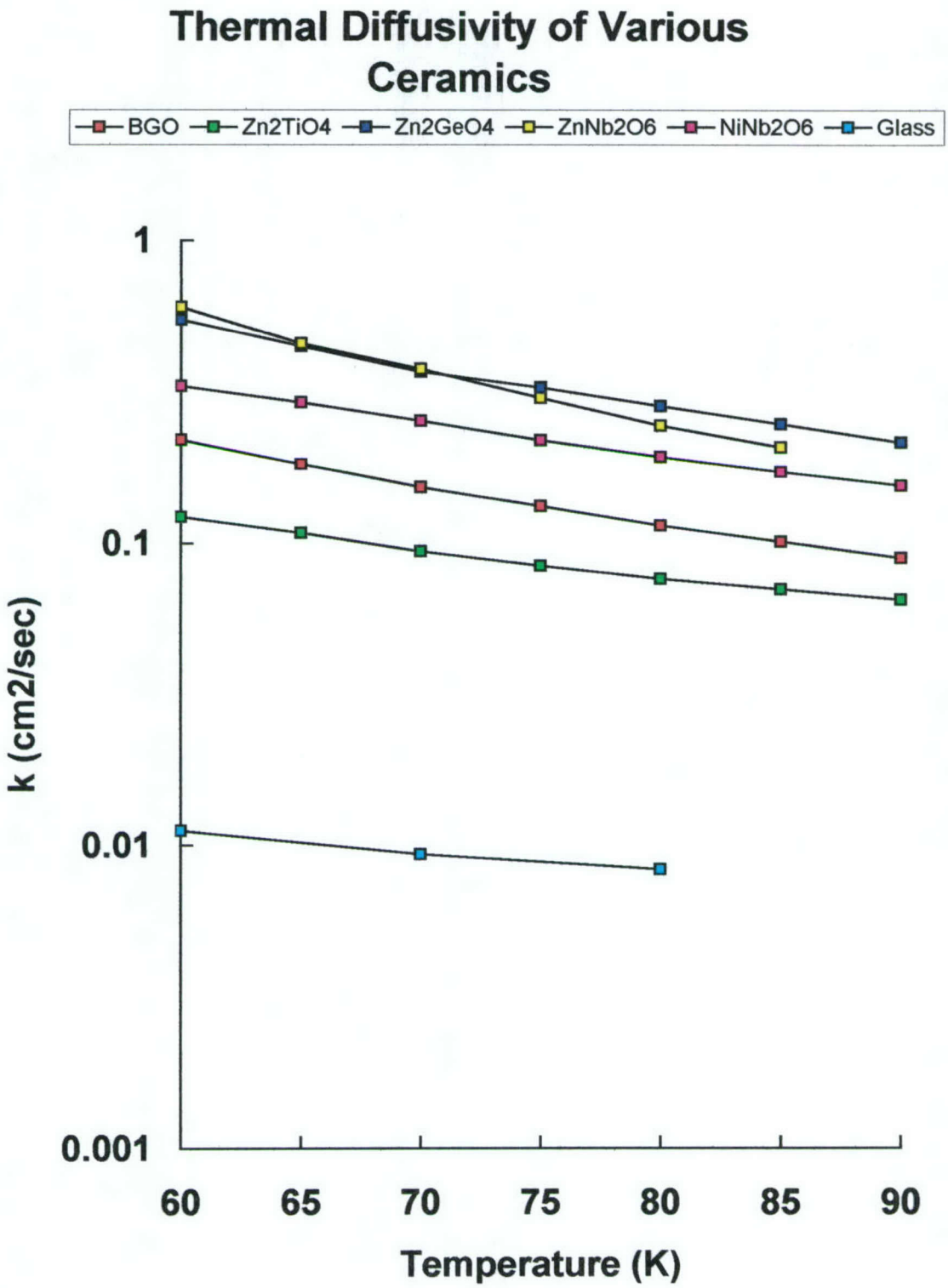
Thermal Diffusivity of Various Ceramics
BGO
Zn2TiO4
Zn2GeO4
ZnNb2O6
NiNb2O6
Glass
1
0.1
0.01
0.001
k (cm2/sec)
60
65
70
75
80
85
90
Temperature (K)

FIGURE III-5

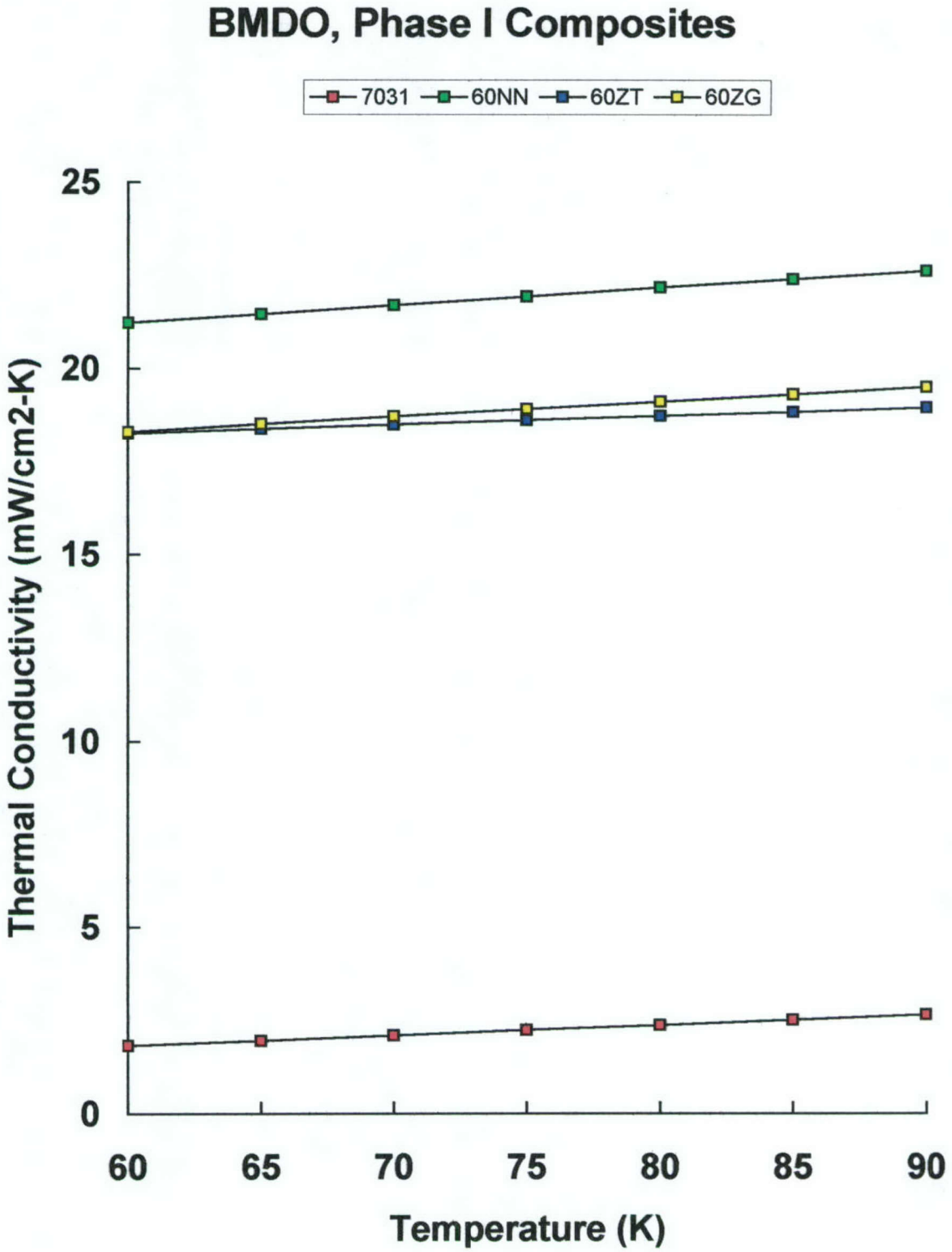
BMDO, Phase I Composites
7031
60NN
60ZT
60ZG
Thermal Conductivity (mW/cm2-K)
25
20
15
10
5
0
60
65
70
75
80
85
90
Temperature (K)

FIGURE III-6

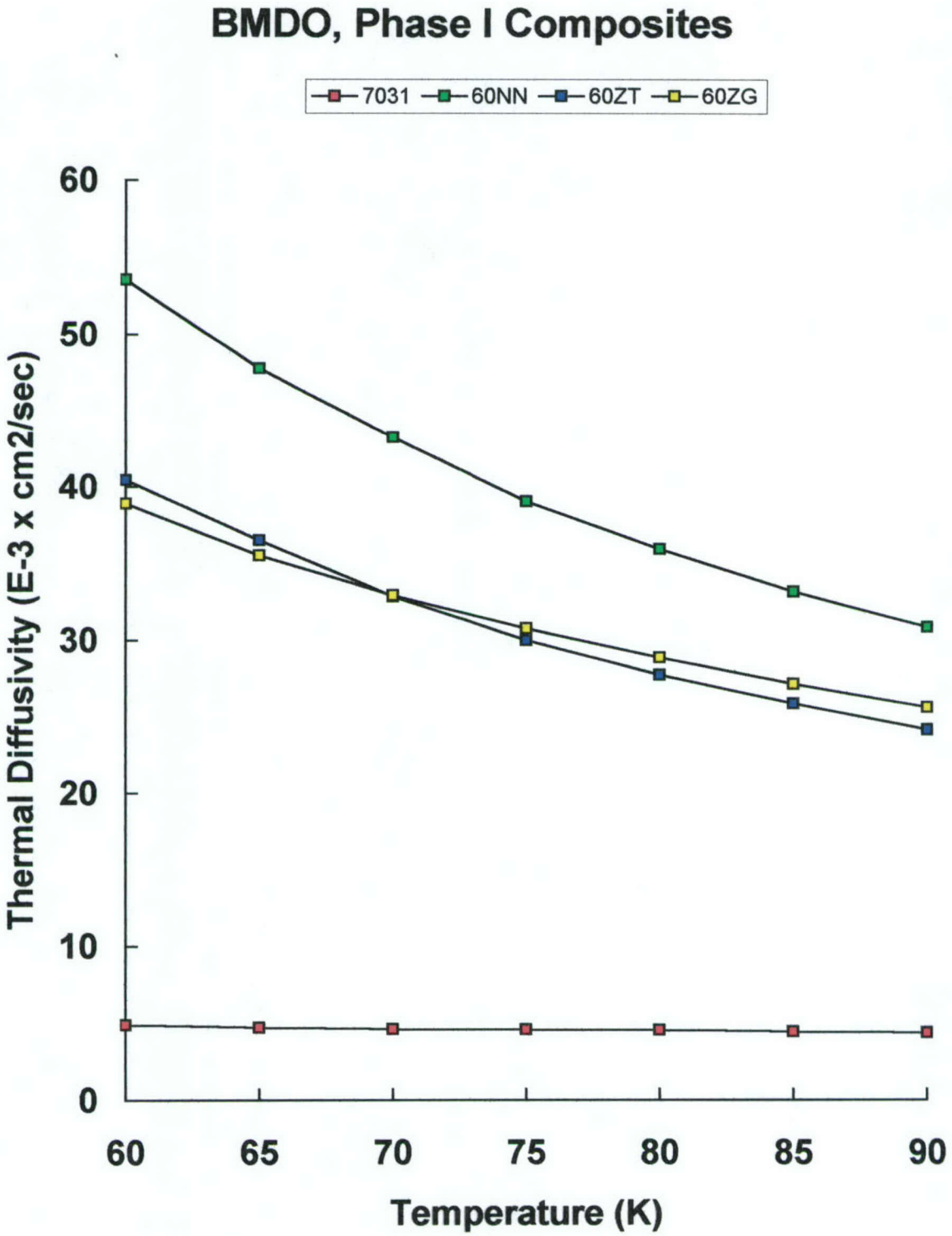
BMDO, Phase I Composites
7031
60NN
60ZT
60ZG
Thermal Diffusivity (E-3 x cm2/sec)
60
50
40
30
20
10
0
60
65
70
75
80
85
90
Temperature (K)

FIGURE III-7

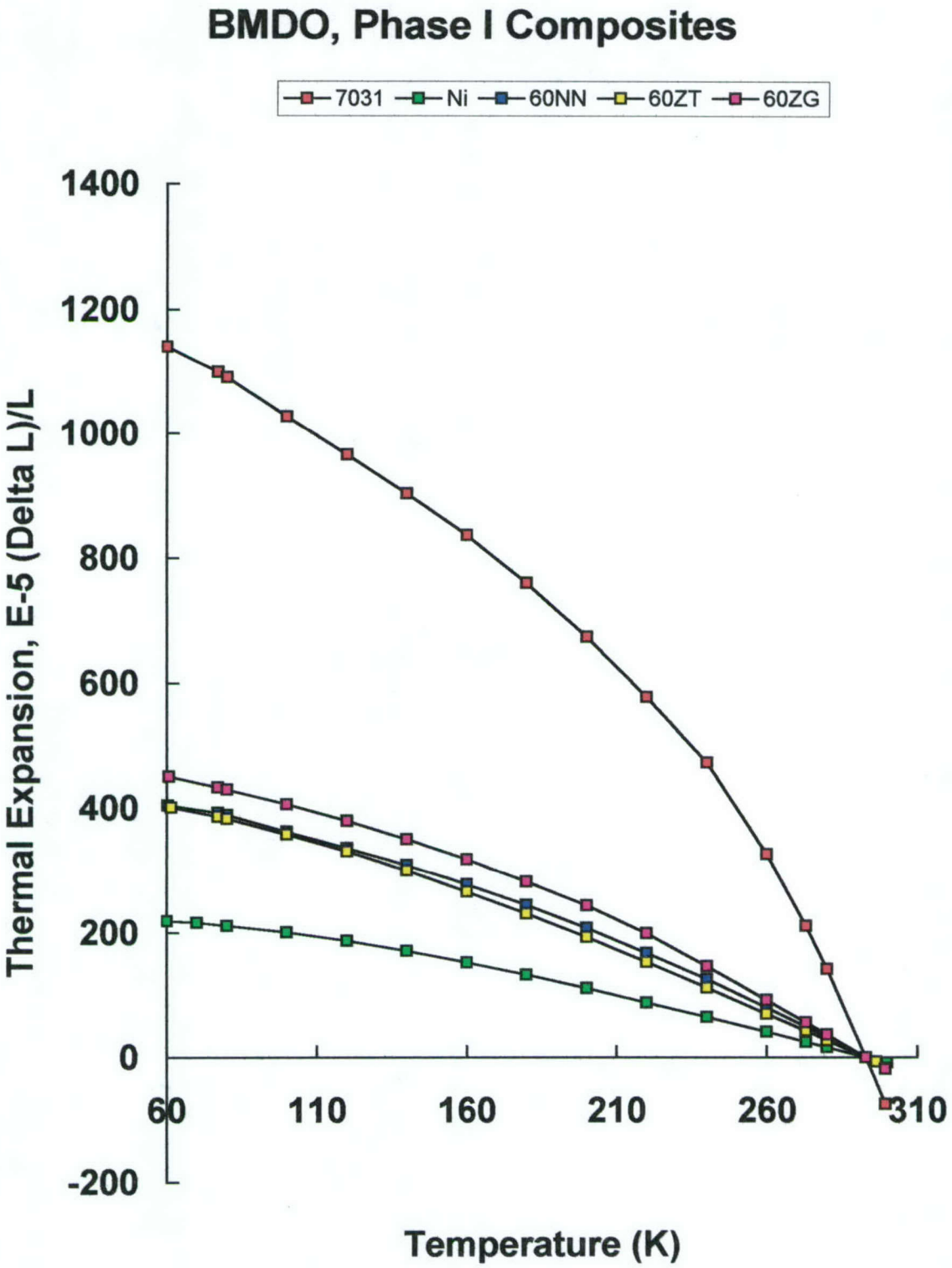
BMDO, Phase I Composites
7031
Ni
60NN
60ZT
60ZG
1400
1200
1000
800
600
400
200
0
-200
Thermal Expansion, E-5 (Delta L)/L
60
110
160
210
260
310
Temperature (K)

FIGURE III-8

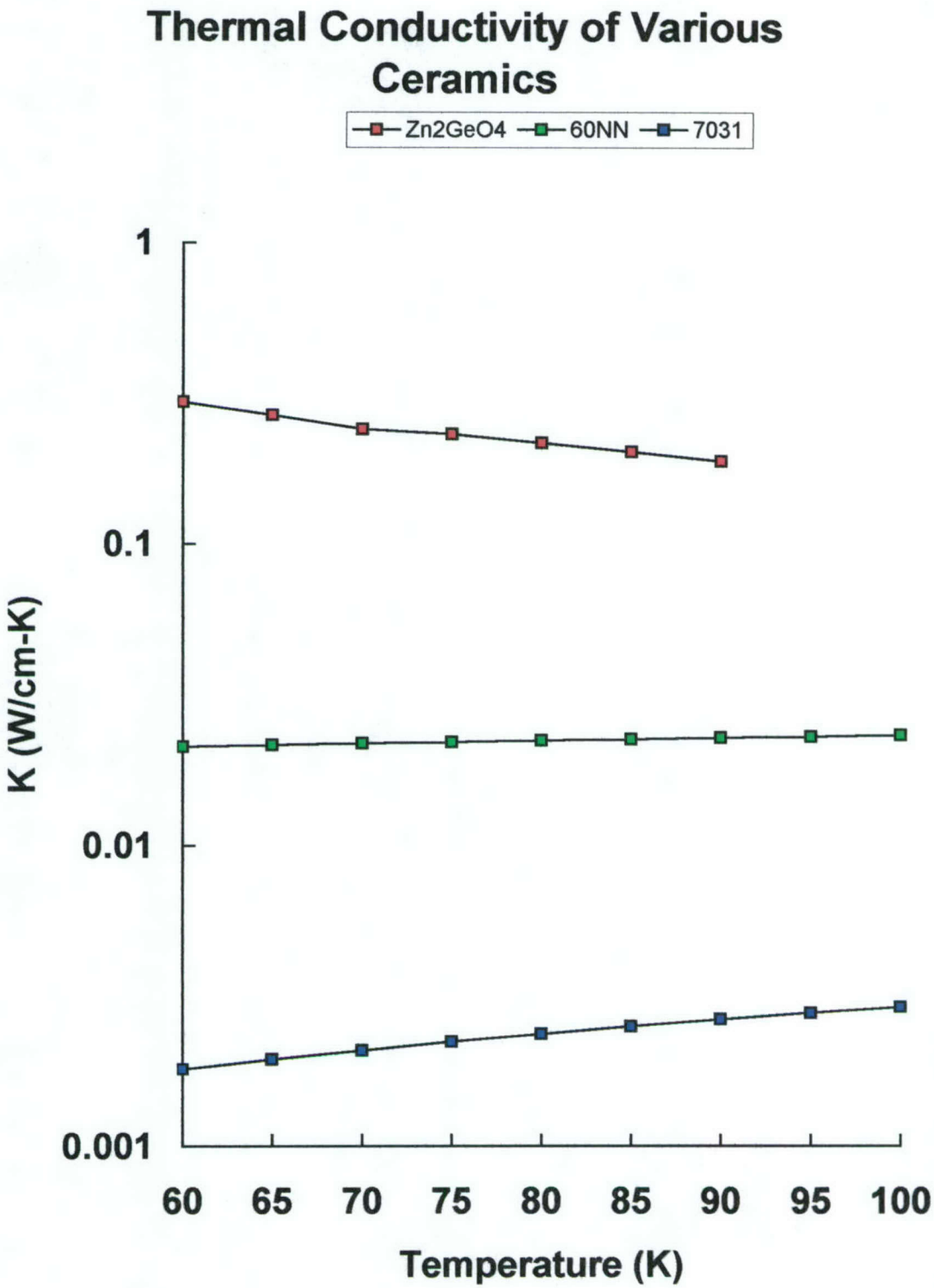
Thermal Conductivity of Various Ceramics
Zn2GeO4
60NN
7031
1
0.1
0.01
0.001
K (W/cm-K)
60
65
70
75
80
85
90
95
100
Temperature (K)

FIGURE III-9

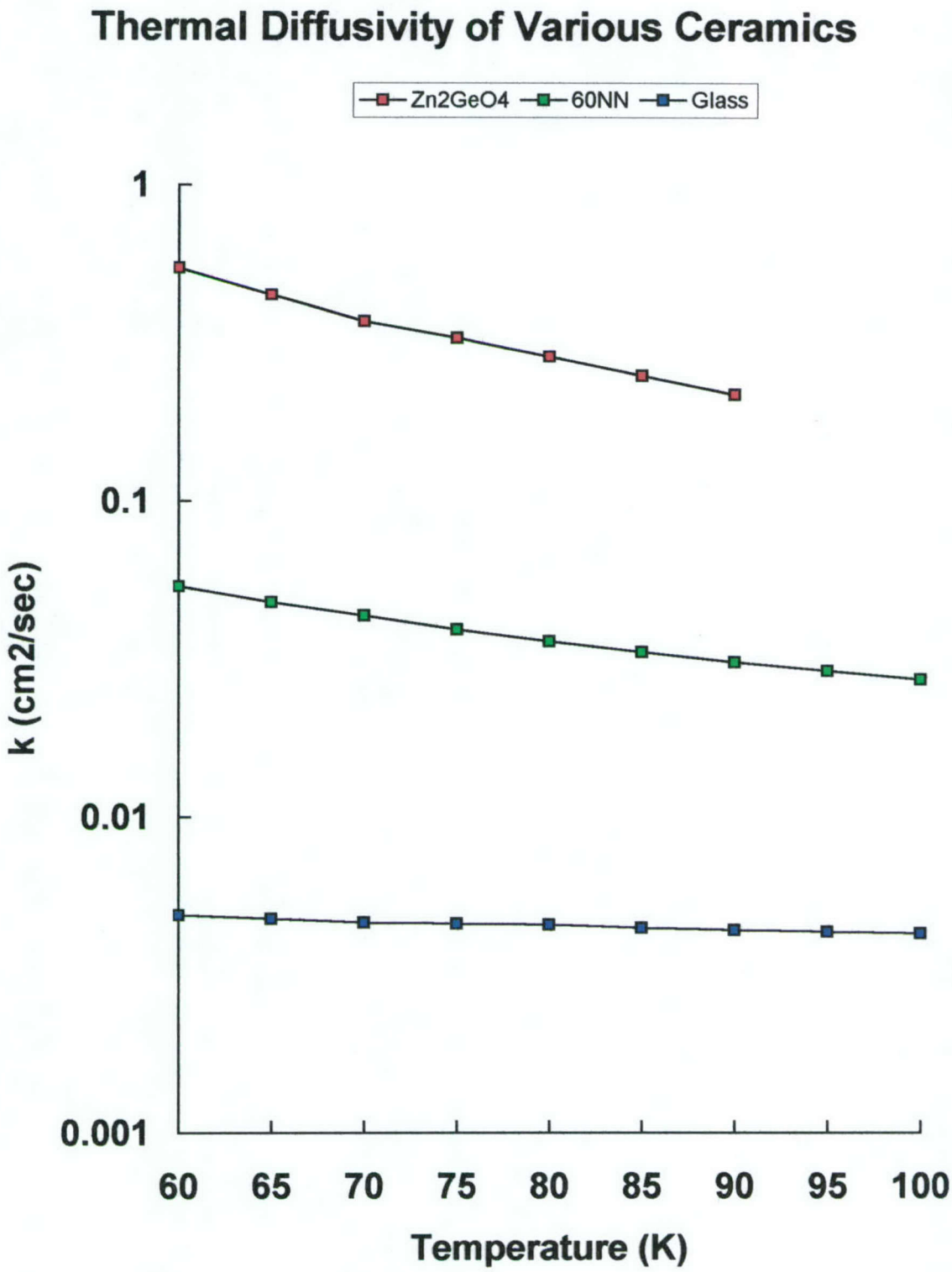

FIGURE III-10

IV. ASSESSMENT OF DIAMOND FILMS

A. INTRODUCTION

Adequate quench protection would allow HTS magnets to operate at temperatures near 77 K, and this would have the very beneficial effect of reducing the size, cost, and complexity of the refrigeration.

A possible scenario for quench protection is to provide a dielectric insulation with a large thermal conductivity, and one approach currently being investigated is the use of diamond films. The motivation here comes from the large thermal conductivity of (single-crystal) diamond at low temperatures.

However, the distribution of phonon path lengths will be considerably different in a thin diamond film than in a single crystal, and this could potentially compromise the thermal conductivity of the film. There is a basic conundrum in measuring the thermal conductivity (or thermal diffusivity) of a film: If the film thickness (e.g., ~ 5 microns) is much *smaller* than the substrate thickness (e.g., ~ 250 microns), then the separation of the film contribution from the measured quantity is subject to a large uncertainty. On the other hand, if a *thick* film were used (e.g., ~ 50 micron), then the distribution of phonon path lengths would not apply to a thinner film.

The purpose of the study here is to examine the phonon distribution in diamond films based on solid-state models for thermal conduction in solids. Measured data on diamond single crystals will be used, and the goal is to make a projection of the thermal conductivities that can be expected in these films. Projections of thermal diffusivities in the films will also be made for modeling purposes at the Univ. of Pittsburgh.

B. REVIEW OF THERMAL CONDUCTION IN SOLIDS

Dominant-Phonon Approximation

One of the most useful descriptions of thermal conductivity in solids is the dominant-phonon approximation [1],

$$K \simeq \rho C v \lambda / 3 \qquad \text{(IV-1)}$$

where v is the average sound velocity and λ is the (dominant) phonon mean free path (i.e., mean free path between scattering events). In Eq. (IV-1), C is the specific heat of the heat-carrying modes; for example, localized defects do not generally carry heat, so the contributions to the specific heat from such defects cannot be included in C in Eq. (IV-1). Equation (IV-1) shows that large thermal conductivities and large specific heats often go hand-in-hand, other things being equal.

Phonon scattering plays the <u>dominant</u> role in thermal conductivity, and this enters Eq. (IV-1) through the mean free path λ (sound velocities, v, do not differ greatly from solid to solid and are essentially temperature independent). The mean free path is determined by three scattering processes: phonon-phonon scattering, geometric (or

boundary) scattering, and phonon-defect scattering, each of which becomes important in different temperature regions.

Phonon-phonon scattering generally dominates at higher temperatures (we shall see below what is considered "higher" temperatures) where the mean free path follows the Peierls relation [2]

$$\lambda \propto \exp(\theta/2T) \qquad \text{(IV-2)}$$

where θ is the Debye temperature. Since the specific heat becomes essentially temperature independent at higher temperatures, it follows from Eq. (IV-1) that K also becomes proportional to exp (θ/2T) at these temperatures, and this is the Region 1 illustrated schematically in Fig. IV-1.

The thermal conductivity has a maximum as shown in Fig. IV-1, and this maximum generally always occurs at low temperatures. There are two phenomena which eventually overwhelm the strong temperature dependence of λ in Eq. (IV-2) and give rise to this maximum. First, the specific heat C in Eq. (IV-1) decreases rapidly with decreasing temperature at low temperatures; and second, the mean free path becomes limited by *boundary scattering*. These two effects dominate the thermal conductivity in Region 2 in Fig. IV-1.

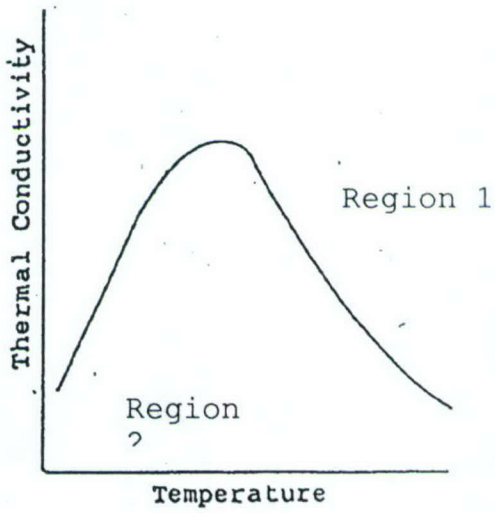

Figure IV-1. *Schematic illustration of the temperature dependence of the thermal conductivity.*

The mean free path according to Eq. (IV-2) is very long at low temperatures -- e.g., at, say 4 K, λ is on the order of millimeters. Thus, as λ increases with decreasing temperature, a condition is reached where phonons scatter from the physical boundary of the sample -- hence the name boundary scattering -- and λ becomes fixed by the physical dimension of the sample and is no longer given by Eq. (IV-2).

The physical dimension of the sample limits the thermal conductivity via boundary scattering, and this is why thin diamond films will have depressed thermal conductivities compared to single-crystal diamond. Estimating thin-film thermal conductivities is the goal of this study.

There is a *distribution* of phonon free paths due to scattering, and λ is the mean of this distribution. As the temperature is decreased, the longest free paths first become limited by boundary scattering, followed by the shorter paths, until eventually all free paths become boundary limited. Thus, Eq. (IV-2) becomes invalid when boundary scattering first occurs, and an example of this will be given below.

Finally, the scattering of phonons by defects decreases λ and thereby the thermal conductivity also. This is a very complicated problem in solid-state physics [3] and depends on the type of defects involved, their spatial distribution, and scattering cross section. Near room temperature where λ is very short (i.e., on the order of unit cell dimensions), defects have very little effect on thermal conductivity. And at the other extreme of very low temperatures, mean free paths are too long to "see" defects (except in the case of resonance scattering).

To complete this review, the specific heat C that enters Eq. (IV-1) is given by the Debye relation [1],

$$C = 3nRf(\theta/T) \qquad \text{(IV-3)}$$

where n is the number of atoms per formula weight (n = 1 for diamond), R is the gas constant, θ is the Debye temperature, and $f(\theta/T)$ is the Debye function. Therefore, the Debye temperature plays a central role in the thermal conductivity by entering Eq. (IV-1) via Eq. (IV-2) for the phonon mean free path and also via Eq. (IV-3) for the specific heat C which enters Eq. (IV-1).

Examples of Thermal Conductivities at Low Temperatures

It is instructive to examine some examples of thermal conductivities at low temperature which illustrate the topics discussed above and also introduce the thermal properties of diamond at low temperatures.

In Fig. IV-2 are shown thermal conductivity data for single crystals of diamond and sapphire and for alumina [4] Three important features are evident in Fig. IV-2: First, sapphire has a larger thermal conductivity than diamond below 70 K; second, the maximum in the thermal conductivity of diamond occurs at a higher temperature (90 K) than the maximum for sapphire (30 K); and third, the thermal conductivity of sintered alumina is about two orders of magnitude smaller than for sapphire (which is a crystalline form of alumina).

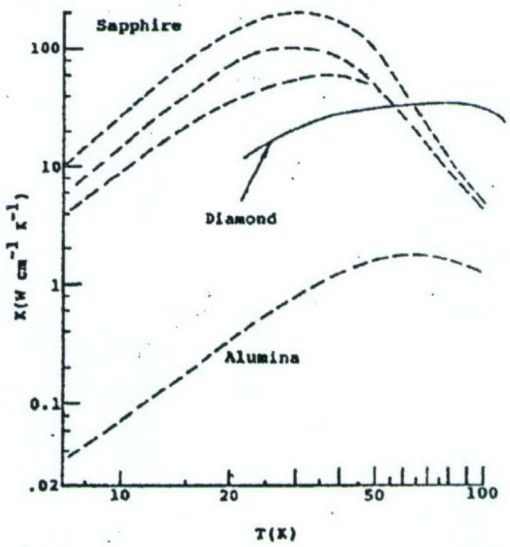

Figure IV-2. Thermal conductivity data for sapphire, diamond, and sintered alumina, 7-100 k.

These features are understandable in terms of the discussion above, as follows: The Debye temperature for diamond is 1940 K compared to 1030 K for alumina [5], and this explains why the K-maximum for diamond occurs at a higher temperature compared to sapphire -- i.e., as the Debye temperature increases, both λ and C shift to smaller values, and from Eqs.(IV-1) - (IV-3) this has the effect of shifting the curve in

Fig. IV-1 to higher temperatures. A corollary here is the fact that diamond has a larger thermal conductivity at room temperature than sapphire.

The magnitude of the maximum thermal conductivity for diamond is less than that for sapphire in Fig. IV-2, and this is due primarily to the difference in specific heats of the two materials in Eq. (IV-1). In Eq. (IV-2), n = 1 and 5 for diamond and sapphire, respectively, and, given the two Debye temperatures, the Debye function at, say, 50 K for sapphire is seven times larger than that for diamond (The Debye function is tabulated in reference 5). These two effects amplify the specific-heat difference by about 35 times according to Eq. (IV-3).

The average sound velocity in diamond is 13.4×10^5 cm/s compared to 7.0×10^5 cm/s for sapphire [1]. Therefore, collecting all these factors in Eq. (IV-1) we expect the thermal conductivity of diamond at low temperatures to be about 20 times smaller than that of sapphire, and this is in reasonably good agreement with the data in Fig. IV-2.

The thermal conductivity of sintered alumina in Fig. IV-2 is considerably smaller than that of sapphire, and the K-maximum for alumina occurs at a higher temperature (70 K compared to 30 K, respectively). These two facts are related and are due to the *grain size* in the alumina sample, ~ 30 micron [4], which determines the boundary-scattering limit rather than the much larger sample dimensions. Therefore, the boundary-limited phonon mean free path in sintered alumina is *much smaller* than in sapphire, and this both suppresses the magnitude of the thermal conductivity and shifts the K-maximum to higher temperatures, according to the discussion above.

Therefore, the thermal conductivity data in Fig. IV-2 provide excellent examples of the thermal properties at low temperatures discussed above.

C. THERMAL CONDUCTIVITY OF DIAMOND FILMS

The thermal conductivity data for diamond in Fig. IV-2 is over a narrow temperature range, and in Fig. IV-3 are shown these data over the range 20 to 300 K. These are composite data measured on four single crystals of diamond where the width of the crystals varied from 1.1 to 3.9 mm [4] and there is essentially no variation in these four data sets.

The data in Fig. IV-3 were analyzed for the phonon mean free path using Eq. (IV-1), as follows: The specific heat was obtained from Eq. (IV-3) using the Debye temperature quoted above and the tabulation of the Debye function in Ref. 5. For the density of diamond the handbook value 3.52 g/cc was used, and the sound velocity quoted above was used (sound velocities in solids are essentially temperature independent).

The phonon mean free path data determined for diamond in this fashion are shown in Fig. IV-4 plotted according to Eq. (IV-2). The data follow Eq. (IV-2) very well down to about 110 K (shown by the dashed line in Fig. IV-4) but deviate substantially at lower temperatures; this is due to the effect of boundary scattering on the *distribution* of phonon scattering lengths discussed above.

The data in Fig. IV-4 are shown in Fig. IV-5 to lower temperatures (5 K) to illustrate the smooth *extrapolation* of the phonon mean free path data to the (average) width of the diamond crystals (2.5 mm) at the lowest temperatures.

We now use the data in Figs. IV-4 and IV-5 to estimate the thermal conductivity of diamond films by the following argument: We assume that the temperature dependence of the phonon mean free path in Fig. IV-4 for diamond crystals can be *scaled* to diamond films using the *ratio* of the film thickness to the average crystal width. For example, for a film thickness of 10 micron, the scale factor is 0.001 cm/0.25 cm = 0.0040 and applies equally to all the diamond-crystal data in Fig. IV-4. The rationale for this simplifying assumption is that as the film thickness decreases, the phonons with longer path lengths become increasingly removed from the distribution which causes the distribution to shift to ever smaller path lengths. This assumption satisfies the two boundary conditions -- that at the higher temperatures Eq. (IV-2) is followed, and at the lowest temperatures the phonon mean free path approaches the film thickness.

Because K is proportional to λ in Eq. (IV-1), thermal conductivity data for films are easily estimated by multiplying the single-crystal data in Fig. IV-3 by the scale factor. Three film thicknesses were adopted, 10, 20, and 50 microns, and the estimated thermal conductivities of these films are shown in Fig. IV-6. Also shown for comparison are data for the ceramic Zn_2GeO_4, and we shall return to this material below.

Finally, thermal diffusivity data (k = K/C) for the diamond films are estimated using the data in Fig. IV-6 and the volumetric specific heat data for diamond. These latter data were determined earlier to analyze the data in Fig. IV-4, and in Fig. IV-7 are shown these thermal diffusivity data. Again, data for Zn_2GeO_4 are also shown.

D. DISCUSSION AND CONCLUSIONS

A review of thermal conduction in solids at low temperatures has been given based on accepted models for the thermal conductivity, phonon mean free path, and specific heat of solids. Literature data for sapphire, diamond, and alumina provide good examples which can be understood in terms of these models.

Literature data for diamond crystals are analyzed for the temperature dependence of the phonon mean free path, and these phonon-path data are scaled by a geometric argument to estimate the suppression of the thermal conductivities of diamond *films* due to boundary scattering. Film thicknesses of 10, 20, and 50 micron thicknesses are adopted, and the estimated thermal conductivities of these films are about 250, 120, and 50 times smaller at 70 K than the thermal conductivity of single-crystal diamond, respectively. It is interesting that these suppression factors are in approximate agreement with the suppression of the thermal conductivity of alumina compared to sapphire in Fig. IV-2.

The scaling assumption made in order to estimate the phonon mean free path in diamond films from the single-crystal data is a necessary assumption, given the information available. Phonon scattering in solids is a complex problem in solid-state physics, and the high-temperature expression for the mean free path in Eq. (IV-2) agrees

functionally with experiment but not quantitatively. For example, if the exponent in Eq. (IV-2) is written as exp(θ/cT), it is found that c varies from 2. A fit to the linear data in Fig. IV-4 for diamond yields c = 2.7, and for sapphire c = 2.1 [8].

We conclude that boundary scattering suppresses the thermal conductivity of diamond films into the 0.1 - 0.7 W cm^{-1} K^{-1} range at low temperatures, and therefore diamond films may *not* be more attractive than alternate ceramic films for quench protection.

A case in point here is the Zn_2GeO_4 ceramic shown in Figs. IV-6 and IV-7 [6]. The ceramic bar used for these measurements was prepared by NexTech Mat'ls Ltd. and had a grain size of 1-5 micron (S. Swartz, private communication) which determined the boundary scattering limit. Therefore, it is anticipated that a thin sputtered film of this ceramic would have the same thermal conductivity shown in Fig. IV-6.

The Zn_2GeO_4 data on the ceramic bar in Fig. IV-6 suggests that a single crystal of this material would have a very large thermal conductivity at low temperatures. This is probably the case indeed because a single crystal of Bi_2GeO_4 (Harshaw Chemical) has a very large thermal conductivity, 3 W cm^{-1} K^{-1} at 20 K, and the maximum in K occurs below 20 K [7].

Finally, thermal conductivity and thermal diffusivity data are tabulated below for the three diamond films for computer modeling purposes at the Univ. of Pittsburgh.

References

1. C. Kittel, *Introduction to Solid State Physics*, Ch. 6 (John Wiley & Sons, New York, Third Edition, 1966).
2. R. Peierls, Ann. Physik **3**, 1055 (1929).
3. P. G. Klemens, Proc. Roy. Soc. (London) **A208**, 108 (1951).
4. NBS Monograph 131, *Thermal Conductivity of Solids at Room Temperature and Below*, US Dept. of Commerce, 1973.
5. E. S. R. Gopal, *Specific Heats at Low Temperatures* (Plenum Press, New York, 1966).
6. W.N. Lawless, Final Report, *Thermal Stabilization of Ceramic Superconductors for Aerospace Pulsed Power*, Phase II SBIR, Air Force Contract F33615-92-C-2286, July 25, 1994.
7. W. N. Lawless, Final Report, *Thermal Stabilization of Ceramic Superconductors for Aerospace Pulsed Power,* Phase I SBIR, Air Force Contract F33615-91-C-2122, September 12, 1991.
8. R. Berman et al., Nature **168**, 277 (1951).

Table IV-I

Projected Thermal Conductivities of Diamond Films, W cm^{-1} K^{-1}

T, K	10 micron	20 micron	50 micron
40	0.111	0.222	0.556
50	0.123	0.245	0.613
60	0.132	0.263	0.658
70	0.133	0.267	0.667
80	0.136	0.272	0.680
90	0.133	0.267	0.667
100	0.121	0.242	0.604

Table IV-II

Projected Thermal Diffusivities of Diamond Films, cm^2 s^{-1}

T, K	10 micron	20 micron	50 micron
40	22.23	44.45	111.1
50	12.61	25.22	63.06
60	7.83	15.66	39.15
70	4.97	9.94	24.85
80	3.40	6.81	17.02
90	2.34	4.68	11.70
100	1.55	3.10	7.75

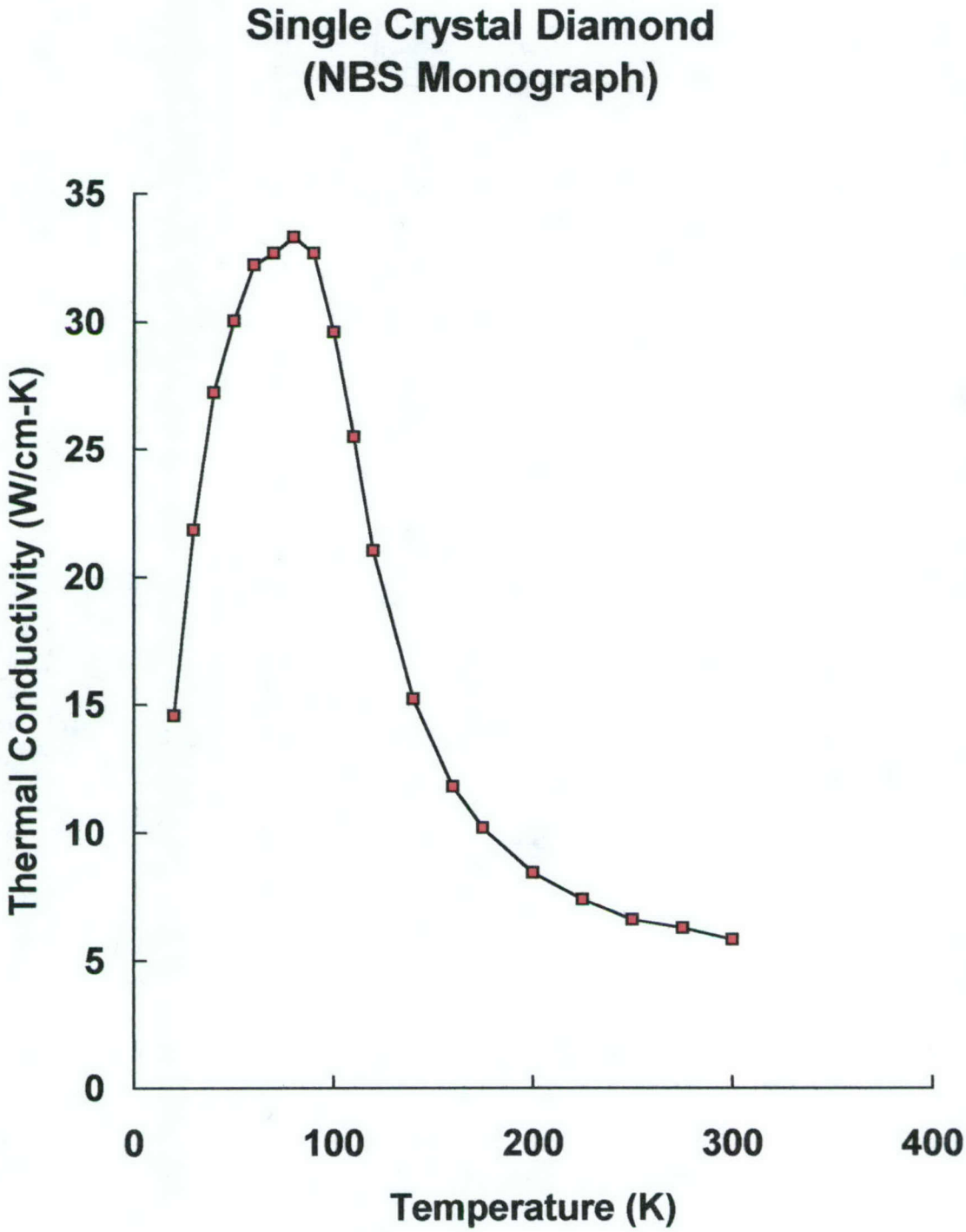
Single Crystal Diamond
(NBS Monograph)
Thermal Conductivity (W/cm-K)
35
30
25
20
15
10
5
0
0
100
200
300
400
Temperature (K)

FIGURE IV-3

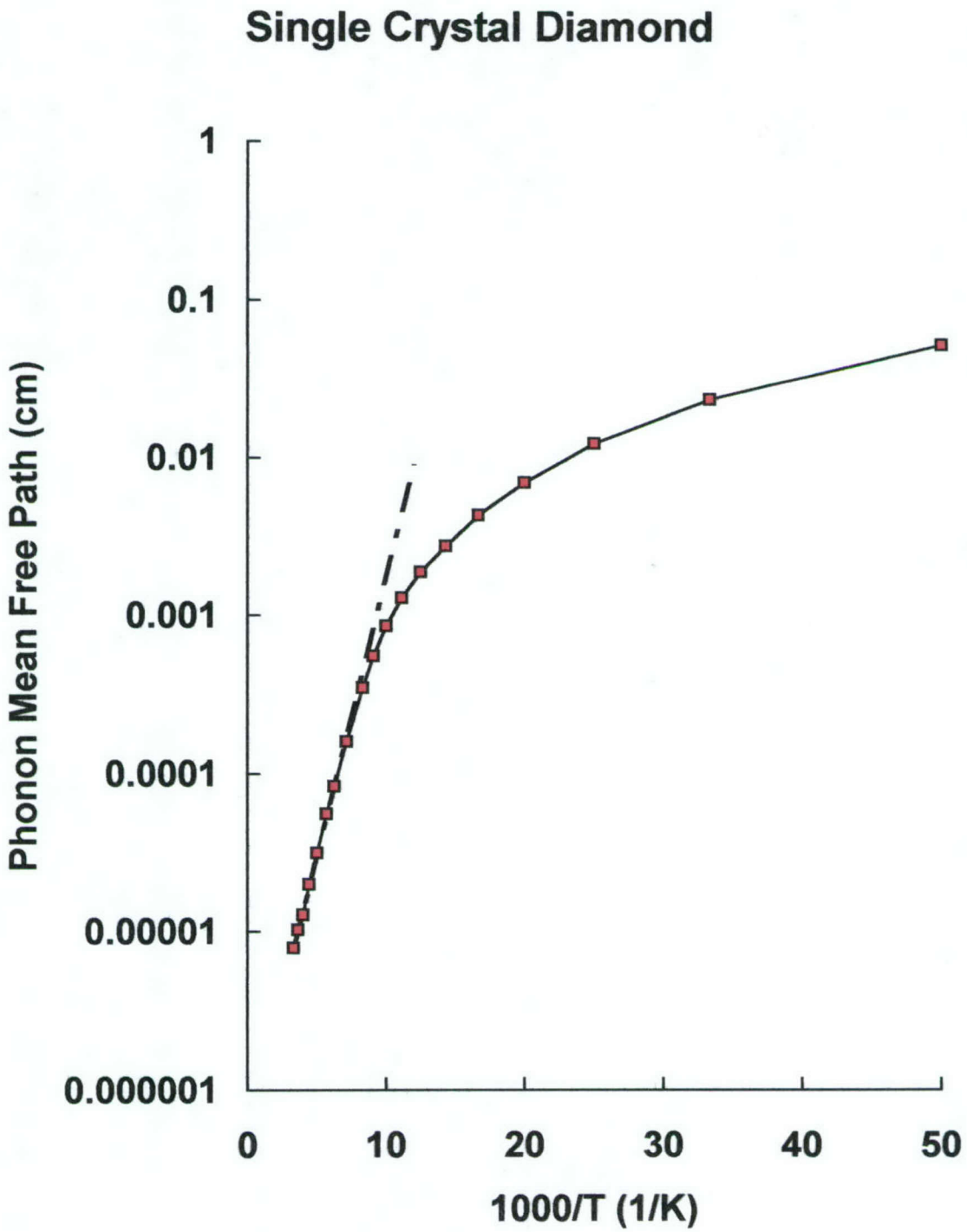
Single Crystal Diamond
Phonon Mean Free Path (cm)
1
0.1
0.01
0.001
0.0001
0.00001
0.000001
0
10
20
30
40
50
1000/T (1/K)

FIGURE IV-4

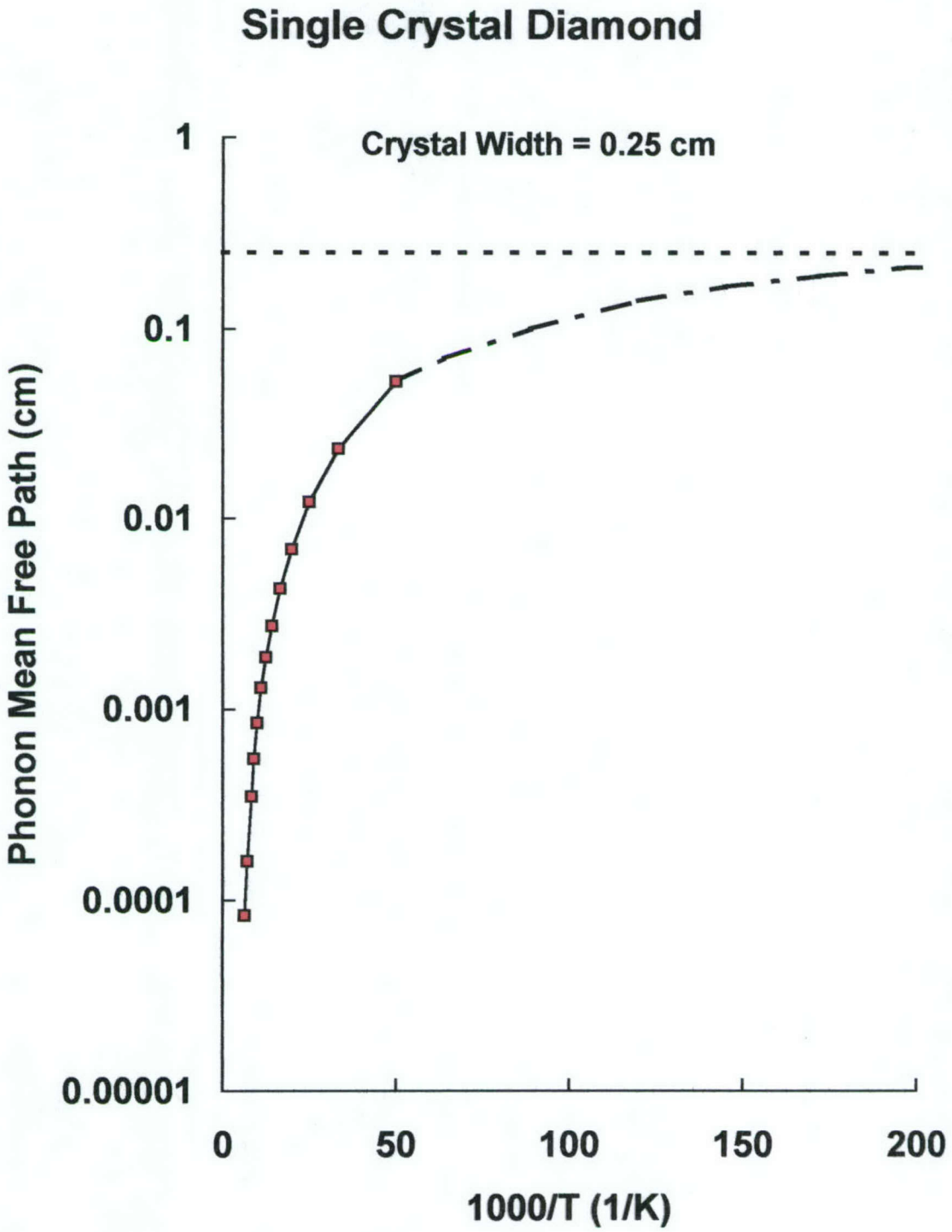
Single Crystal Diamond
Crystal Width = 0.25 cm
1
0.1
0.01
0.001
0.0001
0.00001
Phonon Mean Free Path (cm)
0
50
100
150
200
1000/T (1/K)

FIGURE IV-5

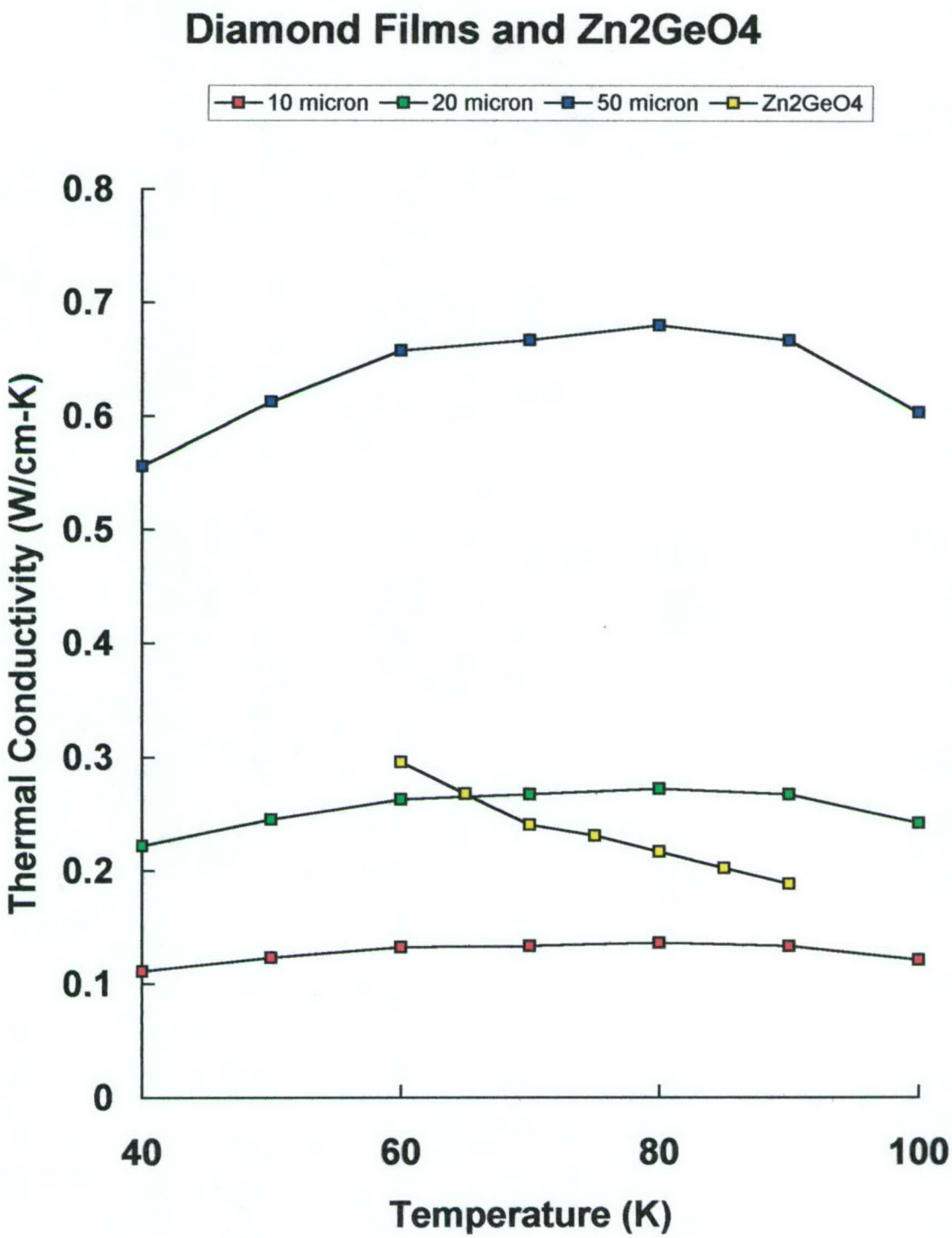
Diamond Films and Zn2GeO4
10 micron
20 micron
50 micron
Zn2GeO4
Thermal Conductivity (W/cm-K)
0.8
0.7
0.6
0.5
0.4
0.3
0.2
0.1
0
40
60
80
100
Temperature (K)

FIGURE IV-6

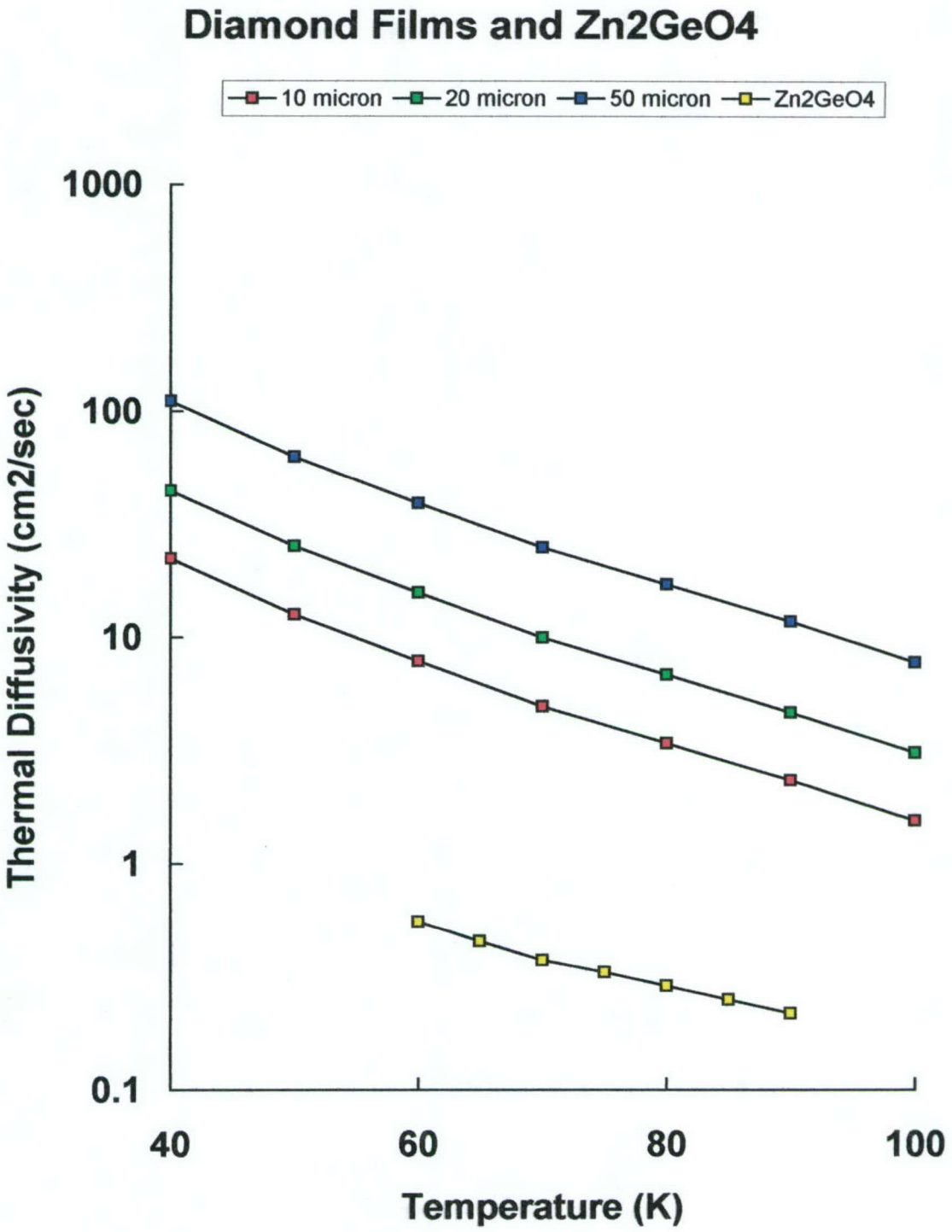
Diamond Films and Zn2GeO4
10 micron
20 micron
50 micron
Zn2GeO4
1000
100
10
1
0.1
Thermal Diffusivity (cm2/sec)
40
60
80
100
Temperature (K)

FIGURE IV-7

V. ASSESSMENT OF CRYOVARISTOR FOR QUENCH PROTECTION

A. INTRODUCTION AND BACKGROUND

Varistor ceramics based on ZnO have found a wide variety of room-temperature applications based on their highly nonlinear I-V characteristics [1-4]. As illustrated in Fig. V-1, at an electric field E ~ 1 kV/cm the material changes from an insulator to a very good conductor, and this switching is useful for the protection of sensitive equipment from transient over voltages. This region is referred to as the breakdown region, and the

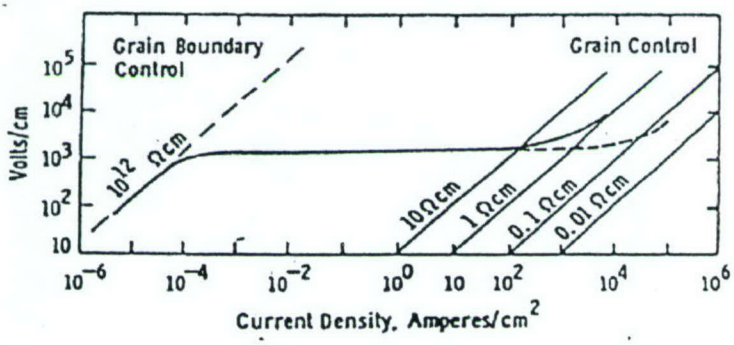

Figure V-1. *Illustration of the characteristics of a varistor. There is an insulation region at low small electric fields (voltages) followed by a breakdown region where the material becomes very conducting over several orders of magnitude in current density. Finally, at large current densities there is an upturn region where the electric field increases rapidly with current density.*

electrical characteristics of the varistor can be thought of as back-to-back Zener diodes [5,6]. In the breakdown region the current density J increases by up to six orders of magnitude before reaching the so-called upturn region where the field increases rapidly. These three features are illustrated in Fig. V-1.

The pre-breakdown insulating region is due to high-resistivity grain boundaries, and the upturn region is due to conduction through the ZnO grains. Varistor ceramics are formed by sintering ZnO and other additives such as the oxides of Bi, Sb, Co, Mn, Ni, Cr, Si, Al, etc. and these additives concentrate in the grain boundaries and provide the electrical barriers necessary to impart the varistor characteristic [7]. To use the varistor in a thin film, the film thickness should be at least double the grain size in order to incorporate the necessary grain boundaries. The grain size of a varistor ceramic is typically about 5 micron.

The elementary picture of the varistor is that of semiconducting n-type ZnO grains separated by grain boundaries of high resistivity, and estimates of the room-temperature resistivities of the ZnO grains and grain boundaries are typically 1-10 Ω cm and 10^{12} Ω cm, respectively. It has also been observed [4,5] that the breakdown field (~ 1 kV/cm) is

independent of the carrier concentration in the ZnO grains and is also quite insensitive to the nature and amount of the various oxide additives or to the ceramic processing.

A number of theoretical papers have been published on the ZnO varistor and are reviewed in Refs. 5 and 6. These theoretical approaches deal with four phenomena: (1) Avalanche breakdown; (2) Space-charge-limited currents; (3) Double Schottky barrier; and (4) Fowler-Nordheim tunneling. These models are an extension of the single crystal band model to a polycrystalline ceramic and can explain certain aspects of the varistor characteristics. The random, composite nature of the varistor has not yet been adequately addressed, but a statistical approach [8] has shown that the effect of having many grains could increase the strength of the non linearity.

Common to all theoretical approaches thus far has been the assumption of a *thermally-activated* grain-boundary conduction in the pre-breakdown region [i.e., $\sigma \propto \exp(-Q/kT)$] as supported by previous experimental data [6]. However, as we shall presently see, the *cryovaristor* characteristic derives primarily from a *non-thermally-activated* grain boundary conduction.

The cryovaristor characteristic follows from the discovery at CeramPhysics that a proprietary ZnO-based ceramic [9] retains the highly nonlinear current-voltage property essentially *unchanged* from room temperature down to 4.2 K -- hence the name cryovaristor. This unique cryovaristor property is illustrated in Fig. V-2, contrasted with the thermally-activated pre-breakdown region of conventional varistors [6].

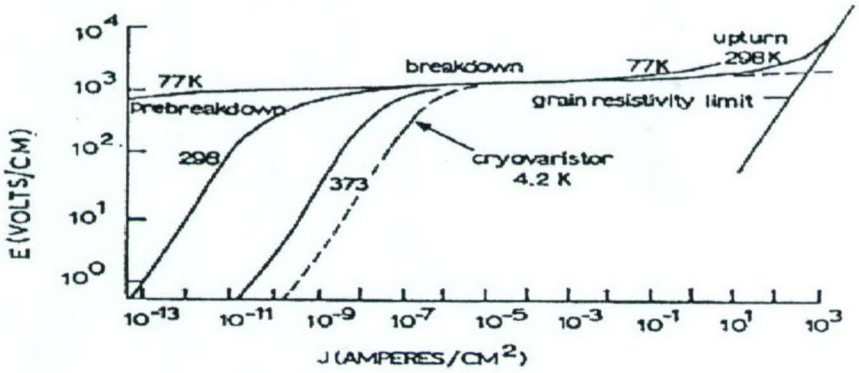

Figure V-2. *The cryovaristor characteristic (dashed lines) compared with the characteristics of conventional varistors. The cryovaristor retains the highly nonlinear characteristic down to 4.2 K whereas conventional varistors progressively lose this property at temperatures below room temperature.*

The cryovaristor might provide *quench protection* for HTS magnets operating near 77 K by shunting the current out of a normal-zone region, and this mechanism might significantly simplify the refrigeration requirements for these magnets. The purpose of this study is to review the measured properties of the cryovaristor and to provide an assessment of this unique cryovaristor approach for HTS quench protection.

B. REVIEW OF THE MEASURED PROPERTIES OF THE CRYOVARISTOR

Thermal Properties

The thermal conductivity of the cryovaristor was measured on a ceramic bar by the two-heater, one-thermometer method, and measured data in the range 60 - 90 K are shown in Fig. V-3(a). The thermal conductivity is large and has a maximum of 0.6 W cm^{-1} K^{-1} near 90 K (Data over a larger temperature range clearly show the maximum). In the range 60 - 90 K the thermal conductivity is essentially temperature independent.

The specific heat of the cryovaristor was measured on a ceramic pellet by a combined drift + pulse method, and data in the 60 - 100 K range are shown in Fig. V-3(b).

These thermal conductivity data and specific heat data were given in table form in Section III for modeling purposes, and thermal diffusivity data were also tabulated.

Thermal conductivity data below 30 K (not shown) were analyzed according to the dominant-phonon approximation that was discussed in Section IV. It was found that the low-temperature boundary scattering limit corresponds to a ceramic grain size of 5 microns [10]. This reinforces the observation made above regarding the minimum thickness of a thin film of the cryovaristor.

Specific heat data below 30 K were measured on pure ZnO and on the cryovaristor, and some interesting physics effects were found [10]. The grain boundaries in the cryovaristor dominate the specific heat below 30 K due to two Schottky terms arising from *compensating* charge densities at the grain boundaries. Therefore, the thermal properties can be understood very well based on the model of the cryovaristor given above.

Thermal expansion data were measured on a ceramic bar of the cryovaristor from 4.2 to 298 K by a capacitance-dilatometry method. These data together with data for copper, nickel, and YBCO are shown in Fig. V-4. Copper and YBCO have identical thermal expansions below room temperature whereas nickel and the cryovaristor have smaller thermal expansions. The thermal expansion of the cryovaristor is well matched to that of nickel.

Electrical Properties

Pulse measurements were made on a cryovaristor sample because large currents could be used for short pulse times to avoid overheating the sample. A Tektronix curve tracer with a camera was used, and the sample was immersed in liquid nitrogen and liquid helium, in addition to the room temperature measurement. The curve traces obtained at 298, 77, and 4.2 K are shown in Fig. V-5, and two traces are shown at 4.2 K, one in zero magnetic field and the other at 10 T (The helium-temperature measurements were made at the National Magnet Lab. at MIT). The axes in Fig. V-5 are reversed compared to case shown in Fig. V-2 (i.e., in Fig. V-5 the vertical axis is current, the horizontal axis, voltage), and the scales in the four traces are the same (50 V per div. horizontal and 200 μA vertical). The curves in Fig. V-5 are essentially identical.

The breakdown region for varistors is commonly characterized by the nonlinear coefficient

$$\alpha = d\ln I / d\ln V \qquad \text{(V-1)}$$

which can be found directly from the curve traces. In Fig. V-6 are shown data for this coefficient at 4.2 K as a function of magnetic field. Also shown in Fig. V-6 at zero field are the values of the coefficient at 77 and 298 K.

The Fig. V-6 data show that the α coefficient is only weakly dependent on magnetic field at 4.2 K, and any magnetic-field effects will be *largest* at 4.2 K because electron mean free paths are longest at these low temperatures. Consequently, in the operating temperature range of HTS magnets, the effect of a magnetic field on the cryovaristor can be confidently ignored.

C. CRYOVARISTOR ELECTRICAL AND THERMAL MODELS

Electrical Model

To lay the groundwork for the electrical model we first review the structure of the HTS ribbon which consists of the following materials and their dimensions (in microns): YBCO (1-2) coated with CeO_2 (0.3-1.0) deposited on a Ni substrate (50-100), and a Ag overlayer (3-4) and a Cu overlayer (20-80) are atop the YBCO. A good design number for the current is 100 A per cm of width of the ribbon [11]. We will assume a 1-cm wide ribbon carrying 100 A for modeling purposes.

To introduce the model, it is instructive to first examine the case where a cryovaristor film deposited on the Cu overlayer is *not* in contact with any adjacent winding. Let x measure the distance along the Cu overlayer and let $x = 0$ be that point where the YBCO first becomes resistive and the current flows into the Cu overlayer. Then the voltage across the current-carrying overlayer at $x > 0$ is given by

$$V = I \rho x / t \qquad \text{(V-2)}$$

where I is the current (100 A), ρ is the resistivity of Cu, and t is the thickness of the Cu overlayer (Recall that we adopt a 1-cm wide ribbon).

From Fig. V-2 the cryovaristor breakdown occurs at an electric field of about 1 kV/cm, and $E = V/x$ is the *longitudinal* field strength in the cryovaristor film arising from the current flowing in the Cu overlayer. Consequently, from Eq. (V-2),

$$E = I \rho / t \qquad \text{(V-3)}$$

which is *independent* of x. Using the resistivity of pure Cu at 67 K, $0.16 \times 10^{-6}\ \Omega$ cm, and I = 100 A and t = 80 micron, we find from Eq. (V-3) that $E \sim 2$ mV. And for Cu at 20 °C, $E \sim 21$ mV. Therefore, an isolated cryovaristor film will offer *no* quench

protection because the longitudinal electric field strength in the film is always very small compared to the breakdown field and no longitudinal current will flow in the cryovaristor film.

Next we consider a more feasible case where the cryovaristor film on the Cu overlayer is *also* in electrical contact with the adjacent winding (via a Cu overlayer on the latter) to provide a ground plane. In this case the current flowing in the overlayer will eventually build a *transverse* electric field across the film equal to the breakdown field and then the film will become conductive. If the film thickness is d, the transverse field across the film due to the current in the overlayer is, using Eq. (V-2),

$$E = I \rho x / t d \qquad \text{(V-4)}$$

We define x = L as the point where the breakdown condition, E = 1 kV/cm, is satisfied in Eq. (V-4).

To judge the practicality of this case, we solve for x = L in Eq. (V-4) and find

$$L = 0.10\, t\, d / \rho \qquad \text{(V-5)}$$

where L is in cm, t and d are in microns, ρ is in micro-ohm cm, and I = 100A.

A plot of L vs. the product td is shown in Fig. V-7 and the curves are parameterized in the resistivity of the Cu overlayer. The range of td is based on minimum values of t and d of 20 and 10 microns and maximum values of 80 and 30 microns, respectively. The resistivity values for pure Cu in Fig. V-7, 0.16, 0.80, and 1.60 correspond to temperatures of 67, 160, and 273 K, respectively.

The data in Fig. V-7 provide important insights into how this cryovaristor quench-protection mechanism might operate, or be engineered to operate. In the simplest case, if the normal zone in the YBCO is localized to x < L, then in the absence of heating effects the current will "flow around" the normal zone through the Cu overlayer and re-enter the YBCO -- in this case the Cu overlayer provides the quench protection for which it was intended.

In the more likely case, the Joule heating in the Cu overlayer causes the underlying YBCO to become normal, and this normal zone propagates a distance x = L to where the cryovaristor film becomes conductive and draws the current out of the Cu overlayer and into the adjacent winding. This mechanism provides quench protection by limiting the extent of the normal-zone propagation. The data in Fig. V-7 indicate that as the temperature of the overlayer increases, the distance L rapidly decreases.

The Fig. V-7 data show that practical lengths L are only associated with *small* td values and *large* Cu resistivity values. There may be an advantage to increasing the resistivity of the Cu overlayer by adding impurities in order to decrease L (e.g., at td = 200 and ρ = 4.0, L = 5 cm). In this case, of course, the Joule heating in the overlayer will be much larger but over a shorter distance, and this may be a reasonable tradeoff.

This cryovaristor protection mechanism *sacrifices* approximately one circumference of a winding -- i.e., from the point where x = L to the neighboring point on the adjacent winding -- and no current flows in this sacrificial winding.

Finally, the current distribution in the neighborhood of the conducting cryovaristor film is a formidable thermal/electrical problem involving the Cu overlayer, the cryovaristor film, and the Cu overlayer + Ni substrate + YBCO layer in the adjacent winding. This problem, which is beyond the scope of the study here, can be outlined as follows: As the cryovaristor film enters the breakdown region there will be some leakage current through the film into the Cu overlayer on the adjacent winding, and this current will increase rapidly as the electric field incrementally increases (Fig. V-2). The current is shared with the Cu overlayer + Ni substrate + YBCO in the adjacent winding, and for this mechanism to operate the electric field has to remain across the cryovaristor film (otherwise the film once again becomes insulating).

We can make a crude estimate of the length of the cryovaristor film involved in shunting current between the windings, as follows. Substituting Eq. (V-2) into Eq. (V-1) for the breakdown region, we have

$$d\ln I = \alpha \, d\ln x \qquad \text{(V-6)}$$

where, as before, x measures the length along the winding from the point where the current first flows into the Cu overlayer. If a leakage current I_1 flows across the film at x_1, and if the full current I_2 flows across the film at x_2, then Eq. (V-6) integrates to

$$\ln(I_2/I_1) = \alpha \ln(x_2/x_1) \qquad \text{(V-7)}$$

If we select I_1 = 10 A and I_2 = 100 A, then using $\alpha = 20$ from Fig. V-6 we have x_2/x_1 = 1.12. Thus, if x_1 = 100 cm, x_2 = 112 cm, and the length of the film involved is about 12 cm.

Another electrical model for quench protection would involve the cryovaristor in the form of a multilayer ceramic capacitor (MLC) located external to the HTS magnet (quench protection of A15 superconducting magnets at 4.2 K are often protected by connecting windings to externally located diodes). Varistor MLC's have been made in the laboratory [12] and are commercially available [13], and in this protection scenario, leads would run from locations on the coil to the MLC cryovaristors. However, such leads would have to carry 100 A and would have impractically large diameters. Therefore, this MLC cryovaristor approach is not viable.

Thermal Model

The goal here is to estimate the temperature rise in the cryovaristor film in that region where the 100 A current is being shunted to the adjacent winding across this film.

The heat-flow equation for this case is

$$C\partial T/\partial t = \partial/\partial z\,(K\partial T/\partial z) + EJ \qquad \text{(V-8)}$$

where C is the volumetric specific heat, K is the thermal conductivity, E is the breakdown field, and J is the current density flowing across the film. The variable z measures the distance across the film from z = 0 to z = d, where as before d is the film thickness. The current distribution in the film is ignored -- the length of the film in the breakdown region is assumed to carry the current density J.

The solution to Eq. (8) always consists of a steady-state term plus a transient term, and the latter term decays in time with a time constant given by

$$\tau = d^2/4\pi^2\,k \qquad \text{(V-9)}$$

where k is the thermal diffusivity. For the cryovaristor $k \sim 0.7\ cm^2/sec$, and for $d \sim 20$ micron we find for the time constant about 0.15 microseconds. This seems much faster than any other time scales involved, and we shall therefore ignore the transient term and consider only the steady-state case described by

$$\partial^2\theta/\partial z^2 + EJ/K = 0 \qquad \text{(V-10)}$$

where a variable change has been made, $\theta\,(z) = T - T'$. We assume that both sides of the film are at the same temperature T' so that $\theta\,(z)$ is the temperature distribution across the film.

The boundary conditions are $\theta\,(0) = \theta\,(d) = 0$, and the solution is the Fourier series,

$$\theta(z) = \Sigma\, A_n \sin\,(n\pi z/d) \qquad \text{(V-11)}$$

The Fourier coefficients are determined in the usual fashion [14], and we find for the centerline temperature at z = d/2,

$$\theta(d/2) = (EJ/K)(2d^2/\pi^3)\,\Sigma\,[1-(-1)^n]\sin\,(n\pi/2)/n^3 \qquad \text{(V-12)}$$

The series in Eq. (V-12) converges rapidly because of the $1/n^3$ term and is easily evaluated from the first five non-zero terms to yield 1.93. Finally, we have for the centerline temperature

$$\theta(d/2) = 2.09 \times 10^2\, d^2\, J \qquad \text{(V-13)}$$

where $K = 0.6\ W\ cm^{-1}\ K^{-1}$ from Fig. V-3, E = 1 kV/cm, and the current density J is in A/cm^2. Data calculated from Eq. (V-13) are given in Table V-I.

Table V-I

Centerline Temperature of the Cryovaristor Film (mK)

d, micron	J = 10 A/cm^2	J = 20 A/cm^2
10	2.1	4.2
20	8.3	16.7
30	18.8	37.5
40	33.4	66.7

The current density J = 10 A/cm^2 approximately corresponds to the 100 A flowing across the 12 cm length of conducting film estimated above.

The data in Table V-I show that the centerline temperature rise of the film is relatively modest, < 70 mK in the worst case. The reason for this is the film is thin and has a large thermal conductivity. A more sophisticated model taking into account the transient term, allowing for different temperatures at z = 0 and z = d, and taking into account the current distribution across the length of the film would not change this conclusion that the centerline temperature rise is small.

D. DISCUSSION AND CONCLUSIONS

The background of the cryovaristor has been presented, and thermal and electrical data measured on the cryovaristor at low temperatures have been reviewed, including data measured in intense magnetic fields.

A cryovaristor film applied to the Cu overlayer of the HTS ribbon appears feasible for quench protection. There are two key elements to this method: First, the current flowing through the Cu overlayer downstream of that point where the YBCO first becomes resistive must travel a critical distance in order to build the necessary *breakdown* electric field for the cryovaristor film to become conducting; and second, the film has to be in electrical contact with another Cu overlayer on an *adjacent* winding to provide a ground plane. This quench-protection mechanism sacrifices one complete turn of the HTS winding.

An electrical model of this quench-protection mechanism is presented, and numerical estimates of the critical length of the Cu overlayer appear practical under realizable conditions.

A thermal model of the cryovaristor film (60 - 90 K) in the breakdown region is Fourier-analyzed, and it is found that the temperature rise of the centerline of the film is modest, < 70 mK. This is due to the large thermal conductivity of the cryovaristor.

There are two outstanding problems to be addressed for this cryovaristor-based quench-protection mechanism:

1. An analysis of the current-sharing conditions associated with the cryovaristor film in the breakdown region has to be performed. This is a challenging thermal/electrical problem involving the temperature rise in the Cu overlayer carrying 100 A, the nonlinear current distribution across the cryovaristor film, and the current sharing

between the Cu overlayer, the film, and the Cu overlayer + Ni substrate + YBCO layer in the adjacent winding.

2. It has to be experimentally demonstrated that the cryovaristor ceramic composition with appropriate grain boundaries can be deposited on the Cu overlayer of an HTS ribbon (by sputtering, MOCVD, etc.) and that such a film does have the cryovaristor characteristics at low temperatures. The film may require a heat treatment to develop the proper characteristics [12] but the temperature of such a treatment is limited to 400 °C.

References

1. L. M. Levinson and H. R. Phillipp, *Ceramic Bulletin* **65** (4), 639 (1986).
2. R. G. Dosch, B. A. Tuttle, and R. A. Brooks, *J. Mat. Res.* **1**, 90 (1986).
3. M. Prudenziati, A. Masoero, and A. M. Bietto, *J. Appl. Phys.* **58**, 345 (1985).
4. G. D. Mahan, L. M. Levinson, and H. R. Phillip, *J. Appl. Phys.* **50**, 2799 (1979).
5. L. M. Levinson and H. R. Phillip, *J. Appl. Phys.* **46**, 1332 (1975).
6. H. R. Phillip and L. M. Levinson, *J. Appl. Phys.* **48,** 1621 (1977).
7. T. K. Gupta and W. G. Carlson, *J. Appl. Phys.* **53**, 7401 (1982); W. G. Carlson and T. K. Gupta, *J. Appl. Phys.* **53**, 5746 (1982); T. K. Gupta, W. G. Carlson, and P. L. Hower, *J. Appl. Phys.* **52**, 4104 (1981).
8. P. R. Emtage, *J. Appl. Phys.* **50**, 6833 (1979).
9. W. N. Lawless and T. K. Gupta (unpublished).
10. W. N. Lawless and T. K. Gupta, *J. Appl. Phys.* **60**, 607 (1986).
11. C. E. Oberly (private communication)
12. T. K. Gupta (private communication)
13. Vitramon Corp.
14. R. V. Churchill, *Fourier Series and Boundary Value Problems* (McGraw Hill, New York, 1941).

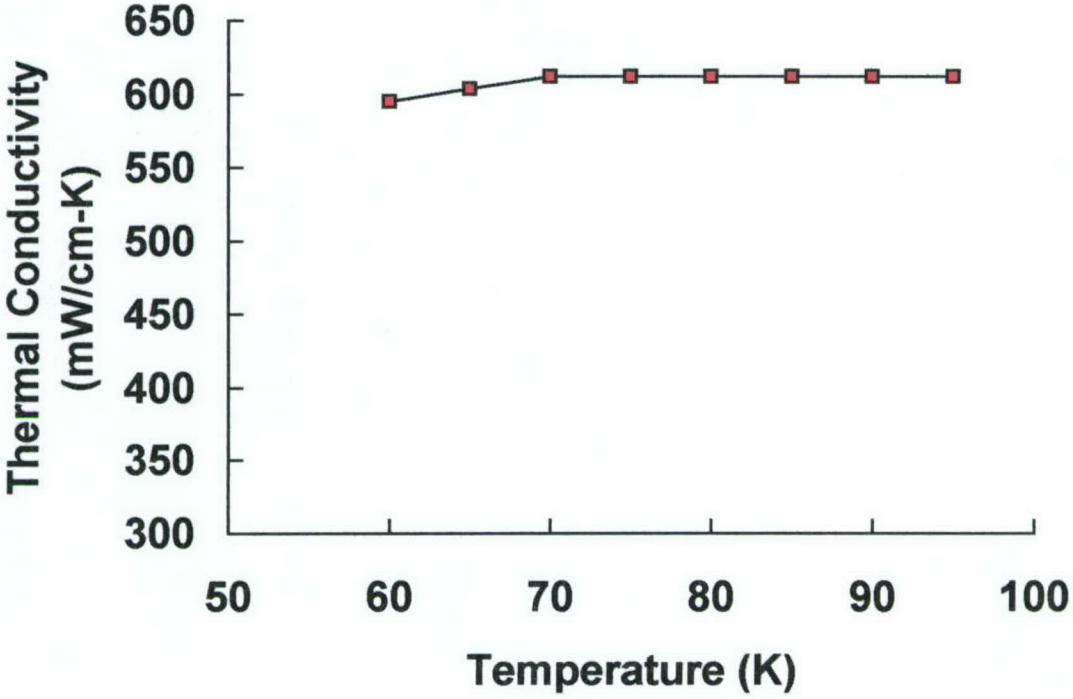
Thermal Conductivity (mW/cm-K)
650
600
550
500
450
400
350
300
50
60
70
80
90
100
Temperature (K)

(a)

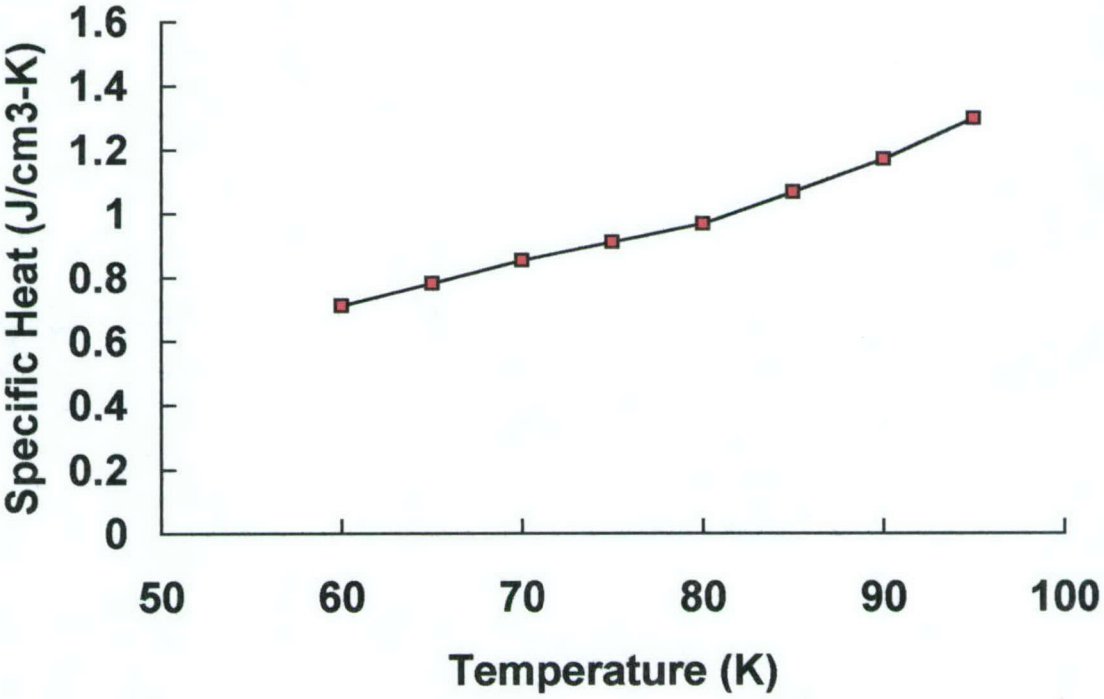
Specific Heat (J/cm3-K)
1.6
1.4
1.2
1
0.8
0.6
0.4
0.2
0
50
60
70
80
90
100
Temperature (K)

(b)

FIGURE V-3

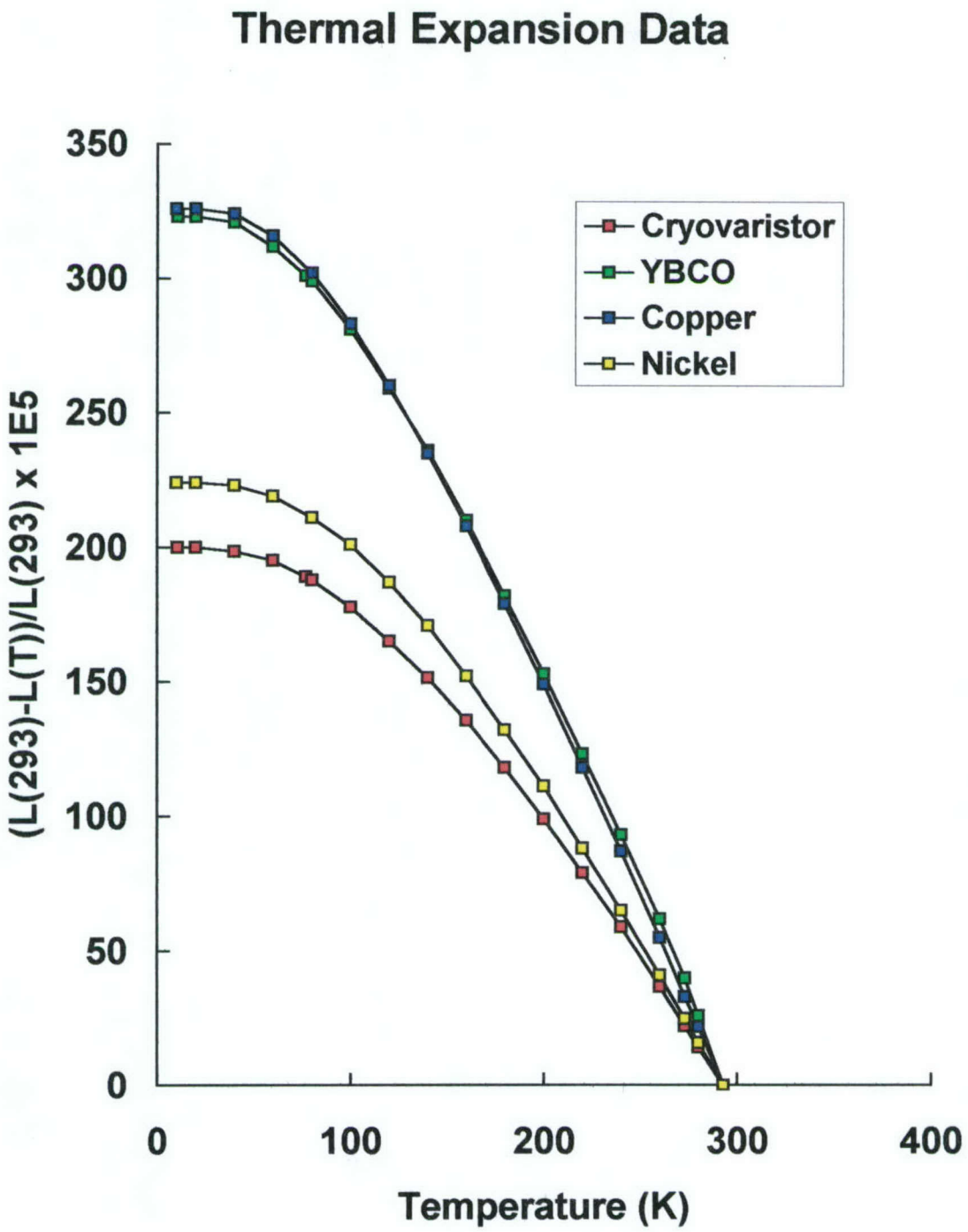
Thermal Expansion Data
350
300
250
200
150
100
50
0
(L(293)-L(T))/L(293) x 1E5
0
100
200
300
400
Temperature (K)
Cryovaristor
YBCO
Copper
Nickel

FIGURE V-4

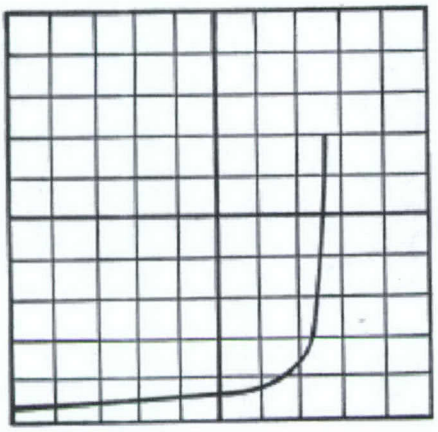

298 K

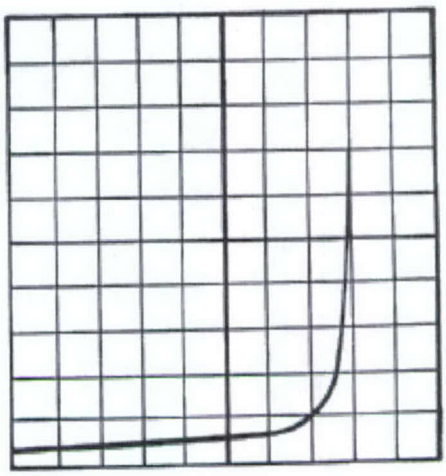

77 K

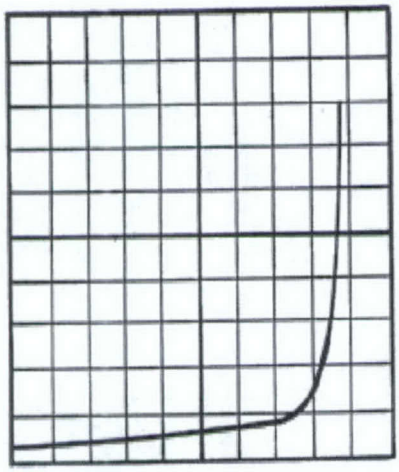

4.2 K, H = 0

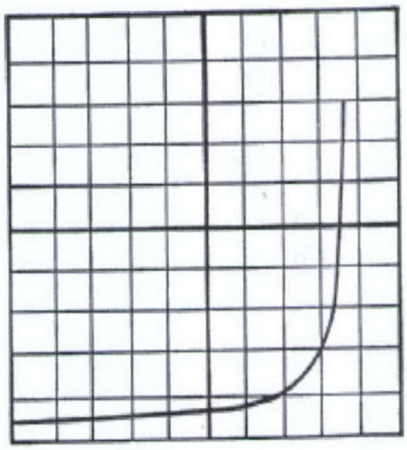

4.2 K, H = 10 T

FIGURE V-5

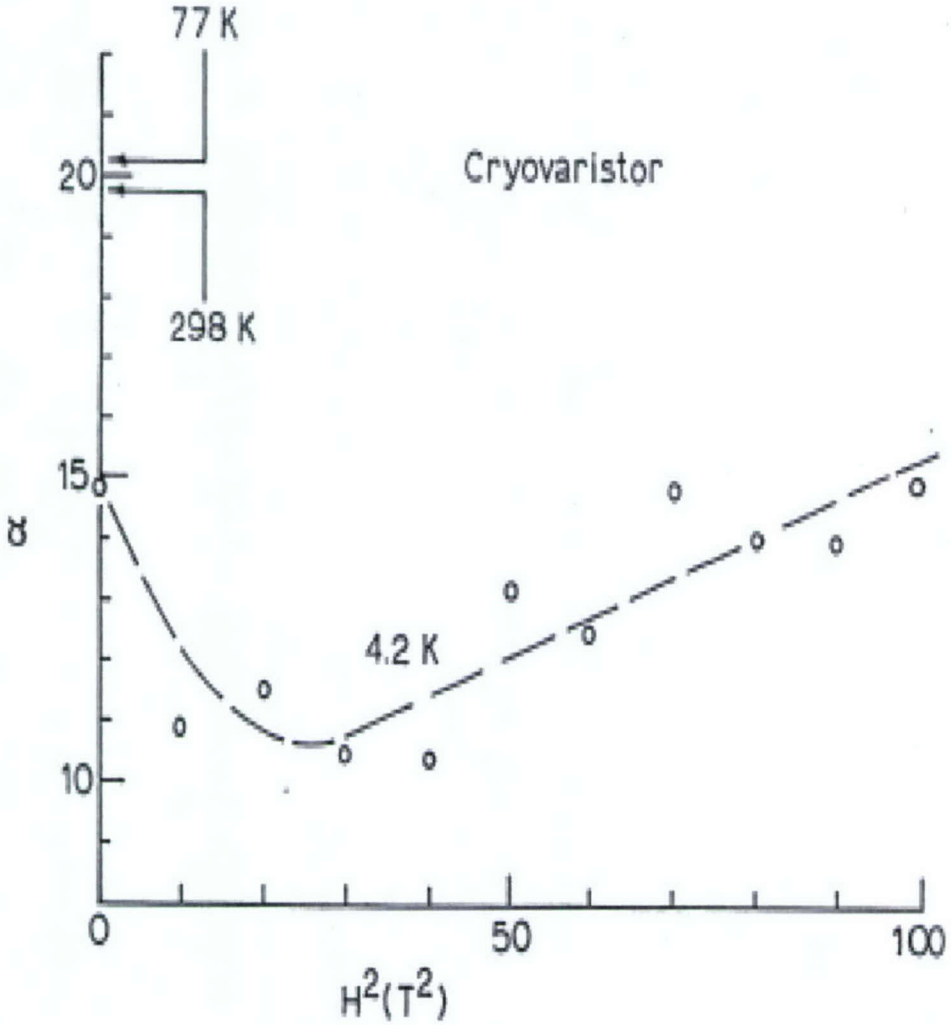

FIGURE V-6

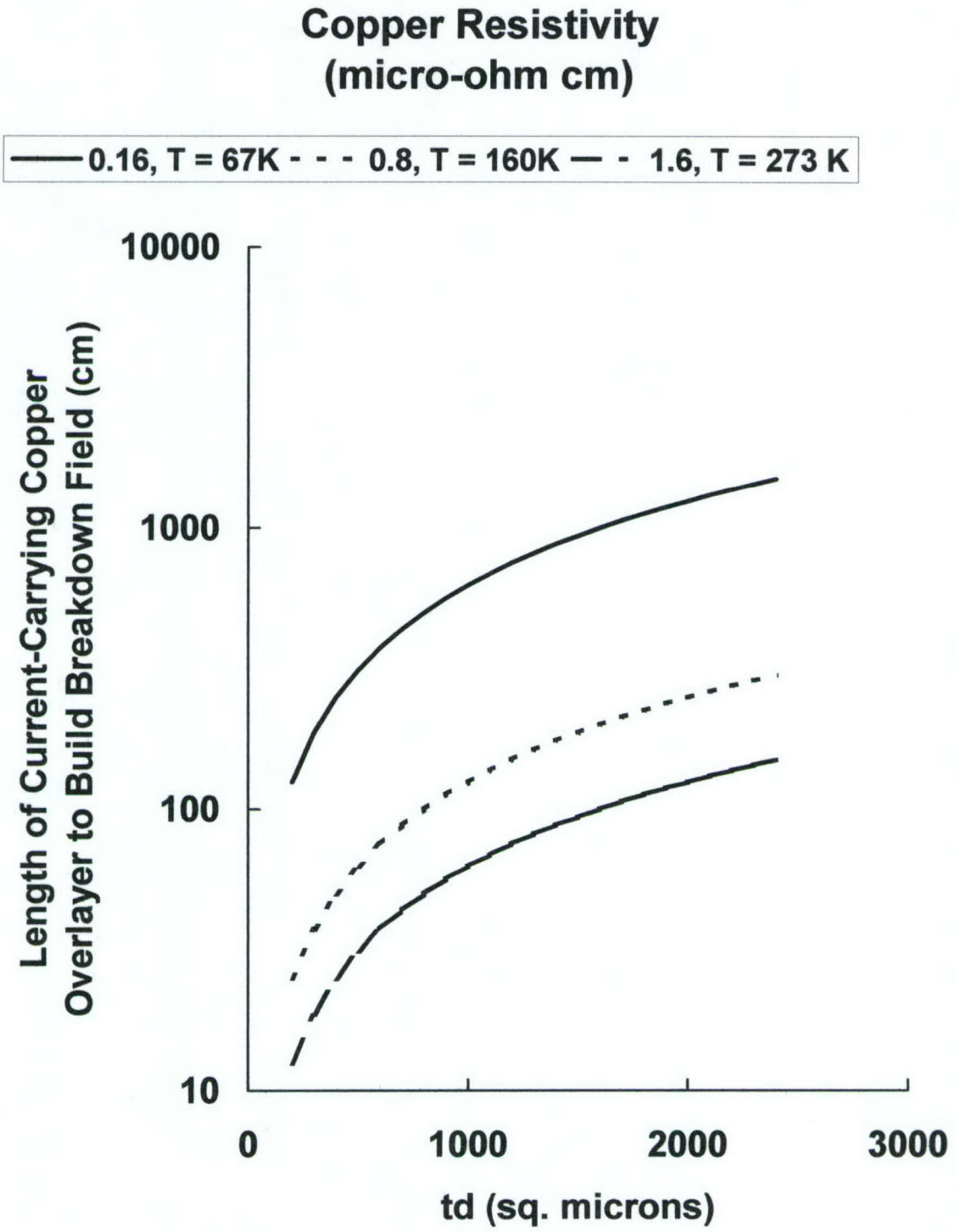
Copper Resistivity
(micro-ohm cm)
0.16, T = 67K
0.8, T = 160K
1.6, T = 273 K
10000
1000
100
10
Length of Current-Carrying Copper
Overlayer to Build Breakdown Field (cm)
0
1000
2000
3000
td (sq. microns)

FIGURE V-7

VI. FORMVAR VARNISH LOADED WITH CERAMIC POWDERS

A. SAMPLE PREPARATION AND MEASUREMENT METHODS

a. Sample Preparation

In the previous program in this technology (Phase I, SBIR, F33615-99-C-2969), 10-micron powders of five different ceramic compositions were loaded in the GE 7031-varnish type of Formvar at both the 40 and 60 vol.% levels, where vol.% refers to the *cured* varnish. The problem in preparing these samples was to avoid entrapped air bubbles, and for this purpose the viscosity of the 7031 varnish was measured,

$$\eta = 15.87 \exp(0.0683x), \text{ poise} \qquad \text{(VI-1)}$$

where x is the volume percent of the methanol/toluene solvent in the as-received varnish. It was found empirically that a mixture with x = 36.7% produced samples without bubble formation.

The samples in the previous program were cast by dip-coating in long (~ 5 cm) Al molds attached to wooden dowels and immediately inserted into a rotating wheel (1 rpm) to keep the samples horizontal during drying to avoid settling of the ceramic grains. A 2-hour air-drying time between dip coats was adequate, and after five dips the mold was baked at 125 °C for two hours to cure the varnish (more than five dips often resulted in bubble formation on curing). The procedure was repeated until the thickness of a cast sample reached about 3 - 4 mm, after which the thin Al mold was pealed off the sample. Final shaping of the bar was done with sandpaper to provide plane-parallel surfaces for measurements.

As mentioned in Section III above, the NN ceramic composition was chosen for this Phase I STTR program.

For the HTS conductor in the present program, 10-micron ceramic powders are too large because the insulation is expected to be 10-micron thick, or less, and therefore it is necessary to study the properties of much finer NN powders loaded in the varnish. Discussions with California Fine Wire Co. led to the choice of 1 - 2 micron sized ceramic grains as being compatible with CFW's draw-tower facilities for potentially coating an HTS conductor (CFW has had experience in applying coatings at high ceramic-powder loadings).

Fine ceramic powders of the NN ceramic composition were prepared by NexTech Materials, Ltd., and in Fig. VI-1 is shown an x-ray diffraction pattern of this powder which confirms the correct phase formation. The particle-size distribution of the powder is shown in Fig. VI-2, and it is seen that the distribution is centered at 1.5 micron.

Loadings of the fine NN powders in the varnish at the 50 and 60 vol.% levels were selected for study. Varnish/solvent solutions with x = 36.7% (see above) were prepared, but it was found that dip-coated samples contained bubbles due to the different rheology conditions with the much finer powders. After much trial and error, it was found that

solutions with x = 40.0 and 35.0 % gave the best results for the 50 and 60 vol.% loading levels, respectively.

Bars were prepared as described above and from density measurements the porosity levels were 25.3 and 23.2 vol.% porosity for the 50 and 60 vol.% levels, respectively (the measured thermal conductivity data below will be corrected for porosity). SEM's of the 50 and 60 vol.% bars are shown in Figs. VI-3 and VI-4, respectively.

b. Measurement Methods

Thermal conductivity measurements, 60 - 90 K, were made by the two-heater, one-thermometer method in a high vacuum. The advantage of this method is that only one thermometer calibration is involved; the disadvantage is that the two heaters should be evenly matched in resistance. If the two heaters are separated by a distance L, and if ΔT is the temperature difference measured by a thermometer on the free end of the bar when the heaters are separately actuated by the same heating power, then the thermal conductivity, K, is determined from

$$i^2R = K(A/L)\,\Delta T \qquad \text{(VI-2)}$$

where i^2R is the heating power and A is the cross-sectional area of the bar [Eq. (VI-2) applies only if the two heaters have the same resistance R and are powered by the same current i].

The heaters were wrapped on the bars using 93 Ω/ft, pre-measured manganin wires of the same length, and fine adjustments of the resistances were made later by adjusting the lengths of the hookup leads in the cryostat. The heater resistances were about 150 Ω and were matched to about +/- 0.8%. The thermometer was a ground 1 kΩ Allen Bradley carbon resistor, and all attachments to the bars were made with GE 7031 varnish.

The cryostat was placed in a dewar, and the surrounding liquid nitrogen bath was pumped to obtain temperatures below 77 K. A datum was measured as follows: The adiabatic shield/reservoir was temperature controlled at a desired set point, and the sample thermometer was calibrated *in situ* (at each set point). The heaters were then separately activated and when thermal equilibria were established, the thermometer readings were recorded. The $\Delta T/T$ values were maintained in the 3 - 5% range, and the K-values at each set point were determined from Eq. (VI-2). The thermal conductivity is proportional to RL/A, and the uncertainty in this quantity was less than 5%. The measurement of the heater current i had a negligible uncertainty, and the uncertainty in determining ΔT is about +/- 2%. Therefore, the overall uncertainty in the measured thermal conductivity is no larger than +/- 5.5%.

The thermal conductivity data have to be corrected for the porosity in the samples, and this correction factor has been examined in depth by Zaitlin and Anderson [1]. At

temperatures above 10 K heat is transported by high-frequency phonons for which diffraction is negligible, and a "missing volume" correction factor applies,

$$f = \exp(2.236x) \qquad \text{(VI-3)}$$

where x is the volume faction of the pores. The measured thermal conductivity from Eq. (VI-2) is multiplied by f, and this correction is valid for $x < 50\%$.

Following the thermal conductivity measurements, the bars were cut on a diamond saw to have squared-off, parallel ends. The thermal expansion measurements, 60 - 300 K, were made by a capacitance dilatometer method. The test bar was mounted vertically in a copper fixture with super glue and GE 7031 varnish, and a thin metal plate was similarly mounted on the top of the bar. This plate formed one plate of a parallel-plate capacitor, the other plate being the insulated top plate of the fixture. All parts of the fixture were made with OFHC copper, and the thermal expansion of the test bar is therefore determined relative to the well-known thermal expansion of copper. The measurements were made in a temperature controlled cryostat immersed in liquid nitrogen using a General Radio Capacitance Measurement Assembly Model 1615A. High vacuum conditions are maintained, and the dielectric constant of the space between the parallel plates is taken to be unity. The capacitance is inversely proportional to the separation of the plates, and changes in capacitance are related to the relative changes in the length of the test bar with temperature. The largest source of error in the method is the measurement of the length of the bar (< +/- 0.5%).

Porosity in the test bar does not affect the thermal expansion measurement by the following argument: The Young's modulus of the solid material in the bar is much larger than that of the gas in the pores, and therefore the strain of the solid material due to the pores is negligible. This argument is reinforced if the porosity is connected (as the SEM's in Figs.VI-3 and VI-4 suggest) since then there is no gas in the pores under high vacuum conditions.

B. MEASUREMENT RESULTS

Thermal conductivity data, corrected for porosity according to Eq. (VI-3), are shown in Fig. VI-5 in the range 65 - 95 K for 50 and 60 vol% of 1.5-micron NN powders in GE 7031 varnish. The 60 % loading has the higher thermal conductivity, and the ratio of the two data sets is about 0.85 which agrees well with the ratio of the two powder loadings, 50/60 = 0.83. This is good internal consistency for the measurement methods and the porosity correction.

Thermal conductivity data for these 1.5 micron powders compared to the former 10 micron powders, both at the 60 % NN level, are shown in Fig. VI-6, and at 77 K the thermal conductivity of the former, 17, is about 77% of that of the latter, 22 (all thermal conductivities here are in the units of mW/cm-K). These data contain some interesting information on the physics of heat transport, as follows. First, the thermal conductivity of the 60% composite with 10-micron powders *uncorrected* for porosity is 13 at 77 K,

and for ceramic NN with a 5-micron grain size, 102 at 77 K (Fig. III-5, Section III). If we ignore the differences in grain sizes and assume that the GE7031 content in the composite can be treated as porosity (owing to its small thermal conductivity at 77 K, 2.3), then the total "porosity" would be 53.9 % and f = 3.34 from Eq. (VI-3) -- one would then expect the composite to have an uncorrected thermal conductivity of 102/3.34 = 30.6 at 77 K instead of 13. The explanation for this large disparity is *Kapitsa thermal resistance* at the interfaces between the ceramic powders and the varnish. This interfacial thermal resistance is analogous to the refraction of light passing between two materials of different indices of refraction (i.e., longer path length) and increases with surface area. This explains why the 1.5-micron powder composite in Fig. VI-6 with the larger surface area has a smaller thermal conductivity that the 10-micron powder composite. Of course, the boundary-scattering limitations discussed in Section IV play a role here also.

Therefore, the GE7031 varnish wets the surfaces of the NN powders and causes a large Kapitsa resistance at the interfaces which is the *dominant* limitation in the thermal conductivity of these composites. The good scaling between the 50 and 60% data sets indicates that the Kapitsa effects are essentially equivalent in the two composites.

Thermal diffusivity data for the 50 and 60 % NN loadings of the 1.5 micron powders are shown in Fig. VI-7, and comparison diffusivity data for the 1.5 and 10 micron powders are shown in Fig. VI-8. To construct these plots, the additive law of specific heats was used (for non interacting materials) from the known specific heats of NN and GE 7031.

Finally, thermal expansion data were measured on the 60% composite bar with 1.5-micron NN powders in the range 60 - 300 K and are shown in Fig. VI-9 compared to previous data for the 10-micron powder case (The 50% bar with 1.5-micron powders was damaged in cleaning and could not be measured). The two data sets in Fig. VI-9 agree reasonably well, but it is unclear why the 1.5-micron case has the smaller thermal expansion since considerations of grain size and porosity do not enter the data analysis, as discussed above.

References

1. B. Zaitlin and A. C. Anderson, *Phys. Rev.* **B12**, 4475 (1975).

C. DISCUSSION AND CONCLUSION

The original SBIR program involved 10-micron size ceramic powders loaded in GE 7031 varnish, but this leads to an insulation too thick for the current HTS tape. Therefore, 1.5-micron size powders were prepared from an NN ceramic selected in Section III based on discussions with California Fine Wire regarding compatibility with a 10-micon thick insulation. Composite bars with 50 and 60 vol.% ceramic powders were successfully cast and measured.

Although the thermal conductivities of these composites contain some interesting physics of heat transport, the dominant limitation in the thermal conductivity is Kapitsa boundary resistance between the ceramic powders and the GE 7031 varnish which leads

to greatly reduced thermal conductivities. As discussed in Section VIII, these thermal conductivities are too small to provide much quench protection for HTS coils. Therefore, this dielectric-insulation approach for quench- protection is not a favorable approach at this time.

However, this loaded-Formvar approach is the *ultimate backup strategy* for a dielectric insulation for the following reasons: (1) Very fine, 1.5-micron size ceramic powders of NN can be prepared inexpensively and are compatible with GE 7031 varnish; (2) A 10-micron composite insulation can be applied inexpensively to the HTS tape using existing, commercial, room-temperature facilities; and (3) A thermal conductivity of 17 mW/cm-K at 77 K can be achieved which is an order of magnitude *larger* than that of any amorphous insulations.

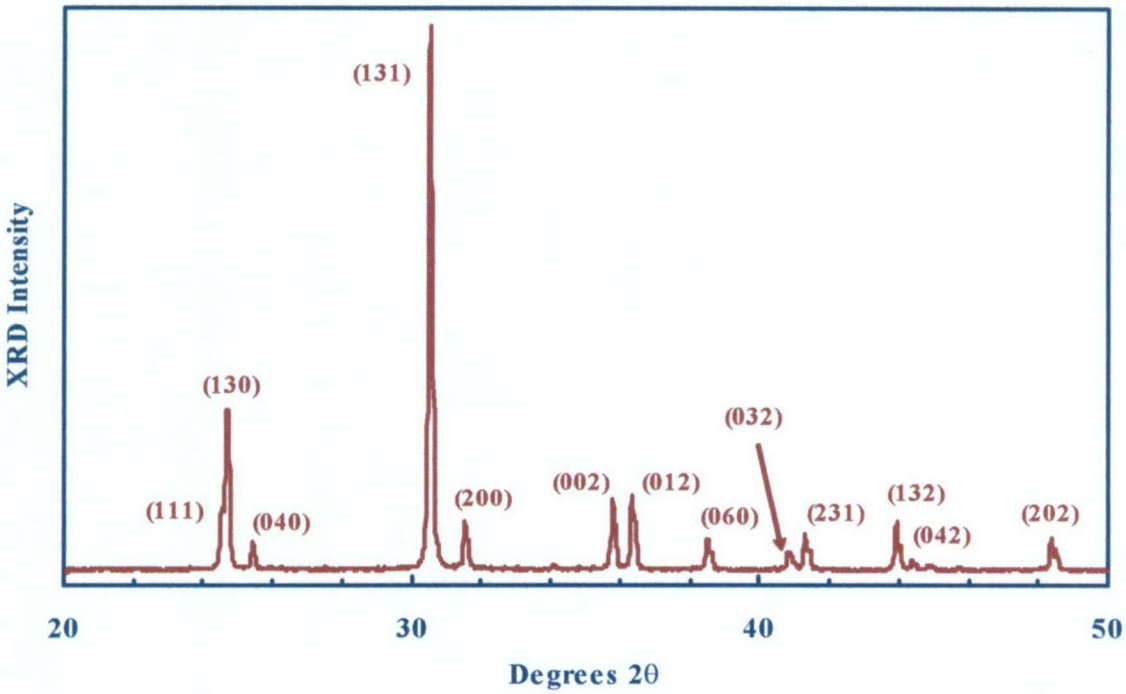

FIGURE VI-1

X-ray diffraction pattern of single-phase $NiNb_2O_6$ powder (Lot #179-9-10).

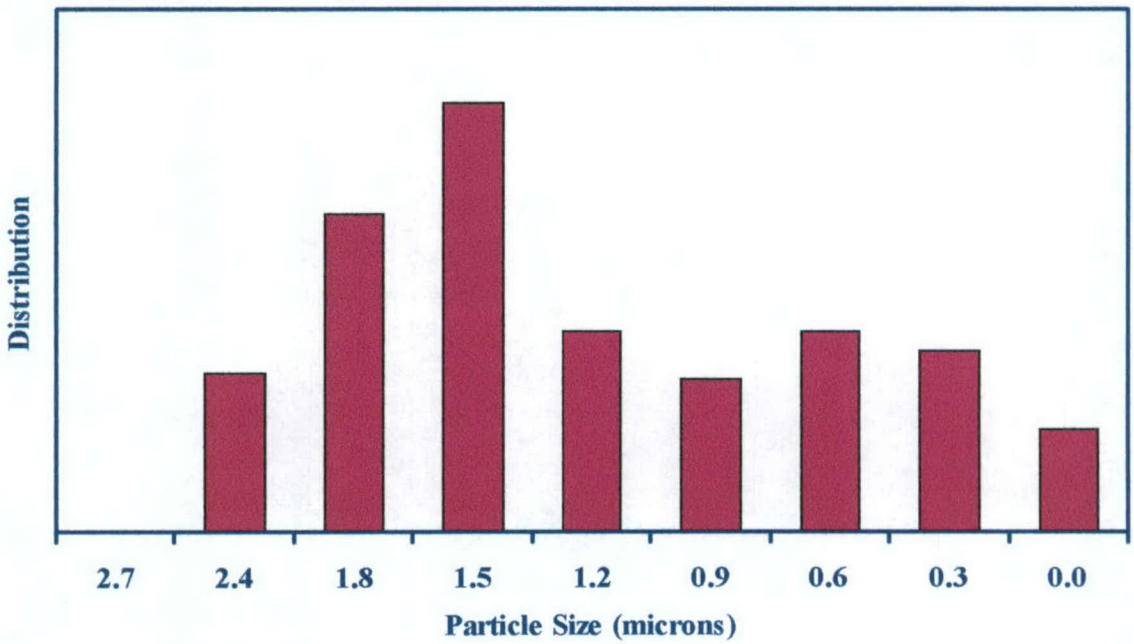

FIGURE VI-2

Particle size distribution of $NiNb_2O_6$ powder (Lot #179-9-10).

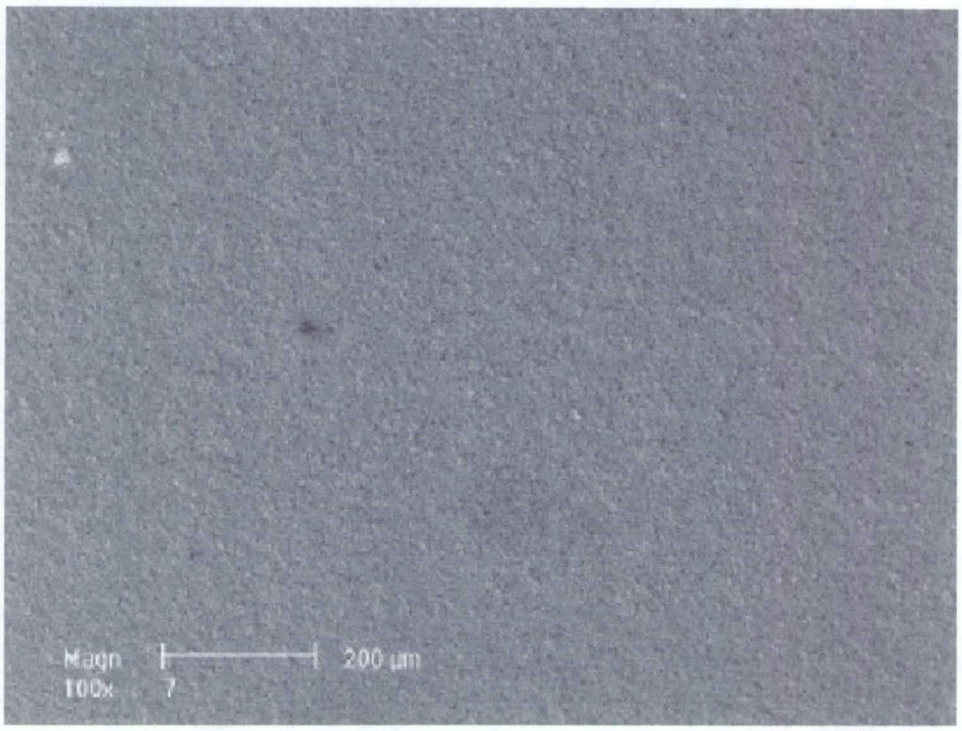

FIGURE VI-3

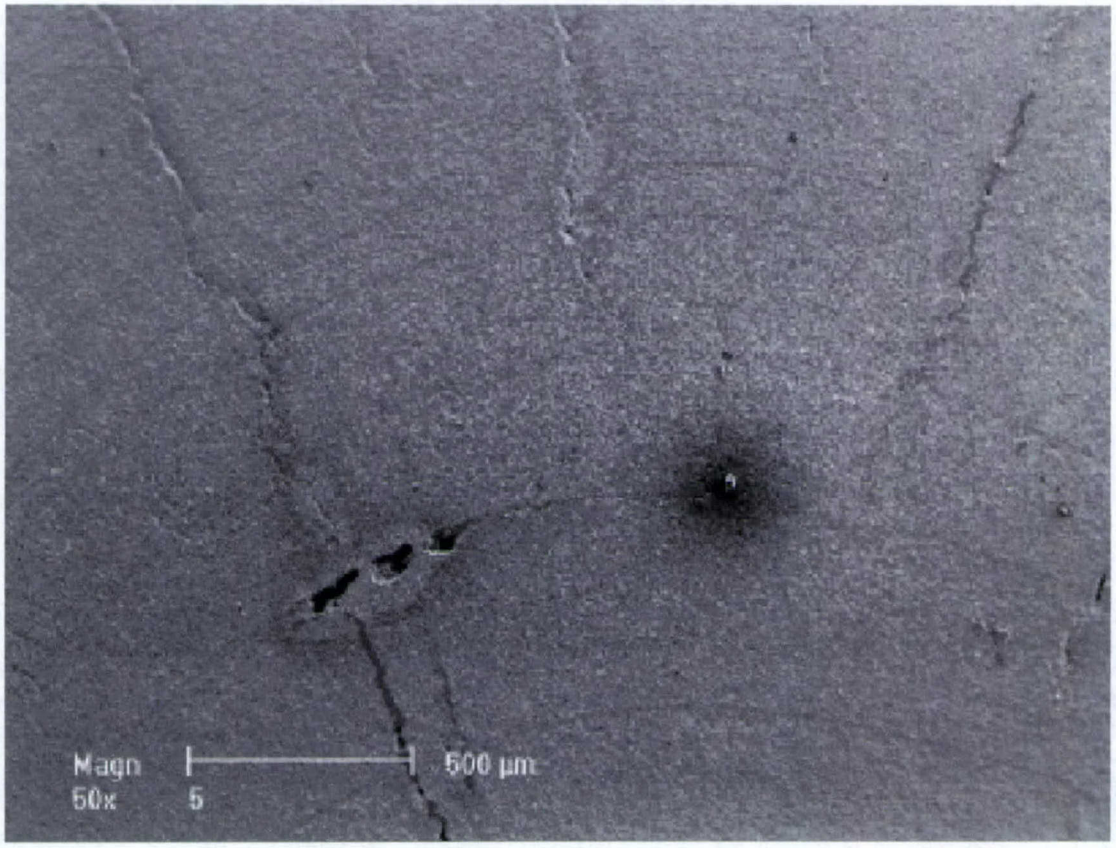

FIGURE VI-4

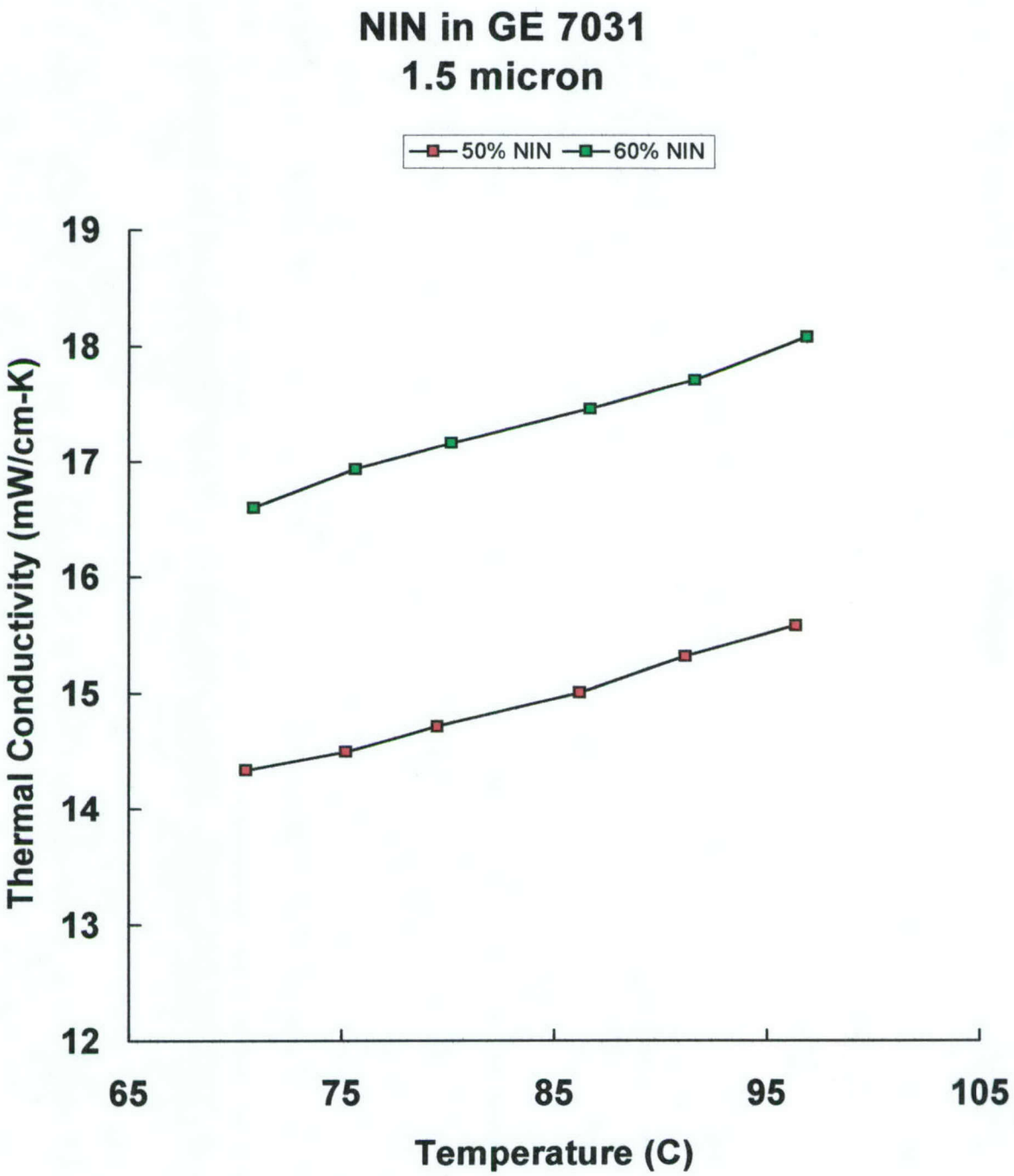
NIN in GE 7031
1.5 micron
50% NIN
60% NIN
Thermal Conductivity (mW/cm-K)
19
18
17
16
15
14
13
12
65
75
85
95
105
Temperature (C)

FIGURE VI-5

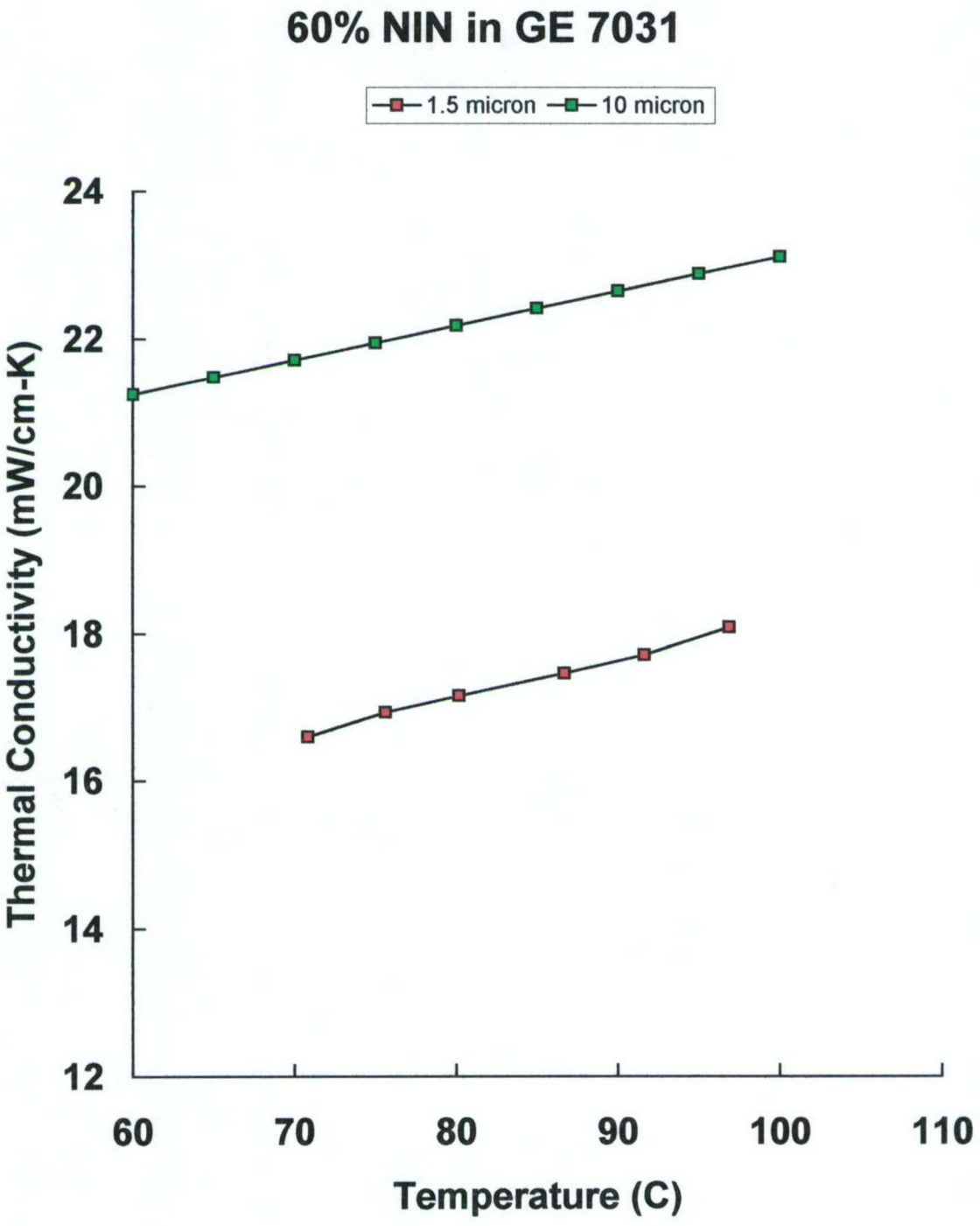
60% NIN in GE 7031
1.5 micron
10 micron
Thermal Conductivity (mW/cm-K)
24
22
20
18
16
14
12
60
70
80
90
100
110
Temperature (C)

FIGURE VI-6

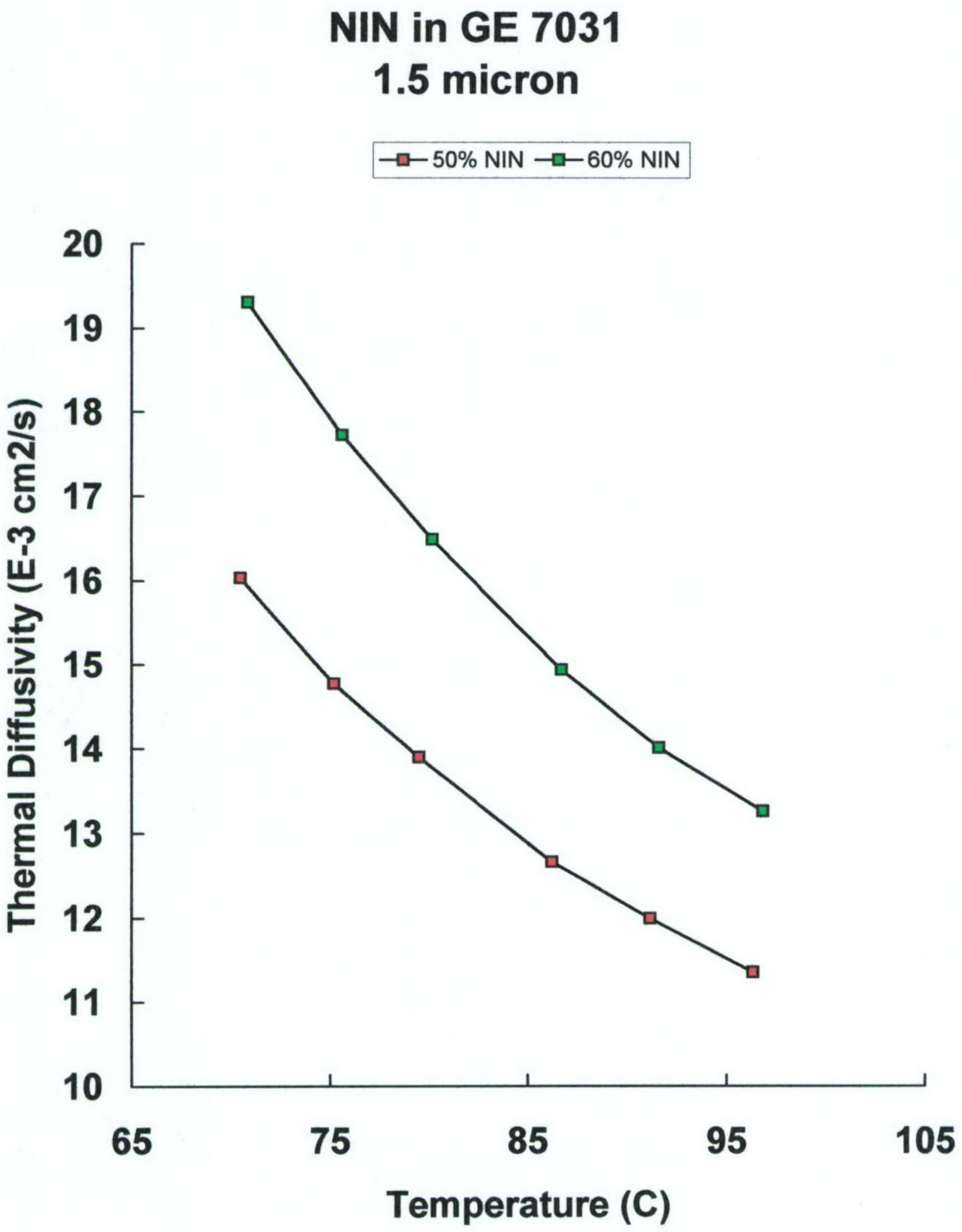
NIN in GE 7031
1.5 micron
50% NIN
60% NIN
Thermal Diffusivity (E-3 cm2/s)
20
19
18
17
16
15
14
13
12
11
10
65
75
85
95
105
Temperature (C)

FIGURE VI-7

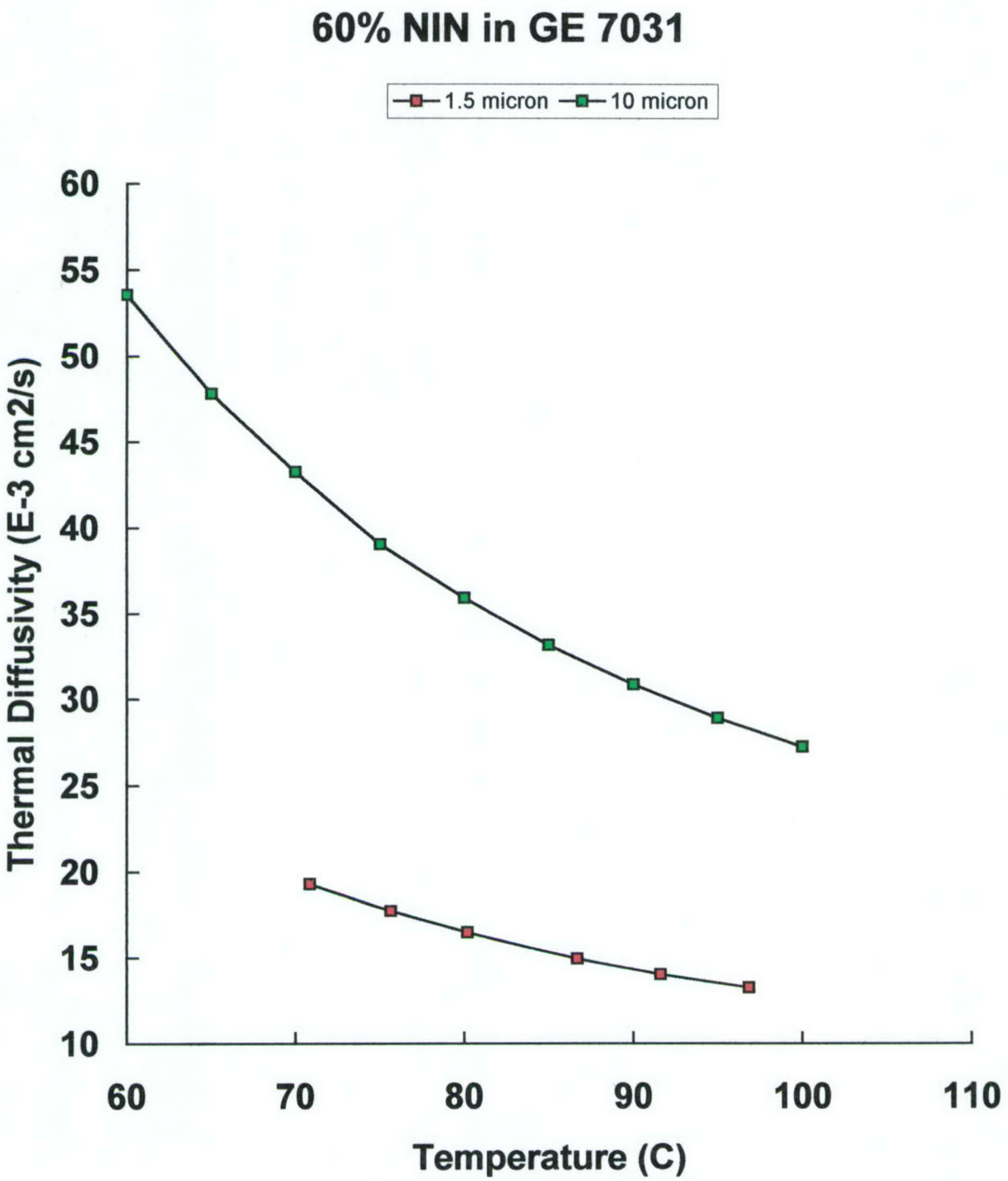
60% NIN in GE 7031
1.5 micron
10 micron
Thermal Diffusivity (E-3 cm2/s)
60
55
50
45
40
35
30
25
20
15
10
60
70
80
90
100
110
Temperature (C)

FIGURE VI-8

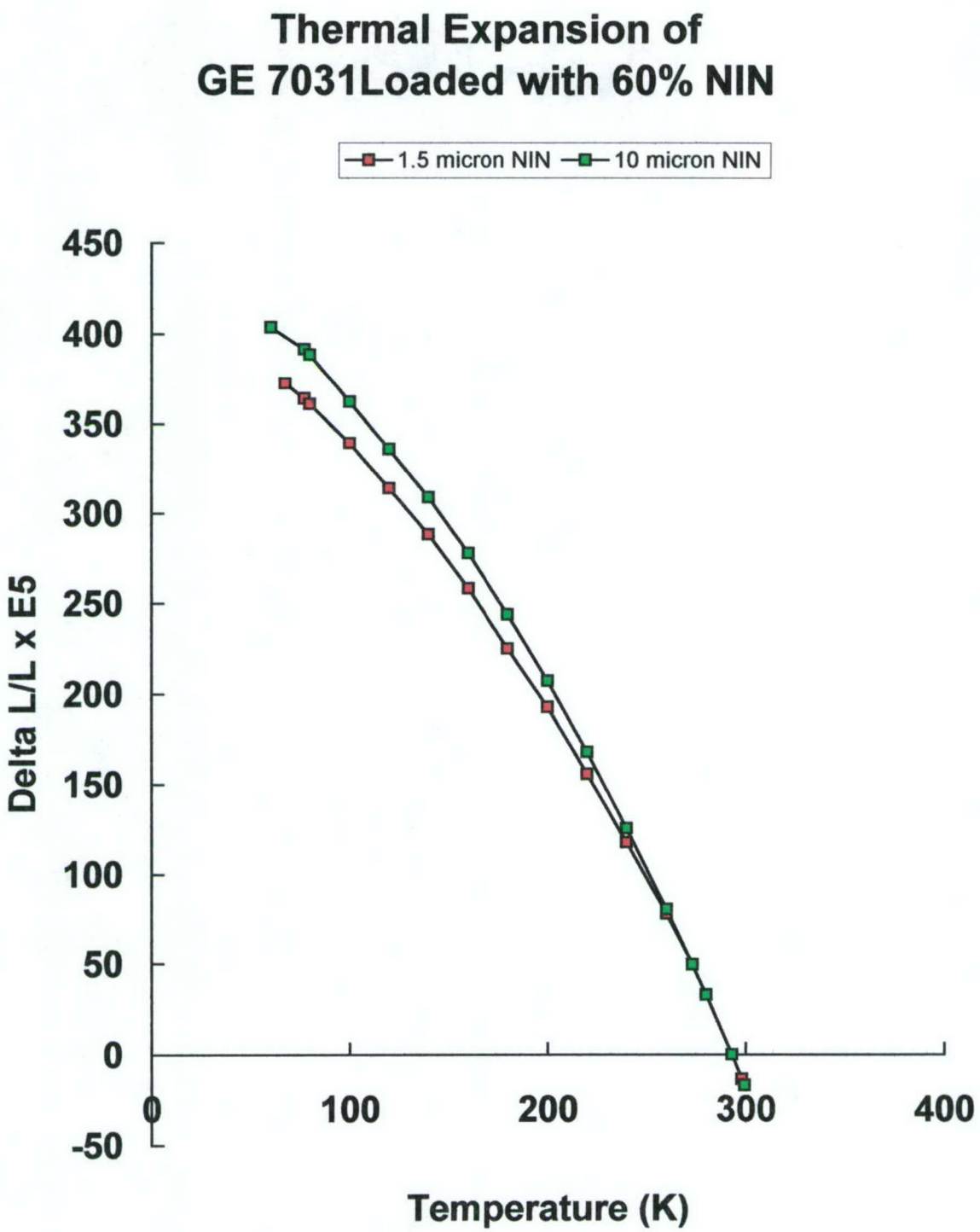
Thermal Expansion of
GE 7031Loaded with 60% NIN
1.5 micron NIN
10 micron NIN
450
400
350
300
250
200
150
100
50
0
-50
Delta L/L x E5
0
100
200
300
400
Temperature (K)

FIGURE VI-9

VII. ASSESSMENT OF SPUTTERED INSULATING FILM

STMC was contracted by Ceramphysics, Inc. (CPI) to sputter a high-thermal-conductivity ceramic onto HTS ribbon samples (provided to CPI by Superpower). Based on CPI's recommendation, we prepared powders and a sputtering target of Zn_2GeO_4 (ZGO).

The process parameters provided by CPI for the ZGO material did not prove useful and an alternative, higher temperature, calcinations and sinter process was developed to produce a target that was phase pure as confirmed by XRD.

From the phase pure ZGO material we fabricated a 2.9 x 0.125" sputter target and bonded that ceramic into a 3" diameter by 0.187" copper backing cup to facilitate maximum heat sinking with the water cooled cathode of our sputter system. We utilized a Denton vacuum coating system with a load lock.

Based on our prior experience sputtering multi-component metal oxides we estimated that the deposition rate, at modest powers, would be on the order of 300 Angstroms per hour. The request from CPI was for films at 1 micron and 10 microns. Two depositions were done to determine the actual deposition rate. We performed a target break-in step where the system was pumped overnight to it base pressure and the the target was energized at 20 watts (Rf) for 12 hours, then gradually ramped to 60 watts. The initial deposition of 24 hours resulted in a film at 5,600 A, or 0.56 microns, thick.

This film was characterized by XRD and proved to be amorphous. The deposition was done at room temperature although there was some self-heating that occurred due to the proximity of the sputter plasma to the substrate (microscope slide). We estimate that the self-heating was on the order of 100 – 150 °C. The resulting deposition rate of 233 A per hour was below our expectations, and actually not very particle, so we did a second deposition at 80 watts Rf for 24 hours with only a modest increase in film thickness.

The film deposited at 80 watts for 24 hours was slightly thicker at 5,700 A. The 33% increase in Rf sputter power resulted in only a 2% increase in deposition rate. Due to time and budget constraints we were not willing to push the ceramic target to its breaking point in order to determine the maximum deposition rate. That could be included in a Phase II work plan. This film was also characterized by XRD and was amorphous.

Based on our inability to generate a crystalline films at room temperature (or 150 °C) we investigated possible post-deposition annealing steps. The HTS ribbon supplier, Superpower, informed us that the maximum annealing temperature for a fully oxygenated YBCO ribbon was 400 °C. Accordingly, we annealed the ZGO film (on glass) in air for 2 hours. That annealed film was characterized by XRD and was still amorphous.

We then decided to try an in-situ anneal of the thin film during deposition. Our sputter system is equipped with a substrate heater capable of a maximum temperature of 350 °C. We performed another 24 hour deposition at 80 watts and 350 °C using two substrates, one glass and the other a pure copper foil. Those films exhibited several problems including poor adhesion and cracking. We were able to characterize the film on glass by XRD but it was still amorphous.

- A literature search was then performed on ZGO and we determined that the temperature required to crystallize a film was on the order of 620 °C in air. Using one of the films deposited on glass we performed an anneal, in air, on the film and it was successfully converted at that temperature.

SUMMARY

Powders, a sputter target and several thin films of ZGO were prepared in order to investigate the feasibility of depositing crystalline high-thermal-conductivity material on HTS ribbons under conditions that would not degrade the superconductive properties of the HTS material. We experimented with two deposition rates and several post-deposition and in-situ annealing temperatures. We were unsuccessful making crystalline films of ZGO below 400 °C but were able to demonstrate that crystalline films could be manufactured by Rf sputtering at room temperature (nominally 150 °C) and a post anneal at 600 °C.

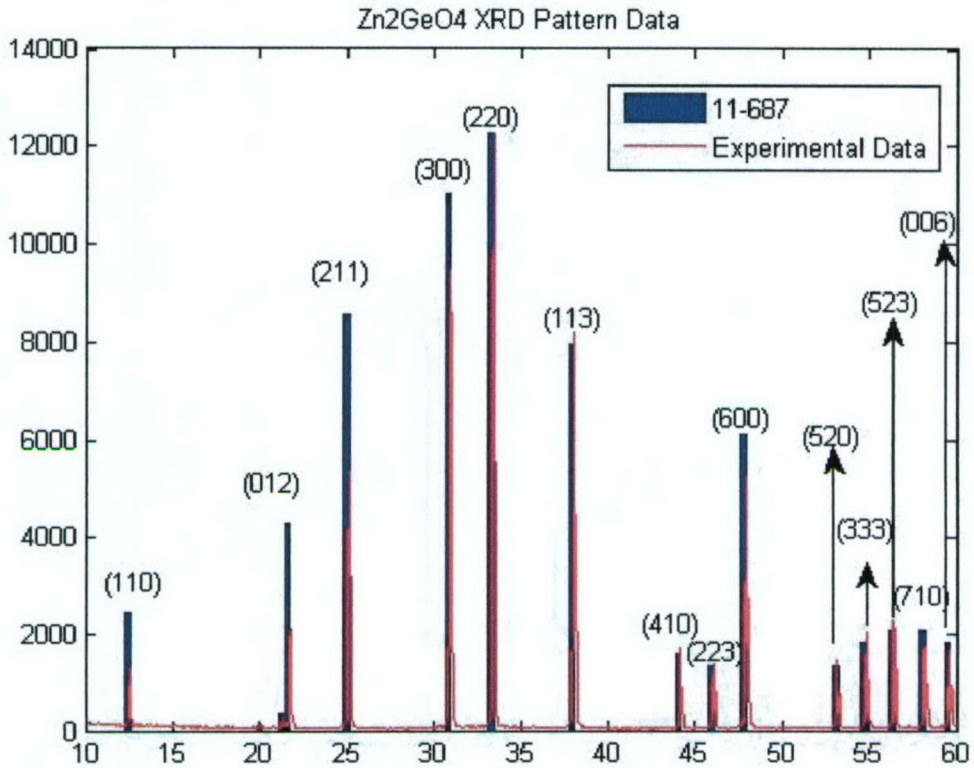

FIGURE VII-1

X-ray diffraction pattern from a coupon of ZGO material prepared by STMC's process

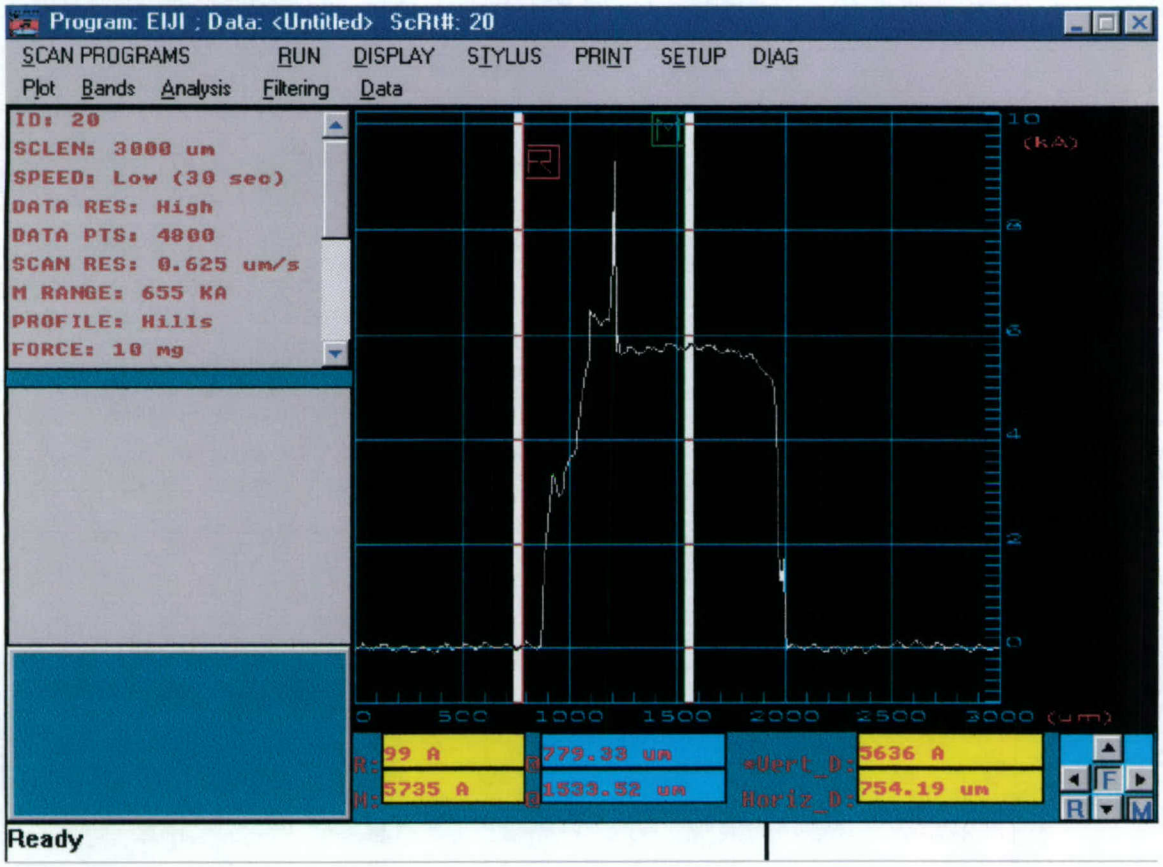

FIGURE VII-2

Film thickness for ZGO film deposited at 60 watts Rf for 24 hours

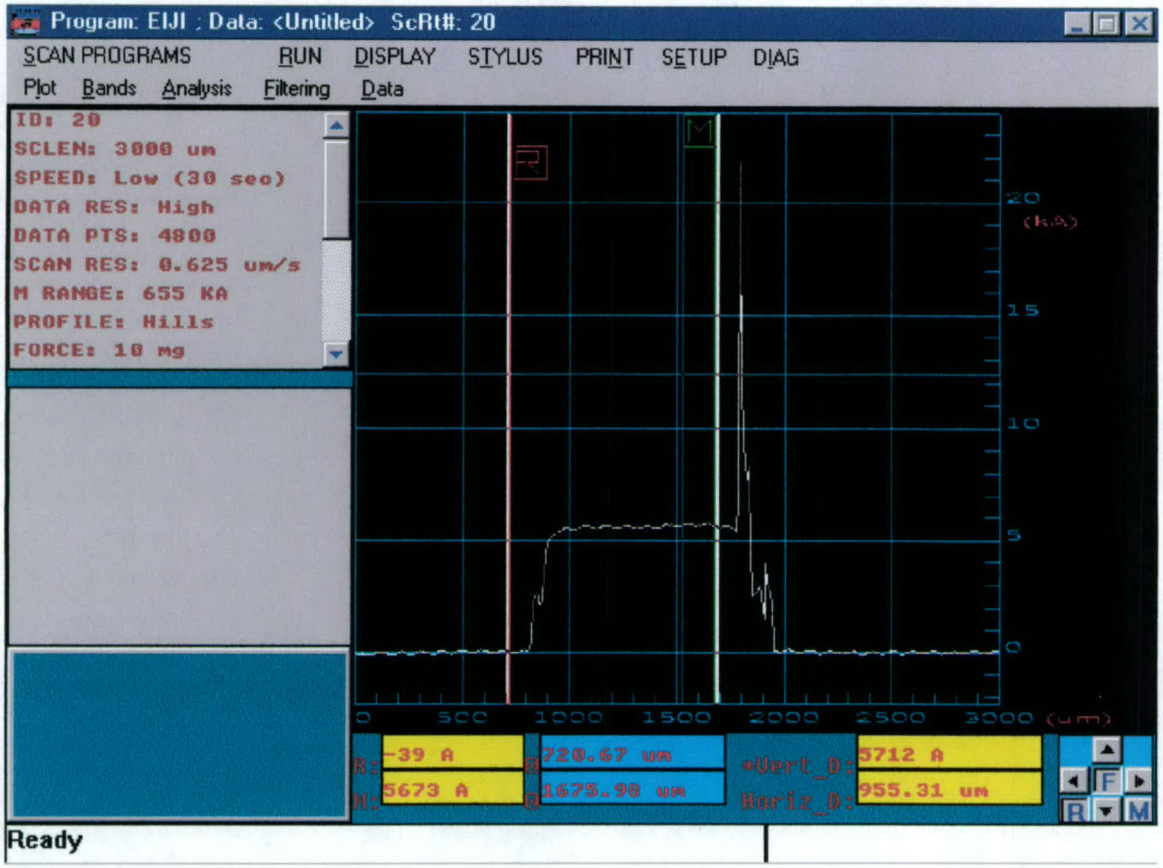

FIGURE VII-3

Film thickness after 24 hours at 80 watts Rf

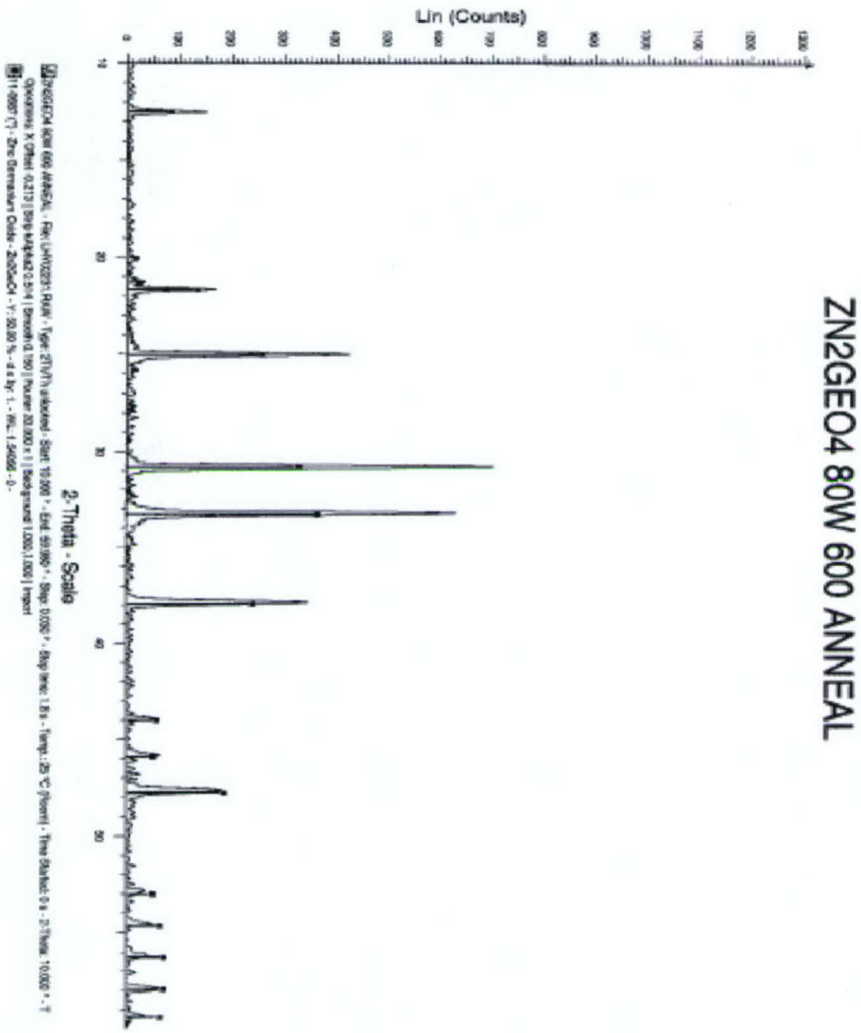

FIGURE VII-4

XRD of ZGO film deposited for 24 hours at 80 watts RF with a post-deposition anneal at 600 °C

VIII. THREE-DIMENSIONAL THERMAL MODELLING

A. SUMMARY

In this STTR effort, the thermal stabilization for high-temperature superconductors YBCO made of a composite with Ni and sheathed with the differently dielectric materials 60NN, ZN_2GeO_4 and CRYOVARISTORS is studied using a numerical simulation. The simulation uses transient, two dimensional energy equations with temperature–dependent properties and a novel current sharing model. The thermal stabilization of superconductors against any disturbance is affected by the distribution of the temperature and the ohmic heat generation caused by the flowing currents. A novel current sharing model was developed that is based entirely on current redistribution in the superconductor and the stabilizer depending on the local potential difference corresponding to the electrical resistivity between domains. The simulation results indicate that the characteristics of normal zone propagation based on the dielectric materials above mentioned remain somewhat similar to each either. The dielectric layers play a rather insignificant role for the convective heat removal from the superconductor tape surface. Nonetheless, they are critical in the transient phase immediate after the disturbance. On the other hand, the thermal properties of dielectric materials appear to have significant influence on the thermal stability of the high-temperature superconductors.

B. INTRODUCTION

An important issue concerning the quench protection of superconductors is to obtain an effective thermal stabilization of superconductors against any external disturbance. The thermal stabilization is affected by the distribution of temperature and the ohmic heat generation caused by flowing currents [1-4]. In the case of decreasing ohmic heat generation, the normal zone propagation collapses with time and the superconductor becomes stable. Therefore, the heat removal plays a very important role for decreasing the temperature in the sample and herewith stable normal zone propagation. This is related to how quick the generated heat is transferred from the superconductor outwards.

A number of theoretical studies are performed to investigate the current sharing in a superconductor [5-6]. One common current sharing model used [6-8] assumes that the super conductor carries the critical current corresponding to the local temperature and the excessive current splits, going into the stabilizer. Determining a critical current is the most important point of the common sharing model. Therefore the results of the common current sharing model are enhanced only with perfect critical currents.

As one of the major accomplishments of this STTR Phase 1 effort, a novel current sharing model, which doesn't use the critical current for determining the current distribution, was developed. The current redistribution in the superconductor and stabilizer depends only on the local potential difference corresponding to the electrical resistivity between domains.

The major objective of this study is to identify and to discus the effects of three dielectric materials provided by CeramPhysics, Inc. on the thermal stabilization for high-temperature superconductors YBCO made of a composite with Ni. They are 60NN, ZN_2GeO_4 and CRYOVARISTORS. The numerical simulation uses transient, two dimensional energy equations with temperature–dependent properties and the newly developed, novel current sharing model.

C. GOVERNING EQUATION

The temperature distribution in the composite sample including both the superconductor YBCO and the stabilizer Ni is governed by the transient heat equation in two dimensional form:

$$\gamma C\frac{\delta T}{\delta x}=\frac{\delta}{\delta x}\left(k\frac{\delta T}{\delta x}\right)+\frac{\delta}{\delta y}\left(k\frac{\delta T}{\delta y}\right)+\rho J^2 \qquad \text{(VIII-1)}$$

with initial and boundary conditions

$$T(x,y,t)=T_b \qquad \text{(VIII-2)}$$

$$\delta T(0,y,t)/\delta x=0 \qquad \text{(VIII-3)}$$

$$\delta T(L,y,t)/\delta x=0 \qquad \text{(VIII-4)}$$

$$\delta T(x,0,t)/\delta y=0 \qquad \text{(VIII-5)}$$

$$\partial T(x,D/2,T)/\partial x=-(h/k)(T(x,D/2,t)-T_b) \qquad \text{(VIII-6)}$$

where γ ,C, k and ρ represents the density, specific heat, thermal conductivity and electric resistivity, respectively. The representation of h is a convective heat transfer coefficient for a face–cooled tape. Note that all properties are temperature dependent, which represents a major nonlinearity to the problem and thus requires numerical iteration in the spatial domain for a given time. T_b is the bath temperature and J is the current density. The last term (source term) in the governing equation is the joule heating either in the YBCO or the Ni stabilizer so that the superconductor becomes intrinsically unstable. Since both the electric resistivity and the current distribution are strong functions of temperature, an iterative procedure in computation is thus required.

A current sharing model is required to calculate the source term of equation (1), ρJ^2,. It is necessary to link the temperature and the amount of current carried in the superconductor and in the stabilizer. An approach developed earlier by [5-8] is based on

two general assumptions: (1) the superconductor carries the critical current density , J_c, corresponding to the local temperature T, and T_b ,and (2) a linearly inverse relation between J_c and T .; i.e., for $T_c < T < T_{co}$ over an entire cross-section of the superconductor,

$$J_c(T)/J_{co}(T) = (T_{co} + T)(T_{co} + T_b) \qquad \text{(VIII-7)}$$

where $T_{co} = 92K$, $J_{co} = 1.0x10^5 A/m^2$, $1.6\ 10^8\ A/m^2$ and $1.6\ 10^9 A/m^2$ are assumed.

D. NOVEL CURRENT SHARING MODEL

The new current sharing model is based entirely on current redistribution in the superconductor and the stabilizer depending on the *local* potential difference corresponding to the electrical resistivity between domains. Applying Kirchhow's first law between the control volumes CV we obtain the potential difference [9]:

$$\Delta U = IR \qquad \text{(VIII-8)}$$

where U, I and R represents the electric potential, electric current and electric resistivity, respectively. The electric resistivity is a physical property of the superconductors and the stabilizer and depends on the temperature. The distribution of electrical potential on control volumes is therefore determined by the temperature distribution.

To determine the distribution of the electric potential we use Kirchhow's second law stating that for each control volume a current conservation exists [9]:

$$0 = \sum_{x,y} I = \sum_{x,y} \frac{\Delta U}{R} \qquad \text{(VIII-9)}$$

or in two dimensional differential form

$$0 = \frac{\delta}{\delta x}\left(\frac{1}{R}\frac{\delta U}{\delta x}\right) + \frac{\delta}{\delta y}\left(\frac{1}{R}\frac{\delta U}{\delta y}\right) \qquad \text{(VIII-10)}$$

with boundary conditions

$$\delta U(0,y)/\delta x = U_{in} \qquad \text{(VIII-11)}$$

$$\delta U(L,y)/\delta x = U_{out} \qquad \text{(VIII-12)}$$

$$\delta U(x,0)/\delta y = 0 \qquad \text{(VIII-13)}$$

$$\delta U(x,D)/\delta x = 0 \qquad \text{(VIII-14)}$$

The differential equation of the electric potential above seems similar to the differential equation of the temperature distribution for a steady state case with no search term. On the other hand the analogy between electric current flow and heat conduction flow is also used in heat transfer to determine the heat conductivity.

E. NUMERICAL PROCEDURES

The numerical solution of the governing equation uses a finite difference scheme with a control volume formulation [10]. This approach, often termed as, "the finite volume method," ensures a perfect energy balance on each discrete domain. The discretization of the equation uses a fully implicit method that provides unconditional stability for computation. The Alternate Direction Iterative (ADI) method is used to solve the discrete algebraic equations [5]. The tape is discretized in a 50x15 grid along the x direction (x axis)and y direction (y axis), respectively, for a typical domain of 0.25 mm YBCO layer, 0.3mm Ni lower layer and 0.3mm Ni upper layer, as shown in Figure VIII-1.

To initiate a normal zone, an energy pulse is supplied to a small region near the left edge of the superconductor: i.e. $0<x/D<1$ and $0<y/D<0.175$. A converged solution is attained over a 200 ms duration with 10 ms time increments.

For each iteration step, the source term of the joule heat generation is determined with a new electric resistivity and current flow, calculated from a new electric potential distribution depending on the temperature. The solution of the governing equation of electrical potential for the same control volumes uses the same numerical approach described above.

F. RESULTS AND DISCUSSIONS

The issues concerning thermal properties of dielectric materials on the thermal stability of a Ni sheathed YBCO has been examined using the new electric models. Three dielectric materials provided by Ceram Physics, Inc. are discussed in the present report. They are

1- 60NN
2- ZN_2GeO_4
3- CRYOVARISTORS

The thermal properties are tabulated below in Table VIII-1.

Table VIII-1

Thermal Conductivity (K), Specific Heat (C) and Thermal Diffusivity (k) Data

Data shown in Table VIII-1 reveal a monotonically increasing order in the magnitude of dielectric thermal properties from 60NN, ZN_2GeO_4 to CRYOVARISTORS. For completeness, Table VIII-2 gives the thermal properties of YBCO and Ni.

60NN			
T	**K**	**C**	**k**
[K]	mW/cmK	J/cm3K	cm2/s
60	21.245	0.397	5.36E+04
70	21.713	0.502	4.32E+04
80	22.181	0.618	3.59E+04
90	22.648	0.735	3.08E+04
100	23.116	0.848	2.72E+04

ZN_2GeO_4			
T	**K**	**C**	**k**
[K]	Mw/cmK	J/cm3K	cm2/s
60	2.95E+02	5.38E-01	5.49E+05
70	2.40E+02	6.48E-01	3.71E+05
80	2.17E+02	7.58E-01	2.86E+05
90	1.88E+02	8.67E-01	2.17E+05

CRYOVARISTOR			
T	**K**	**C**	**k**
[K]	mW/cmK	J/cm3K	cm2/s
60	5.95E+02	7.11E-01	8.37E+05
70	6.12E+02	8.53E-01	7.17E+05
80	6.12E+02	9.68E-01	6.32E+05
90	6.12E+02	1.17E+00	5.22E+05

Table VIII-2

Thermal Conductivity (K), Specific Heat (C) and Thermal Diffusivity(k) Data

YBCO			
T	**K**	**C**	**k**
[K]	W/cmK	J/cm3K	cm2/s
20	0.446	2.90E-05	1.61
25	0.551	7.00E-05	1.23
30	0.624	1.00E-04	0.98
35	0.692	1.30E-04	0.76

Ni			
T	**K**	**C**	**k**
[K]	W/cmK	J/cm3K	cm2/s
20	141.0	4.00E-04	355.2
25	112.2	7.00E-04	165
30	80.2	1.17E-03	77
35	49.9	1.70E-03	33

The numerical simulation are conducted for three different initial (bath) temperatures: i.e. T_b =20 K, 40 K and 80 K, for the constant electric potentials differences ($\Delta U = U_{in} - U_{out} = 0.00001V$) (It yields an operating current density: J= $5.610^8\ J/m^2$) and for the levels of initial disturbance energy E=$1x10^9\ J/m^3$ with the convective cooling (h=10 W/m^2). For the new current sharing model the desired currents are supplied by setting the corresponding boundary conditions of the electric potential.

Figure VIII-1 presents the results for the temperature distribution along the centre line of the superconductor with the three dielectric isolation layers for the bath temperature, i.e. T_b = 80 K. All cases are subjected to the same lower initial disturbance of E=$1x10^9$, a constant current potential difference and the same convective heat transfer (constant heat transfer coefficient). The temperature is shown in dimensionless form, $\theta = (T - T_b) / (T_{co} - T_b)$. Generally, the results with the three differently dielectric materials indicate the same characteristics for the temperature distribution with the collapsing trend. After 100 ms the whole temperature in the sample falls below the critical temperature of the super conductor. This implies that using the dielectric materials with the differently thermal properties doesn't change the temperature distribution in the operation conditions.

In the case of the lower bath temperature around the sample with the dielectric CRYOVARISTORS the temperature of the sample is shown in Figure VIII-2. Except the lower temperature level, the effect of the dielectric materials on the temperature distribution in the sample remains similar to that of the higher bath temperature.

- Figure VIII-3 discloses the results of the temperature distribution in the sample made of YBCO and Ni layers without the dielectric layers (3 Layer). The sample without the electric layer achieves the same temperature distribution as that of the sample with the dielectric layers (5 Layers) under the same operating conditions as above, but only after 200 ms. The effect of the dielectric layers on the temperature distribution is observed at the beginning phase of simulation. The temperature of the normal zone in the sample with 3 layers (without dielectric) lies relatively higher than that of sample with the dielectric layers.

The convective heat removal from the surface of the sample with and without the dielectric materials is compared in Figure VIII-4. The trend of the heat transfer similar to that of the temperature distribution in the sample is observed. It implies that the convective heat transfer controls the temperature distribution. Theoretically, the temperature distribution in the superconductor and the stabilizer is controlled by a combined effect of heat transfer and joule heating, which causes current flows.

This energy is transferred by conduction in both longitudinal (x) and transverse direction (y, z). Heat transferred in the transverse directions will be removed by the convective cooling on the outer surface of the dielectric layer. Since the stabilizer Ni has a much higher thermal conductivity than both YBCO and the dielectric layer, by about 2 to 3orders of magnitude, the heat conduction in the longitudinal direction become predominant in the Ni sheath (Table VIII-1-2). This implies that the thermal properties of dielectric material have no effect on the longitudinal heat transfer unless their magnitudes are comparable to those of Ni.

Heat in the transverse direction is transferred through the thermal resistance of three material layers and convective resistance in series. For the calculation of such a thermal resistance per unit length, the following expression is used:

$$R_{transverse} = D_{YBCO} / k_{YBCO} + D_{Ni} / k_{Ni} + D_{Dielec} / k_{Dielec} + 1/h \qquad \text{(VIII-15)}$$

In this equation the convective resistivity between the outer surfaces of the electric layer and the ambient (bath) temperature is a larger resistivity than that of others because the thickness of the YBCO, Ni and dielectric materials layers (D) is very small. The value of the heat transfer coefficient, 10 W/m^2, is a reasonable and realistic assumption. The overall heat transfer is only enhanced with the improvement of the condition of convective heat transfer. The thermal diffusion of the dielectric materials appears to have no effect in the present system.

The heat removal from the sample will be more dependent on the higher thermal conductivity dielectric materials and a higher convection coefficient. In the case of an improved heat convection condition a higher thermal conductivity of CRYOVARISTORS is very desirable. However, to prevent the heat transfer from the zone of Ni into the zone of the superconductor the higher thermal conductivity of the dielectric materials than that of YBCO is required.

- A high specific heat of dielectric materials is desirable in the use for additional energy storage in case of imposing of disturbance energy. A higher thermal conductivity of dielectric materials than that of YBCO and Ni is required to obtain a heat transfer flowing outward in the transverse direction, in other words to reduce the heat conduction flowing in towards YBCO. All the dielectric materials considered here have specific heat of about 2 to 5 times greater than those of YBCO or Ni. In addition, thickening the dielectric layers is recommended to absorb more excessive disturbance energy. Further simulations with the dielectric materials will yield more results about the effect of the new model on the normal zone propagation among a larger external disturbance, current density, bath temperature and cooling.

F. SUMMARY

This report presents simulation results of the thermal stabilization for high-temperature YBCO superconductor composite with Ni and sheathed with the differently dielectric materials 60NN, ZN_2GeO_4 and CRYOVARISTORS provided by CeramPhysics, Inc. One of the major accomplishments resulted from this STTR Phase 1 effort is the development of a novel, differential current sharing model and its implementation in the simulation code. This model is fundamentally superior to any existing models based primarily on algebraic approximations. A systematic evaluation shows that algebraic current-sharing model often over-predicts thermal instability, which may render more conservative measure in quench protection.

The numerical simulation solves the transient two dimensional energy equations with temperature–dependent properties. The finite volume method is applied for the numerical solution of the governing equation. As mentioned earlier, a novel current sharing model based on the local potential difference corresponding to the electrical resistivity between domains is used to determine the joule heat generation. The operation condition for the numerical simulations are three different initial (bath) temperatures: i.e. T_b =20 K, 40 K and 80 K, a constant electric potential differences ($\Delta U = U_{in} - U_{out} = 0.00001V$, equivalent to operating current density: J= $5.6 10^8$ J/m^2) and an initial disturbance energy E=$1x10^9$ J/m^3 with convective cooling h=10 W/m^2. The numerical simulation indicates that in the same bath temperature, the three different dielectric materials have similar effects on the temperature distribution. On the other hand, the rate of the convective heat transfer from the sample surface also remains similar to each other.

Energy generated in the composite YBCO sample is transferred by conductive in both longitudinal (x) and transverse direction (y, z). Heat transferred in the transverse direction will be removed by the convective cooling on the outer surface of the dielectric layer. The heat conduction in the longitudinal direction become predominantly in the Ni sheath. This implies that the thermal properties of dielectric material have insignificant effect on the longitudinal heat transfer unless their magnitudes are comparable to those of Ni.

- The heat in the transverse direction flows through the three material layers and then is removed convectively. For the overall heat transfer, the thermal resistivity of the dielectric material is not the main thermal resistance compared to that of the heat convection imposed at outer surface of the sample. The overall heat transfer is critically dependent on the overall arrangement and geometry of magnet fabrication with more effective transverse heat conductance or convective heat transfer coefficient.

The higher thermal conductivity dielectric materials with a corresponding higher heat conductance will benefit the heat removal from a disturbed sample. Thus the higher thermal conductivity of CRYOVARISTORS is most desirable in this aspect. In addition, a higher thermal conductivity of CRYOVARISTORS than that of YBCO is beneficial for directing ohmic heating generated in Ni sheath further away from the superconductor. A high specific heat of dielectric material is desirable for transient energy storage during the immediately post disturbance period, hence suppress the formation of normal zone. However, this may adversely hinder the normal zone propagation speed and detection sensitivity, which makes the quench protection difficult. Future research focus would be placed on extension of the current modeling effort to system level involving realistic magnets.

nomenclature

C	Specific heat
D	Sample thickness
E	Disturbance energy
h	Heat transfer coefficient
I	Current
J	Current density
Jc	Current density of superconductor at given temperature
Jco	Critical current density at operating temperature
Jop	Operating current density
Js	Current density in stabilizer
k	Thermal conductivity
K	Thermal diffusivity
L	Conductor length
R	Electrical resistivity, Thermal resistance
T	Temperature
Tb	Ambient (bath) coolant temperature
Tc	Critical temperature at given current density
Tco	Critical temperature at zero current, 92 K
t	Time
U	Electrical potential
x	Coordinate
y	Coordinate

z	Coordinate

Greek

γ	Density
θ	Dimensionless diffusivity
ρ	Electric resistivity

Subscripts

sc	Superconductor
s	Stabilizer
in	inlet
out	outlet

References

1. Martin N. Wilson,'' Superconducting Magnets'', Oxford Science Publication, UK (1983).
2. Prochnow Dave, '' Superconductivity Experimenting in A New Technology'', TAB Books Inc., USA(1989)
3. Carr W. J. Jr. and Charles P. Poole, Jr., ''AC Loss and Macroscopic Theory of Superconductors'' Gordon And Breach Science Publisher, New York (1983).
4. Ovens J. Frank and Poole P. Charles, '' The New Superconductors'' Plenum Press. , New York and London (1996).
5. V.S. Kovner and R. G. Mints, Normal Domains in Large Multifilamentary Composite Superconductors, J. App. Phys. 75, 7538(1994)
6. M.K. Chyu and C.E. Oberly, Influence of Operating and Contact Thermal Resistance on The Normal Zone Propagation in Metal-Sheathed High-Tc Superconductor Tape, Cryogenics 32, 519 (1992).
7. M.K. Chyu and C.E. Oberly, Influence of Operating Temperature on Stability and Quench of Oxide High-Tc Superconductors, Cryogenic Engineering Conference, Huntsville USA, (1991).
8. M.K. Chyu and C.E., Effects of transverse heat transfer in normal zone propagation in metal –clad high temperature superconductor coil tape, Cryogenics (1992) 31 680-686.
9. Purcell M. Edward , '' Electricity And Magnetism'', Mc Graw-Hill, New York (1965)
10. S.V. Patankar, ''Numerical Heat Transfer an Fluid Flow'', Hemisphere Publication, New York (1980)

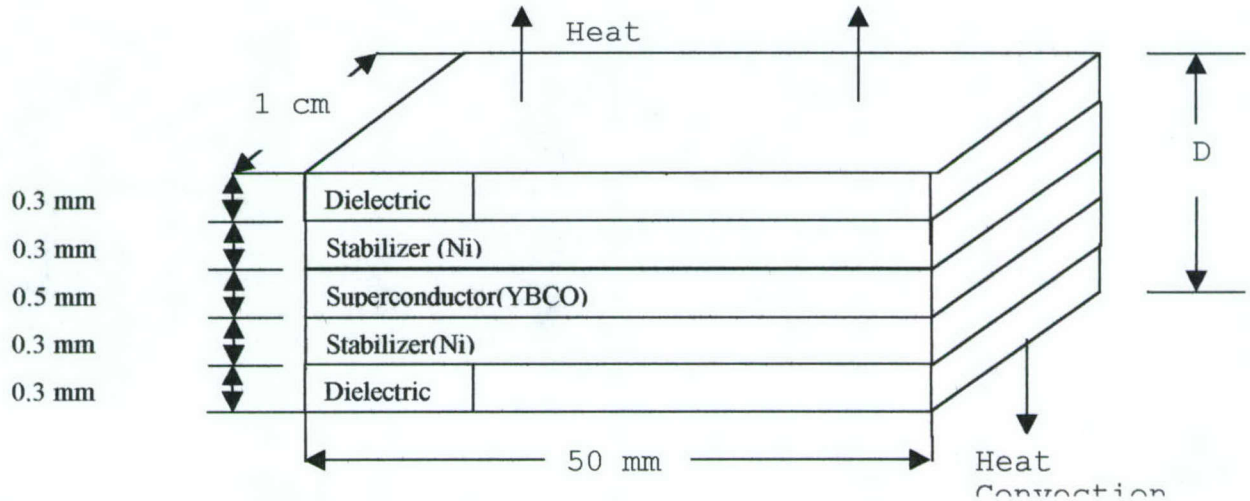

FIGURE VIII-1

YBCO-Ni Composite Samples

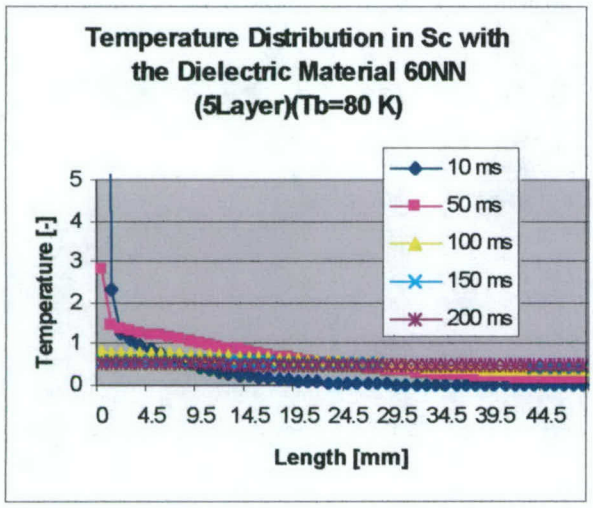

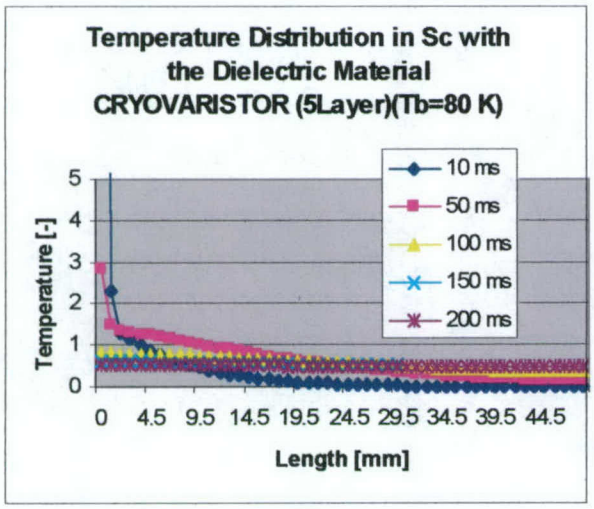

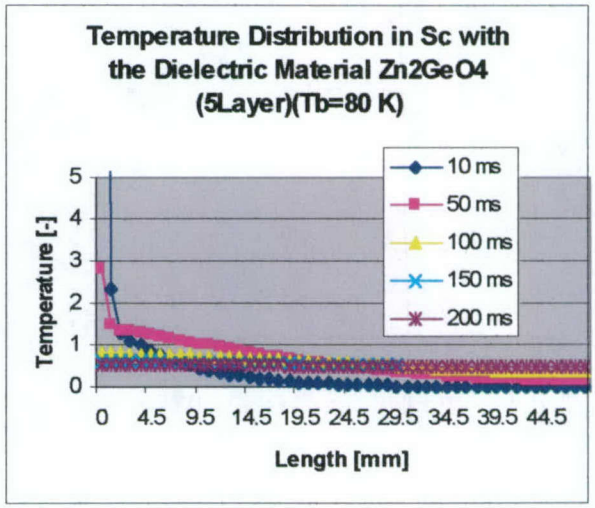

FIGURE VIII-1

The distribution of the temperature in the IYBCO covered with the dielectric materials: 60 NN, Zn_2GeO_4 and CRYOVARISTOR.

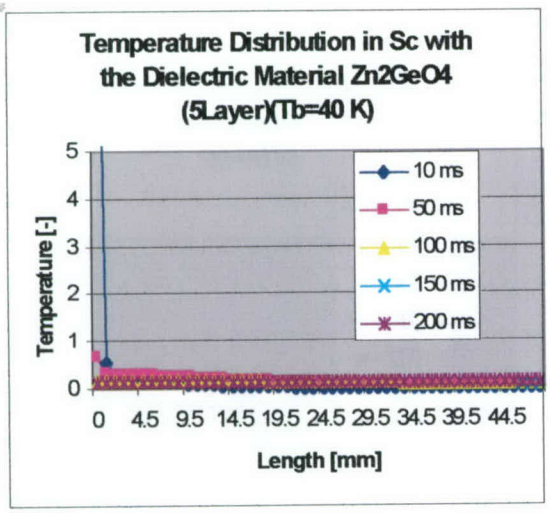

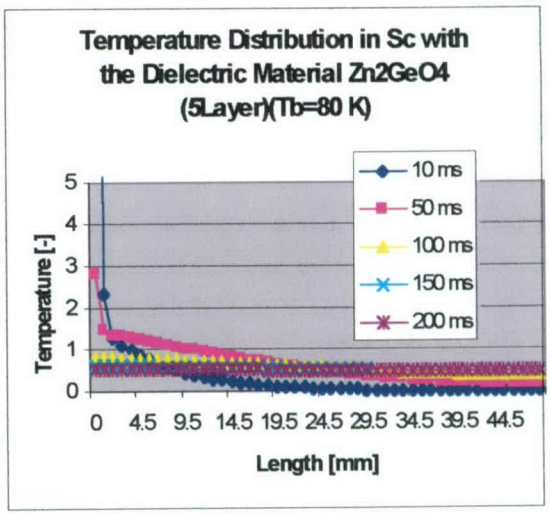

FIGURE VIII-2

Comparison of the temperature distribution for the differently bath temperature, T=40 K and 80 K (with the dielectric materials Zn_2GeO_4)

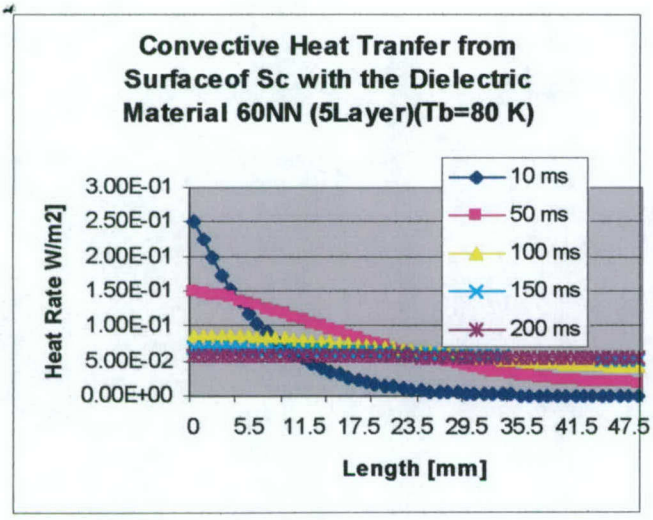

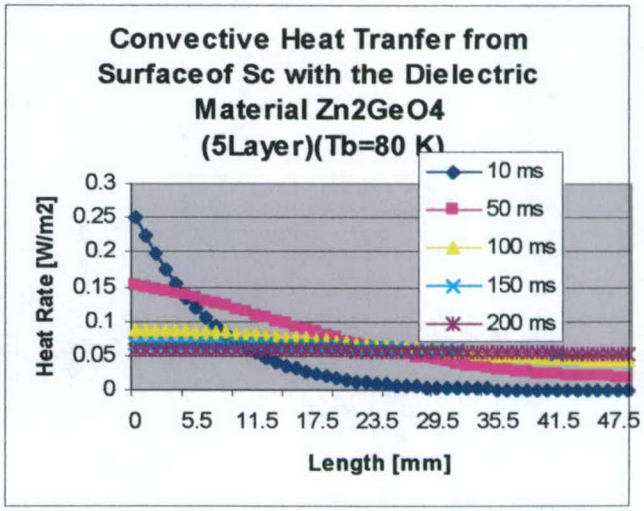

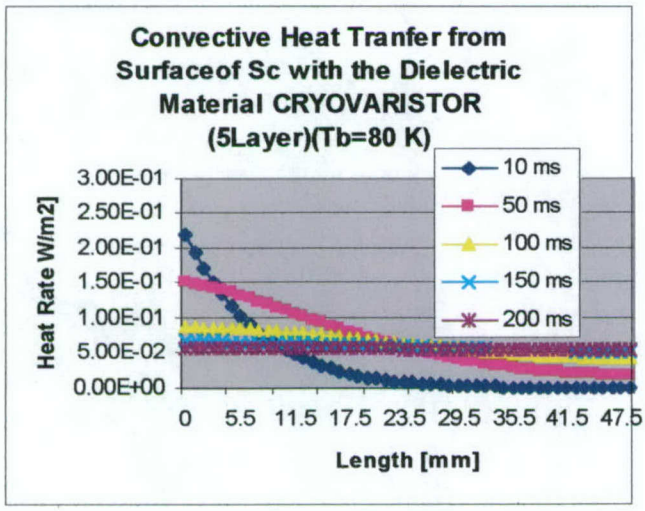

FIGURE VIII-4

Comparison of the convective heat transfer from the surface of YBCO with the differently dielectric materials: 60 NN, Zn_2GeO_4 and CRYOVARISTOR.

IX. CONCLUSIONS OF THE PHASE I STTR PROGRAM

A broad-based program has been successfully pursued to make assessments of four distinct strategies for the quench protection of HTS coils near 77 K -- diamond-film insulation, cryovaristor current shunt, loaded Formvar insulation, and a sputtered ceramic insulation. The three-dimensional thermal modeling of quench protection has provided important guidelines for judging the strategies, and a greatly improved modeling code has been developed in the program for doing so.

Boundary scattering substantially depresses the thermal conductivity of diamond films even though single-crystal diamond has a large thermal conductivity at low temperatures. A theoretical analysis indicates that a 10-micron thick diamond film would have a thermal conductivity of only 130 mW/cm-K at 77 K which is too small to be of interest from the thermal modeling of quench protection. Therefore, this strategy is not viable, given the high cost of these films.

The cryovaristor current shunt is modeled electrically. For this strategy to work, both sides of the HTS coil would have to have a Cu overlayer, and current would have to travel a considerable distance in one of the Cu overlayers to build the 1 kV/cm field needed to switch the cryovaristor. One full turn of the coil would also have to be sacrificed. There are two major drawbacks to this strategy: First, the current sharing in the cryovaristor requires a considerable electrical + thermal theoretical analysis; and second, the cryovaristor characteristic requires a substantial amount of impurities in the grain boundaries which may not be achievable with deposition methods limited to 400 °C. Therefore, this strategy requires a considerable development effort with a low probability of success.

The cryovaristor ceramic is very significant but for a *different* reason. Namely, this ceramic has a very large thermal conductivity at 77 K, 620 mW/cm-K, and is in fact the insulation material of choice from the thermal modeling. This conductivity is *due to the ZnO grains* [1] (i.e., the grain boundaries are not heat carriers) and is not boundary-scattering limited for films thicker than 5 micron. Therefore, ZnO, which is a simple ceramic, should be explored for quench protection using deposition methods which are consistent with the 400 °C constraint.

Measurements of Formvar loaded with 1.5 micron powders of a high-thermal-conductivity NN ceramic are made and show that Kapitsa resistance at the Formvar/ceramic interface depresses the thermal conductivity of the composites, 15 - 17 mW/cm-K at 77 K. Therefore, this strategy does not provide a desirable level of quench protection but does, however, provide an ultimate, practical backup strategy compared to any amorphous insulations.

Thin films of a high-thermal-conductivity ZG ceramic sputtered on substrates were amorphous and could not be crystallized without exceeding the 400 °C limitation of the HTS coil (e.g., 600 °C). Therefore, this strategy remains viable but alternate or modified deposition methods should be explored consistent with the 400 °C constraint because ZG has a large thermal conductivity at 77 K, 224 mW/cm-K, which is not boundary-scattering limited for films thicker than 5 micron.

In conclusion, the assessments of the initial four strategies are not encouraging for quench-protection of HTS tapes, but they are valuable for advancing the technology. In a Phase II program, appropriate deposition methods for ZG and ZnO should be pursued and small HTS magnets wound and tested, together with continuing thermal modeling studies.

References

1. W. N. Lawless and T. K. Gupta, *J. Appl. Physics* **60**, 607 (1986).